Open Research Online

Strain measurement using neutron diffraction

Thesis

oro.open.ac.uk

Faculty of Technology

Materials Discipline

STRAIN MEASUREMENT USING NEUTRON DIFFRACTION

Duan Qiang (David) Wang

August 1996

A thesis submitted in partial fulfilment of the requirements of the degree of Doctor of Philosophy

Duan Qiang (David) Wang

The Open University

Strain Measurement Using Neutron Diffraction

ABSTRACT

This thesis contains a study of improvement and application of strain measurement technique using neutron diffraction. A dedicated neutron strain scanner – ENGIN, funded by EC, has been developed at ISIS. It has two radial collimators, allowing for the first time, measurements taken simultaneously at two orthogonal directions; uses Pawley refinement permitting both whole pattern and individual peak profile analysis and its positioner allows specimens weighing 250 kg to be placed with an accuracy of 100 μm.

Strain measurement using neutron diffraction has been investigated under two extreme circumstances: very shallow (within 1 mm near surface) and very deep in materials (hundred of mm). Near-surface measurement requires both the accurate determination of the effective measurement position associated with precise location of specimen, calculation of centroid and correction for an anomalous near-surface effect. The strain measurements on a shot-peened surface in titanium alloy were carried out using the methodology mentioned above. The result is comparable to that obtained from X-ray diffraction.

The latter was exploited by studying the effect of wavelength-dependent attenuation in materials. Experiments and theoretical analysis on aluminium and iron show that the effect is small for a strain scanner using radial collimator and time-of-flight technique. However, the reduction of the diffraction peak intensity, as a function of the amount of material in the beam path, reveals that great care should be taken when measuring texture as a function of depth in materials.

The neutron diffraction technique was applied to several sets of engineering strain measurements. Firstly, 3-D residual stresses surrounding a cold expanded hole in a high strength aluminium alloy plate were measured. The result agrees well with that from modified Sachs' method after taking the effect of gauge volume averaging into account. Second, measurements of strain distributions in a Q-joint under zero and 30 kN load have been carried out, which provides a confirmation of the excellence of the joint design as the fastener system has completely shielded the fastener hole from deleterious tensile strains under operational loading. Finally, calibration strain measurement for an energy-dispersive neutron transmission spectrometer was performed for the first time and it is found that the transmission spectrometer is feasible for strain and phase transformation measurement.

PREFACE

The work in this dissertation was taken in the Materials Discipline of the Open University, between June 1993 to August 1996, under the supervision of Dr. Lyndon Edwards. It is the original work of the author except where reference is made to others. None of this work has been submitted, or is in the process of being submitted in whole or part for a degree at any other University. Some of my work has been published and is listed as following:

D.Q.Wang and L.Edwards, "Precise determination of specimen surface position during sub-surface strain scanning by neutron diffraction", Proc. 4th European Conference on Residual Stresses, Cluny, France, June 1996.

D.Q.Wang, L.Edwards, I.B.Harris and P.J.Withers, "Near-surface Strain Measurement by Means of Neutron Diffraction", Proc. 4th European Conference on Residual Stresses, Cluny, France, June 1996.

L.Edwards and D.Q.Wang, "Neutron Diffraction Determination of the Complete 3D Residual Stress Distribution Surrounding a Cold Expanded Hole", Proc. 4th European Conference on Residual Stresses, Cluny, France, June 1996.

L.Edwards and D.Q.Wang, M.W.Johnson, J.S.Wright, H.G.Priesmeyer, F.Rustichelli, G.Albertini, P.J.Withers and I.B.Harris, "Precise Measurement Of Internal Stresses Within Materials Using Pulsed Neutrons, (Premis)", Proc. 4th International Conference on Residual Stresses, publ. Society for Experimental Mechanics, Baltimore USA, pp 220-229, 1994

R.Hermann, D.Q.Wang, M.A.Tomlinson and L.Edwards, "Measurements Of Residual Stresses In Metal-Matrix Composites During Heat-Treatment Using Neutron Diffraction Techniques", Proc. 4th International Conference on Residual Stresses, publ. Society for Experimental Mechanics, Baltimore USA, pp 1144-1153, 1994

A.T.Ozdemir, D.Q.Wang and L. Edwards, "Measurement of the 3D Residual Stress Distribution at Split Sleeve Cold Expanded Holes", Proc. 4th International Conference on Residual Stresses, publ. Society for Experimental Mechanics, Baltimore USA, pp 549-558, 1994

P.J.Withers, I.B.Harris, L.Edwards, D.Q.Wang, M.W.Johnson, J.S.Wright, H.G.Priesmeyer, J.Larsen, J.A.Goldstone, F.Rustichelli and G.Albertini, "ENGIN – A Neutron Spectrometer For Internal Stress Measurement In Lightweight Engineering Structures", Proc. of Inst. Symp. on Adv. Materials for Lightweight Structure, Noordwijk, Holland, March 1994

measurement; Prof. Hans Priesmeyer at GKSS, and Prof. Franco Rustichelli of University of Ancona, Italy.

Finally, and most importantly, I would like to thank my parents and my wife, who always give me encouragement and support.

NOMENCLATURE

σ	general symbol for stress (Pa)
$\sigma_i(z)$	stress variation along the direction z; the subscript indicates the principal stress axis along which the stress is acting
ε	general symbol for strain, with subscripts for principal strain; dimensionless
E	elastic modulus (Pa)
v	Poisson's ratio; dimensionless
a	lattice parameter (Å)
f, g, h	gauge volume dimension in three directions (mm)
L	distance from sample surface to tip of gauge volume in sample (mm)
I	intensity of neutron beam; units of neutron number
k	neutron attenuation coefficient (cm^{-1})
μ	neutron linear absorption coefficient (cm^{-1})
b	neutron diffraction length of atom (barn)
β	neutron diffraction section (cm^{-1})
λ	wavelength of neutrons (Å)

θ Bragg scattering angle (degree)

d interplanar spacing (Å)

d_0 strain-free interplanar spacing (Å)

T time-of-flight of neutrons (μs)

TABLE OF CONTENTS

REFERENCES

CHAPTER 1: INTRODUCTION

There is no standard method for the accurate and non-destructive measurement of 3D stress fields deep within engineering components. Although residual stress measurement by neutron diffraction has been around for over a decade it remains a somewhat esoteric technique due, in no small part, to the need to utilise diffractometers primarily designed for crystallographic structure determination. To address this difficulty, PREMIS (PREcise Measurement of Internal Strain), an EC funded program to design and implement a dedicated strain scanner, named ENGIN, at ISIS, Europe's premiére pulsed neutron source was undertaken. There have been five participants in this project: University of Kiel (Germany), University of Ancona (Italy), University of Cambridge, Rutherford Appleton Laboratory and The Open University. This thesis is based on research work carried out under the PREMIS programme.

1.1 Origins of Residual Stress

Residual stress is present in virtually every solid material or component. Most common manufacturing operations, such as turning, grinding, heat treatment, surface hardening and welding can set up internal stresses. Residual stress can be responsible for reducing component fatigue life, and accelerating stress corrosion.

Residual stress in components can arise from any manufacturing process, which imparts permanent inhomogeneous deformation into a material.

1

It is now generally accepted that residual stresses can be classified into three categories according to the scale over which the residual stresses are almost homogeneous [Macherauch 1986]:

- Residual stresses of type-I (residual stress I) are nearly homogeneous across large areas of several grains, over many millimetres or even centimetres, of a material and are equilibrated within the whole body. Residual stress I is also called macro residual stress.

- Residual stresses of type-II (residual stress II) are nearly homogeneous across microscopic areas, say one grain or partial grain, of a material and are equilibrated over a sufficient number of grains. These stresses occur because of some small-scale anisotropy in the material: for example, due to a mismatch in coefficient of thermal expansion (CTE) or elastic modulus between different phases, or anisotropy in plastic flow between different phases or even individual grains of the material. These stresses were termed "pseudo-macrostresses" by Cullity [1977], as they can be detected using stress-measurement diffraction techniques such as X-ray diffraction, but are undetected by sectioning techniques such as hole drilling. This is because these mismatch stresses must sum to zero over any appreciable volume of the material.

- Residual stresses of type-III (residual stress III) are inhomogeneous across submicroscopic areas of a material, say several atomic distances within a grain, and are equilibrated across small parts of a grain.

Generally, engineers incorporate only type-I stresses into any failure assessment procedure, as they base their calculations on the overall mechanical behaviour of a material and not the microscopic behaviour of its individual grains. However there is growing awareness of the attention that should be given to type-II and III stresses, as they may cause cracking at grain boundaries where discontinuity of stress and strain occurs, especially in multi-phase materials [Krawitz 1991].

2

1.2 Methods of Residual Stress Measurement

All techniques of residual stress measurement rely on the measurement of strains in the component, and a good understanding of the elastic and plastic behaviour of the material enables the strains to be converted to stresses. The ultimate objective of measuring residual strain in a component is to obtain the full 3D stress tensor at any point in the interior, preferably without destroying the component. Residual strain measuring techniques are either 'destructive' or 'non-destructive' depending on whether the component is potentially reusable after the measurement. Most mechanical residual stress analyses are based on the release of macrostrains by cutting, shaving, or chemical milling and measuring the shape change during the process. Among non-destructive methods, X-ray diffraction and neutron diffraction (ND) both rely on the determination of lattice strain. This involves the measurement of small changes in lattice spacing by applying Bragg's law of diffraction [Allen 1985]. The main advantage of using neutrons rather than X-rays as a probe is that neutrons can penetrate deeply into the material (several cm) whereas X-rays can only be used as a surface measurement of residual stress.

1.2.1 Destructive Measurement Techniques

In destructive test methods material is removed from a sample, resulting in stress relaxation in the remaining material. The change in strain at different points on the surface of the component can then be related to the residual stress that existed in the removed layer. The variation in strain is usually measured by strain gauges. Methods of material removal may also introduce residual stresses, modifying the original residual stress field. It is essential that this effect is minimised

1.2.1.1 Hole drilling

This is a widely used procedure. In the standard method, the stress at the surface is obtained following relaxation by drilling a hole to a depth of 1.5 times the hole diameter. The relaxation on the surface is measured using a special strain gauge rosette centred around the hole as shown in figure 1.1. If σ_{1h} and σ_{2h} are the principal stresses on the surface of the material; and α, the reference position for a single strain gauge measurement, then the radial strain at the surface of the specimen ε_{in} (α_i) resulting from material removal over Δh_i is given by [Niku-Lari 1985]:

$$\varepsilon_{in}(\alpha_i) = A_{in}\Delta h_i(\sigma_{1hi}+\sigma_{2hi})+B_{in}\Delta h_i(\sigma_{1hi} - \sigma_{2hi})\cos 2\alpha_i \qquad (1.1)$$

A_{in} and B_{in}, the correlation coefficients, can be obtained by theoretical or finite element calculations. For a strain gauge rosette three such equations are obtained for α_i, $\alpha_i + \gamma$ and $\alpha_i + \varphi$. In an extension of the drilling well defined incremental steps enables residual stress depth profiles to be obtained [Niku-Lari 1985], [Schajer 1988]. The depth increment is limited by the accuracy of the cutting tool but can be as small as 0.02 mm, permitting the measurement of stress gradients up to 1500 MPa/mm [Niku-Lari 1985]. Major assumptions when using the hole-drilling technique are:

- the material is elastic and isotropic

- measured stresses are below the elastic limit

- stress components normal to the surface are negligible

- the stresses within the layer of material to be removed is uniform

- the shear force is negligible between successive layers.

There are limitations to the depth that can be explored (approximately 8 mm [Hauk 1986]) and the steepness of stress gradients possible, as the strain is averaged over the depth of the drilled layer. The typical time for a single surface stress measurement is only a few minutes. A similar technique to hole-drilling is the ring core method (trepanning) where

an annular groove is cut around a strain gauge rosette and the relaxed strains are measured [Proctor 1987], [Almen 1963]. Steep stress gradients can be resolved using this technique [Macherauch 1986].
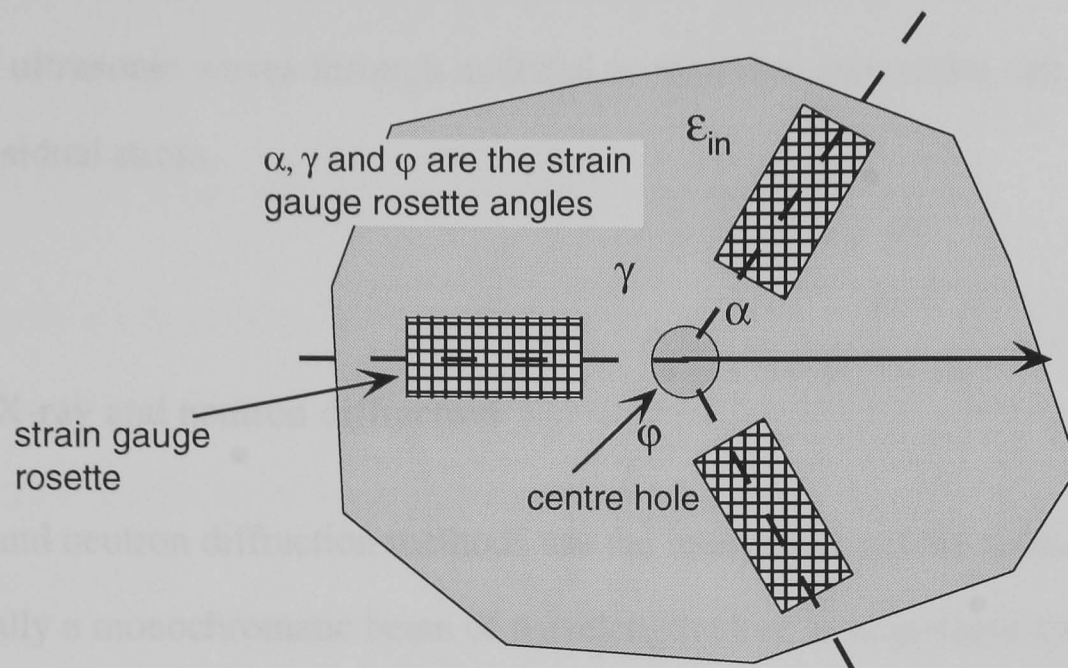
Figure 1.1 Arrangement of strain gauge in hole drilling method.

1.2.1.2 Sachs boring

The Sachs boring method [Sachs 1927] also relies on the relaxation of stresses after concentric layers of material are removed. The change of strain is used to obtain the residual stress in the removed layers. Assumptions in the analysis are:

- the material is isotropic

- the residual stresses are distributed with rotational symmetry about the axis of the cylinder

- the bore is concentric with the outer diameter

- the ring is thick enough to prevent lateral bending

- the axial stress is negligible

In most cases the hoop stresses are the most significant in failure analysis of cylinders, being much larger than the radial or axial stresses [Stacey 1985].

5

1.2.2 Non-Destructive Stress Measurement

Non-destructive methods of residual stress measurement rely on some intrinsic properties of the material to enable the measurement of stress. Variations in interatomic spacing, velocities of ultrasonic waves through material or magnetic properties can all be used to determine residual stress.

1.2.2.1 X-ray and neutron diffraction

Both X-ray and neutron diffraction methods use the interplanar atomic spacing as a strain gauge. Usually a monochromatic beam of wavelength close in magnitude to the atomic spacing is directed to the material under examination. Bragg reflection of the X-ray or neutron beam gives the interplanar atomic spacing of suitably oriented planes, and shifts in the Bragg peak give the strain for particular (hkl) plane. The engineering stress is obtained from the crystallographic elastic constants which relate the elastic strain in a crystal to the bulk engineering stress. Strain measurements are restricted to surface regions in the case of X-rays due to their low penetration depth, whereas with neutron diffraction, measurements are possible to depth of a few centimetres. Diffraction methods are generally non-destructive, but if depth profiles are required using X-ray measurement surface layers must be removed rendering the process destructive. A more detailed description of neutron and X-ray diffraction methods is given in chapter 2.

1.2.2.2 Ultrasonic methods

Acoustic methods of stress measurement use the propagation of Rayleigh waves through the surface of a material. If ultrasonic waves are passed through a material the velocity of the wave is affected by the variation of strain in the material (acoustoelastic effect) and this effect is used for residual strain measurement. By using different wave modes the only measured quantity needed is the ultrasonic time-of-flight (velocity) of the sound

waves from generator to receiver. If two or three modes of vibration are generated, they are each influenced differently by the state of strain. By varying the frequency the depth of strain measurement can be varied [Thompson 1994]. Only elastic strains are measured, and the technique cannot be used to measure strains normal to the plane of the plate. The separation of texture and acoustoelastic effects is a problem, although Delsanto [Delsanto 1986] has proposed solutions for this.

Measuring times are approximately one minute, with depths of measurement possible to 10 mm [Herzer 1990]. Complications with the technique arise from texture, or changes in microstructure, grain size, dislocation density or temperature as all can introduce large errors into the analysis.

1.2.2.3 Magnetic methods

Measurements using this technique are restricted to ferromagnetic materials or ferromagnetic phases in heterogeneous materials. Micromagnetic quantities such as the magnetic and acoustic Barkhausen noise, incremental permeability and the dynamic magnetostriction can be used [Theiner 1986]. The advantage of these methods lies in the fact that quantities can be used that are sensitive to either stress, microstructure and/or texture. Unambiguous residual stress results can be obtained by combining independent micromagnetic quantities. Variations of strain, dislocation density and microstructure affect the magnetization curve. Barkhausen noise is a term used to describe the domain wall movements which separate different magnetic domains. These magnetic domains are modified when an external magnetic field is applied. The movement of the domain walls is picked up by a suitable coil device, converting the movement to voltage pulses, and is observed on a (B - H) magnetization curve [Ruud 1982]. Barkhausen noise is sensitive to the material condition and the residual stress state. A micromagnetic multiparameter microstructure and residual stress analysis testing procedure is used for measuring the magnetic Barkhausen noise and the incremental permeability. Calibration measurements

are necessary on 'unstressed material' for an accurate interpretation of the results and absolute stress values.

CHAPTER 2: PRINCIPLES OF STRESS MEASUREMENT USING DIFFRACTION TECHNIQUE

2.1 Introduction

Stress measurements by diffraction rely on Bragg's law and a knowledge of the full 3D elastic response of a crystal. Ideally, the relationship between single crystal deformation and that of polycrystals should also be known because both neutron and X-ray diffraction techniques measure strains by determining lattice d-spacings in materials, and using these strains to calculate the internal stresses.

2.2 Elasticity Theory in Solids

2.2.1 Stress and Strain – Hooke's Law

Strain and stress in solids are second rank tensors. For the case of isotropic solids the strain tensor can be given in terms of stresses according to Hooke's law as:

$$\varepsilon_{ij} = \frac{1+\nu}{E}\sigma_{ij} - \delta_{ij}\frac{\nu}{E}\sigma_{kk} \qquad (2.1)$$

where k is a dummy suffix summing over all k (i.e. $\sigma_{kk} = \sigma_{11} + \sigma_{22} + \sigma_{33}$); E, the Youngs modulus; ν, the Poissons ratio; and δ, Kronecker's delta function. The stress tensor can be obtained by inverting equation (2.1):

$$\sigma_{ij} = \frac{E}{1+\nu}\varepsilon_{ij} + \frac{\nu E}{(1+\nu)(1-2\nu)}\delta_{ij}\varepsilon_{kk} \qquad (2.2)$$

When an anisotropic system is considered the expressions are not that simple and a generalised Hooke's law can be written as:

$$\sigma_{ij} = C_{ijkl}\varepsilon_{kl} , \qquad\qquad \varepsilon_{ij} = S_{ijkl}\sigma_{kl} \qquad\qquad (2.3)$$

where C_{ijkl} are the elastic stiffness constants relating the stresses in direction ij to the strains in direction kl while S_{ijkl} are the elastic compliance constants relating the strains in directions ij to the stresses in directions kl. C_{ijkl} and S_{ijkl} are both fourth rank tensors.

2.2.2 Single Crystal Elastic Constants (SCEC's)

Polycrystalline materials exhibit isotropic behaviour unless the materials have had some directionality introduced by manufacturing processes such as rolling and cold drawing which generate anisotropy in the final materials' microstructures. An isotropic assumption is often reasonable as the bulk mechanical properties of the materials result from the characteristics of randomly oriented crystals. However, elastic properties in single crystals vary with direction as crystal lattices are themselves anisotropic. As a result, engineering strains in polycrystals are often deduced from the anisotropic response of a single crystal, considering grain interactions, and transfer of stress and strain at grain boundaries. In crystallography, the crystal planes and directions are indexed in terms of the Miller indices, (hkl).

Crystals have long range order in the position and stacking sequence of their constituent atoms. A unit cell is defined to describe the repeat properties. The lattice parameter characterises the size of the unit cell or the arrangement of the lattice equivalent points. There are seven unique crystal unit cells and fourteen Bravais lattices describing the atomic layout. Only cubic and hexagonal systems will be discussed in detail as these are the most commonly occurring in metals. For a detailed description of other systems see Cullity [1978].

The interatomic d-spacing for a given crystal plane in a unit cell can be obtained using:

$$d_{hkl} = \frac{1}{\sqrt{\dfrac{h^2 + k^2 + l^2}{a^2}}} \qquad (2.4)$$

for a cubic crystal and:

$$d_{hkl} = \frac{1}{\sqrt{\dfrac{4}{3}\left(\dfrac{h^2 + k^2 + hk}{a^2}\right) + \dfrac{l^2}{c^2}}} \qquad (2.5)$$

for a hexagonal crystal. The lattice parameter, a, for a cubic crystal represents the length of a side of the unit cell whilst a and c are the lattice parameters for a hexagonal crystal and represent the base dimension and the height of the unit cell respectively.

The symmetry in cubic systems allows the elastic compliance constant to be reduced to:

$$S_{ij} = \begin{bmatrix} S_{11} & S_{12} & S_{12} & 0 & 0 & 0 \\ S_{12} & S_{11} & S_{12} & 0 & 0 & 0 \\ S_{12} & S_{12} & S_{11} & 0 & 0 & 0 \\ 0 & 0 & 0 & S_{44} & 0 & 0 \\ 0 & 0 & 0 & 0 & S_{44} & 0 \\ 0 & 0 & 0 & 0 & 0 & S_{44} \end{bmatrix} \qquad (2.6)$$

C_{ij} can be obtained by replacing S with C in the expression (2.6). The Young's modulus can be derived from the strains in the cubic crystal subject to an uniaxial stress as following [Allen 1985]:

$$\frac{1}{E_{hkl}^{//}} = \frac{\varepsilon_{hkl}^{//}}{\sigma_{applied}} = S_{11} - 2SA_{hkl} \qquad (2.7)$$

where $\varepsilon_{hkl}^{//}$ is the strain in the direction of the applied load, and

$$A_{hkl} = \frac{h^2k^2 + k^2l^2 + l^2h^2}{(h^2 + k^2 + l^2)^2} \qquad (2.8)$$

is the anisotropy factor which describes the degree of elastic anisotropy in a crystal, and S is given by:

$$S = S_{11} - S_{12} - \frac{S_{44}}{2} \qquad (2.9)$$

Considering the strain response in a direction perpendicular to the applied stress direction allows the Poisson ratio (ν) to be obtained, thus:

$$\frac{1}{E_{hkl}^{\perp}} = \frac{\varepsilon_{hkl}^{\perp}}{\sigma_{applied}} = S_{12} + 2A_{hkl} \qquad (2.10)$$

Poissons ratio ν as measured by a given (hkl) reflection is therefore:

$$\nu = -\frac{\varepsilon_{hkl}^{\perp}}{\varepsilon_{hkl}^{/\!/}} = -\frac{E_{hkl}^{/\!/}}{E_{hkl}^{\perp}} \qquad (2.11)$$

In a hexagonal crystal the elastic compliance constant becomes:

$$S_{ij} = \begin{bmatrix} S_{11} & S_{12} & S_{13} & 0 & 0 & 0 \\ S_{21} & S_{22} & S_{23} & 0 & 0 & 0 \\ S_{31} & S_{32} & S_{33} & 0 & 0 & 0 \\ 0 & 0 & 0 & S_{44} & 0 & 0 \\ 0 & 0 & 0 & 0 & S_{44} & 0 \\ 0 & 0 & 0 & 0 & 0 & 2(S_{11} - S_{12}) \end{bmatrix} \qquad (2.12)$$

A similar analysis to that used for cubic crystals given above can be followed, giving the Youngs modulus in any direction as:

$$\frac{1}{E} = S_{11}\left(1 - a_{13}^2\right)^2 + S_{33}\, a_{13}^4 + a_{13}^2\, (S_{44} + 2S_{13})\left(1 - a_{13}^2\right) \qquad (2.13)$$

From this expression it is observed that the Young's modulus in a given direction depends only on the direction cosine a_{13}, which is the cosine of the angle between the direction of interest (plane normal) and the axis of hexagonal symmetry (c-axis).

2.2.3 Elastic Constants in Polycrystalline Materials

For polycrystals the elastic response of a given direction can be calculated from the Single Crystal Elastic Constants provided that some form of macroscopic averaging is used to model the random orientation of crystallites. The strain fields within individual crystallites will vary depending on their orientation. Various theories have been proposed for simplifying the calculation of strain and stress fields in polycrystals. The method of Voigt [1928] assumes that each crystallite experiences the same strain (i.e., there is transfer of strain at grain boundaries), resulting in a variation of stress from crystallite to crystallite. In the method of Reuss [1924] each crystallite is assumed to experience the same stress (i.e. there is transfer of stress at grain boundaries) resulting in a variation of strain from crystallite to crystallite. These two theories (Voigt and Reuss) are extremes to the true state of stress and strain and in reality a combination of these states must exist for continuity at grain boundaries. Eshelby [1957] considered the case of an anisotropic ellipsoidal inclusion in a homogenous isotropic matrix. Kroner [1958] extended the method of Eshelby and obtained the strain and stress distribution in the inclusion. The strain and stress distributions hence can be estimated using either the Voigt, Reuss or Kroner theory from the SCECs. Neerfeld [1942] and Hill [1952] also suggested using the average of the Reuss and Voigt estimates to obtain the average elastic constants.

2.2.3.1 Voigt's solution

The Voigt method assumes that the strain field throughout the polycrystal is uniform, implying that all grains experience the same strain and that there is a continuity of strain at the grain boundaries (figure 2.1). The stress will hence vary from point to point within material. Noyan [1987] presented the analysis for averaging the elastic stiffness in a cubic crystal and showed that the Youngs modulus and Poissons ratio are:

$$E = \frac{3\ (C_{11} + 2C_{12})\ (\ C_{11} - C_{12} + 3C_{44})}{5\ (C_{11} + 2C_{12}) + (C_{11} - C_{12} + 3C_{44})} \qquad (2.14)$$

13

$$v = \frac{-5 \ (C_{11} + 2C_{12}) - 2 \ (\ C_{11} - C_{12} + 3C_{44})}{10 \ (C_{11} + 2C_{12}) + 4 \ (C_{11} - C_{12} + 3C_{44})} \qquad (2.15)$$

In HCP crystals the Voigt averages are [Prummer 1988]:

$$S_1 = \frac{3 \ (4C_{44} - C_{11} - C_{33} - 5C_{12} - 8C_{13})}{(2C_{11} + C_{33} + 2C_{12} + 4C_{13}) \ (7C_{11} + 2C_{33} - 5C_{12} - 4C_{13} + 12C_{44})} \qquad (2.16)$$

and

$$\frac{1}{2} S_2 = \frac{15}{7C_{11} + 2C_{33} - 5C_{12} - 4C_{13} + 12C_{44}} \qquad (2.17)$$

S_1 and $(1/2)S_2$ are the Voigt estimates of the X-ray elastic constants. The Young's modulus and Poisson ratio are then:

$$\frac{1}{E} = S_1 + \frac{1}{2} S_2 \qquad \text{and} \qquad v = -ES_1 \qquad (2.18)$$
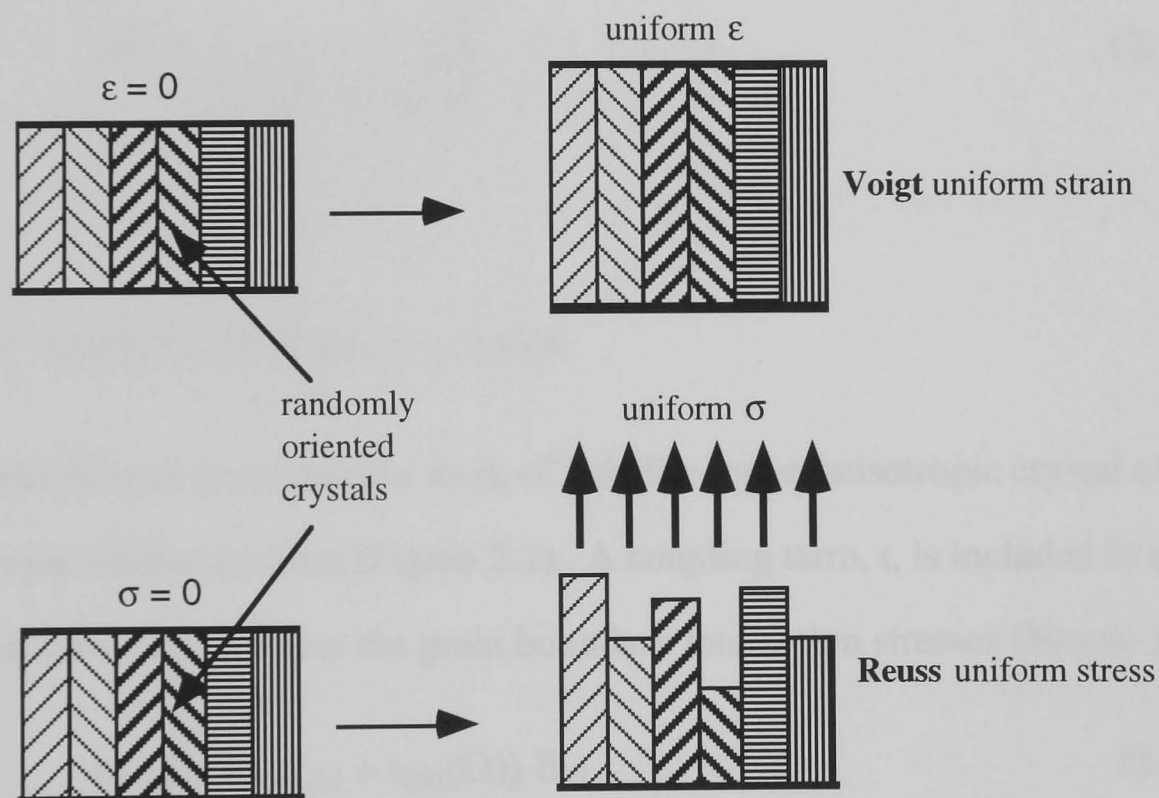
Figure 2.1 Voigt and Reuss models for the relationship between strain and stress

2.2.3.2 Reuss' solution

In Reuss' method it is assumed that there is continuity of stress at the grain boundaries. The strain therefore varies from point to point and for a cubic system (see figure 2.1):

$$E_{hkl} = \frac{1}{S_{11} - 2SA_{hkl}} \qquad (2.19)$$

14

$$v_{hkl} = \frac{-(S_{12} + SA_{hkl})}{S_{11} - 2SA_{hkl}} \qquad (2.20)$$

For hexagonal crystal the Reuss assumption gives [Prummer 1988]:

$$S_1 = \frac{1}{2}(S_{12} + S_{12}) + \frac{1}{2}(S_{11} + S_{33} - S_{13} - S_{12} - S_{44}) - a_{13}^2 - \frac{1}{2}(S_{11} + S_{33} - S_{44} - 2S_{13}) - a_{13}^4 \qquad (2.21)$$

and

$$\frac{1}{2}S_2 = \frac{1}{2}(2S_{11} - S_{12} - S_{13}) - \frac{1}{2}(5S_{11} + S_{33} - 5S_{13} - S_{12} - 3S_{44})\, a_{13}^2 +$$

$$\frac{3}{2}(S_{11} + S_{33} - S_{44} - 2S_{13})\, a_{13}^4 \qquad (2.22)$$

where a_{13} is the cosine of the angle between the normal to diffracting plane and the c-axis, which is given by:

$$a_{13}^2 = \frac{l^2}{\frac{4}{3}\left(\frac{c}{a}\right)^2 (h^2 + k^2 + hk) + l^2} \qquad (2.23)$$

2.2.3.3 Eshelby and Kroner's solution

In this model Kroner extended the work of Eshelby for an anisotropic crystal embedded in an isotropic elastic medium (Figure 2.2). A coupling term, t, is included in equation (2.3) which takes into account the grain boundary interaction stresses [Noyan 1987]:

$$\varepsilon_{ij}(\Omega) = (S_{ijkl} + t_{ijkl}(\Omega))\, \bar{\sigma}_{kl} \qquad (2.24)$$
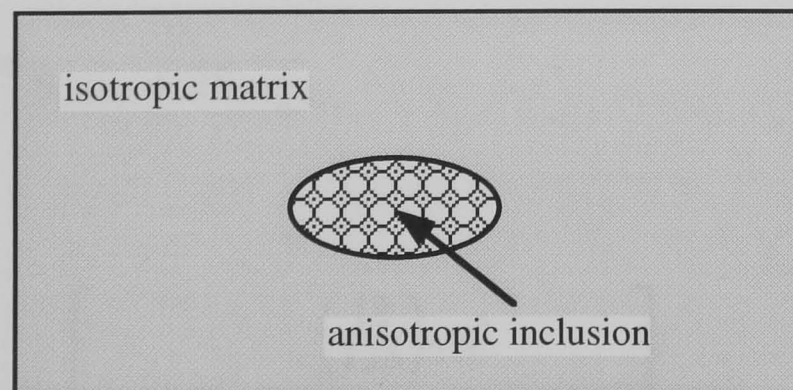
Figure 2.2 Eshelby-Kroner analysis modelled on the deformation of an anistropic inclusion in an isotropic matrix .

$$\bar{\varepsilon}_{ij} = (S_{ijkl})_B\, \bar{\sigma}_{kl} \qquad (2.25)$$

15

where $(S_{ijkl})_B$ is the average bulk value of the single crystal elastic constants S_{ijkl} and Ω represents the volume of the diffracting crystallites. The elastic constants for cubic crystal are given by:

$$-\frac{\nu}{E} = (S_{3311})_B + t_{3311} + t_0 A_{hkl} \tag{2.26}$$

$$\frac{1 + \nu}{E} = (S_{3333})_B - (S_{3311})_B + t_{3333} - t_{3311} - 3t_0 A_{hkl} \tag{2.27}$$

where $t_0 = t_{3333} - t_{3311} - 2t_{3131}$ and the coupling factor is given by:

$$t_{3333} = \frac{1}{3G_k} \frac{2G_k(S_{1111}(\Omega) - S_{1122}(\Omega)) - 1}{\frac{8G_k^2 + 9K_kG_k}{6G_k + 3K_k}\left(S_{1111}(\Omega) - S_{1122}(\Omega)\right) + 1} \tag{2.28}$$

and

$$t_{3311} = t_{3131} = -0.5t_{3333} \tag{2.29}$$

The bulk elastic constants $(S_{3333})_B$ and $(S_{3311})_B$ represent averages over the single crystal elastic constants S_{ijkl} and are given by:

$$(S_{3311})_B = \frac{1}{3}\left[\frac{1}{3K_k} - \frac{1}{2G_k}\right] \tag{2.30}$$

$$(S_{3333})_B - (S_{3311})_B = \frac{1}{2G_k} \tag{2.31}$$

The subscript k represents the Kroner estimate. K_k and G_k are the average bulk and average shear moduli in the Kroner limit and are given by:

$$3K_k = \frac{1}{S_{1111} + 2S_{1122}} \tag{2.32}$$

and

$$G_k = G_v\left[1 - \frac{\left(\frac{12}{125}\right)wx^2}{1 - \left(\frac{2}{25}\right)wx - \left(\frac{24}{625}\right)w^2x^2}\right] \tag{2.33}$$

G_v is the Voigt average of the shear modulus and is given by:

$$G_v = \left(\frac{1}{5}\right)[(C_{11} - C_{12} + 3C_{44}]$$ (2.34)

w and x are given by:

$$w = \frac{6G_v + 3K_k}{4G_v + 3K_k}$$ (2.35)

$$x = \frac{5A_{hkl}}{3S_{1111} - 3S_{1122} + 4S_{1212}}$$ (2.36)

So, with only knowledge of the single crystal elastic constants the Kroner estimates of the elastic constants can be obtained using equations (2.26) and (2.27) for cubic crystals.

The Kroner model gives elastic constants closer to the measured values than the Voigt or Reuss estimates. However, the Neerfeld – Hill average [Neerfeld 1942] gives results close to the Kroner model and provides an easier-to-use alternative.

2.3 Determination of Stress from Neutron Diffraction Data

2.3.1 Neutron Characteristics

The technique of neutron scattering can be used to study both structure and dynamics of matter since the thermal neutron (between $10 - 100\,meV$) wavelength is of the same order of magnitude as typical atomic spacings, and they have comparable energies to those of atomic excitations in solids. The earliest references [Allen, Schmank, Krawitz, Pintschovius 1981] to stress measurement by neutron diffraction date from the early 1980s and the field is currently developing at most neutron sources due to improvements to the source and instruments, while X-rays have been used for the stress measurement for much longer.

The properties of the neutron that makes it suitable to condensed matter science can be summaried as follows:

- Neutrons are a unique probe, allowing the simultaneous measurement of microscopic structure and dynamics;

- Neutrons with velocity v have an intrinsic de Broglie wavelength:

$$\lambda = \frac{h}{mv} \qquad (2.37)$$

where h is Planck's constant; m, the neutron mass. Thus neutrons behave like waves. Neutrons have wavelengths similar to atomic spacings permitting diffraction measurements to be performed. Diffraction experiments range in length scale from directly probing the wavefunction of the hydrogen atom to the low-resolution study of macromolecules;

- Neutrons scatter from materials via interaction with the nucleus rather than the electron clouds. This means that the scattering power of an atom is not strongly related to its atomic number, unlike X-ray and electron scattering. This has three advantages: (i) it is easier to sense light atoms, such as hydrogen, in the presence of heavier ones, (ii) neighbouring elements in the periodic table generally have substantially different scattering cross sections and can be distinguished, and (iii) the nuclear dependence of scattering allows isotopes of the same elements to have substantially different neutron scattering lengths.

- Neutrons have a magnetic moment which couples directly to spatial variations of the magnetisation of materials on an atomic scale. Unlike other forms of radiation, neutrons are thus ideally suited to the study of magnetic structures (and hence microscopic magnetism) and short wavelength magnetic fluctuations. The cross-sections for magnetic and chemical structure are fortunately of the same magnitude, permitting the simultaneous measurements of magnetic and chemical behaviour of materials;

- Neutrons perturb the system weakly thus greatly facilitating theoretical interpretation of neutron scattering measurements and allowing absolute cross-sections to be

determined. This often means that neutron scattering provides the most reliable scientific results in a diverse range of areas;

- Neutrons are a highly penetrating probe (Appendix 1), allowing the investigation, again non-destructive, of the interior of materials, rather than the surface layers probed by techniques such as X-rays, electron microscopy or optical methods. This feature can also make the use of complex sample environments such as cryostats, furnaces and pressure cells quite routine, and enables the measurement of bulk processes under realistic conditions.

Neutrons can be generated by fission and spallation, which are employed in reactor and spallation sources respectively. In reactor sources the initial energy of neutrons in a nuclear reaction is measured in MeV and they have wavelengths too small to be of use for diffraction. A moderator is employed to slow down the neutrons from fission and is made of hydrogenous materials (light or heavy water, or CH_4), which should have a reasonable scattering cross section without a large absorption [Carpenter 1986].

In pulsed sources neutrons are produced by spallation, which occurs when energetic particles like protons interact with target nuclei. Heavy element targets offer the best efficiency for emitted neutrons per unit energy of the incident pulse, and either a tantalum or a depleted uranium target is used. The protons are typically accelerated in bursts to 800MeV using a synchrotron and are subsequently directed at the target. The target nuclei are excited and "boil off" neutrons and lighter particles in an 'evaporation' process. Each incident burst produces a pulse of highly energetic (up to 1MeV) neutrons. The fast neutrons from the initial pulse are then 'thermalised' using a moderator [Windsor 1981].

Neutrons which undergo many collisions with the moderator material achieve thermal equilibrium with their surroundings. By opening an aperture to the moderator, a Maxwellian distribution of neutron energies is obtained in which the maximum intensity is determined by the moderator temperature, T, as described in the following equation [Hughes 1953]:

$$\frac{h^2}{2m\lambda^2} = K_B T \qquad\qquad (2.38)$$

where K_B is Boltzmann's constant. The neutrons from the moderator are then guided to experimental instruments via a tube which consists of nickel-plated glass plates.

The inherent difference between pulsed and continuous sources concerns the ways in which the scattered radiation is measured. If a neutron is created at a known time and position, its energy (and therefore wavelength) on detection can be determined from the distance it has travelled to the detector and the time taken to do so, called the Time-Of-Flight (TOF). Measurements on pulsed sources are energy dispersive, and for powder diffraction are independent of the scattering angle (although the resolution of individual detectors is dependent on the scattering geometry) [Windsor 1981].

2.3.2 Fundamental Concepts of Diffraction Methods

For strains to be measured, coherent scattering of the radiation is essential, i.e. scattering resulting in distinctive Bragg peaks. Using a monochromatic X-ray or neutron beam with wavelength λ, the Bragg equation enables the angular position θ_{hkl}, of the diffraction peak of a family of crystallographic planes to be determined (see Figure 2.3). Knowing λ and θ_{hkl} the interplanar spacing d_{hkl} for the (hkl) set of planes can be obtained:

$$2d_{hkl} \sin\theta_{hkl} = n\lambda \qquad\qquad (2.39)$$

where n is an integral (n =1 for the first order reflection) and $2\theta_{hkl}$ is the angle between the incident beam and the diffracted beam. For an elastic strain to exist there must be some deformation of the lattice and, depending on the nature of the loading, the spacing between any set of crystallographic planes will change. Referring to the Bragg equation, this elastic strain will therefore be detected, by a shift in the value of $2\theta_{hkl}$ for a constant wavelength, for a particular reflecting plane. Differentiation of equation (2.39) gives:

$$\Delta\theta_{hkl} = -\tan\theta_0 \left(\frac{\Delta d}{d_0}\right) \qquad\qquad (2.40)$$

where Δd is the change of lattice parameter, and d_0, the stress-free lattice parameter. So, the strain in the (hkl) set of planes is given as:

$$\varepsilon = \left(\frac{\Delta d}{d_0}\right) = -\Delta\theta \cot\theta_0 \qquad (2.41)$$
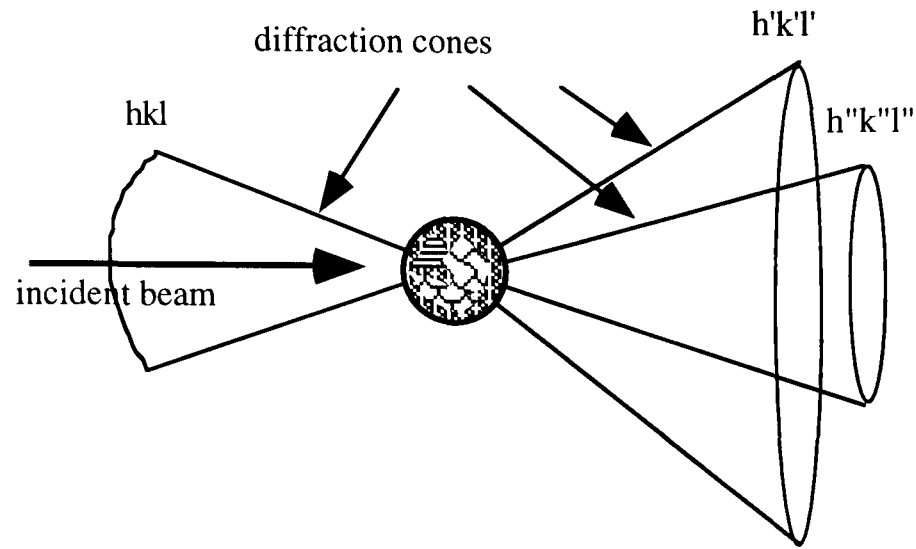
Figure 2.3 Monochromatic neutron diffraction of polycrystals

In the Time-of-Flight technique the lattice spacing, d_{hkl} is determined by maintaining a constant scattering angle, 2θ at the detector and scanning the wavelength. Therefore from equation (2.37), (2.39) and the following equation,

$$v = \frac{L}{T} \qquad (2.42)$$

where L is the distance of neutron flight; T, the Time-of-Flight, so

$$T_{hkl} = \frac{2mLd_{hkl}\sin\theta}{h} \qquad (2.43)$$

and since the Time-of-Flight is proportional to neutron velocity, by equation (2.37) then:

$$\varepsilon = \frac{\Delta d_{hkl}}{d_{hkl}} = \frac{\Delta\lambda_{hkl}}{\lambda_{hkl}} = \frac{\Delta T_{hkl}}{T_{hkl}} \qquad (2.44)$$

21

2.3.3 Determination of Stresses

For the Time-of-Flight technique which uses a pulsed 'white' beam of neutrons, the energy, and hence wavelength, of each neutron that arrives at the detector can be deduced from its time of flight from the target source. Since the high energy (low wavelength) neutrons arrive at the sample first, Bragg diffraction is first observed for the lower d spacings, the larger spacings arrive later. Thus each pulse provides a diffraction profile across a very large range of d spacings (≈ 0.4 - 3 Å), but at a low intensity. Many profiles over successive peaks are then summed to give a statistically significant diffraction profile. This process is, in effect, energy dispersive neutron spectrometry. The lattice strain in a given gauge volume (figure 2.4) is then given simply in terms of the time shift of the relevant peak (Δt) as shown in equation (2.43).
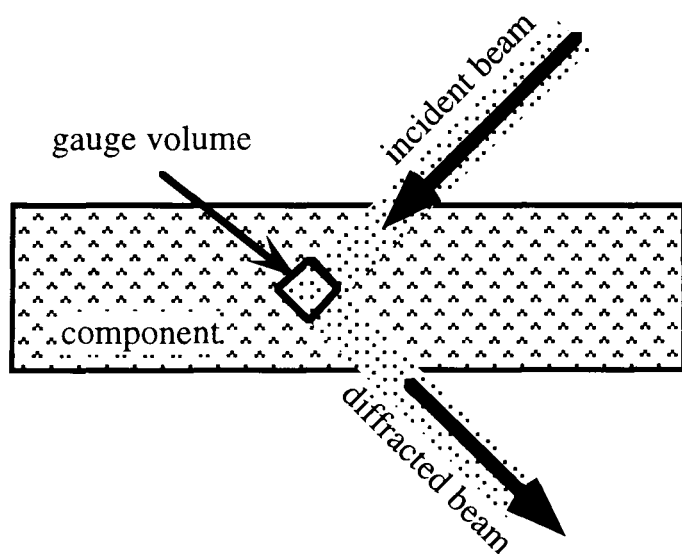
Figure 2.4 Definition of gauge volume
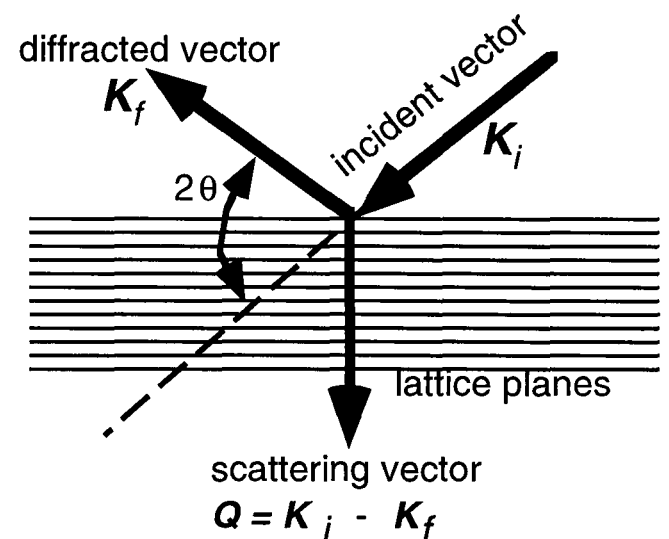
Figure 2.5 Definition of scattering vector

To fully specify the strain tensor at least six strain measurements are required unless some symmetry is assumed [Allen 1985]. This is achieved by reorienting the specimen with respect to Q, the scattering vector which is the measured strain direction as shown in figure 2.5. The strain tensor defined relative to orthogonal axes (x, y, z) in a sample can be determined from measurements in different directions. If the orientation of Q relative to the sample axes is given by the direction cosine (l', m', n') then:

$$\varepsilon \, (l', m', n') = l'^2 \, \varepsilon_{xx} + m'^2 \, \varepsilon_{yy} + n'^2 \, \varepsilon_{zz} +$$

22

$$2l'm'\varepsilon_{xy} + 2m'n'\varepsilon_{yz} + 2l'n'\varepsilon_{zx} \qquad (2.45)$$

Once the strain tensor is determined the principal axes can be found by diagonalization. The principal stresses can then be calculated using equation (2.2), the macroscopic Young's modulus, E, and Poisson's ratio, ν for isotropic materials are discussed in section 2.2.

2.4 Techniques of Neutron Strain Measurement

Neutron diffraction has been used extensively in determining internal strains both in metals and composites [Hutchings 1992 and Kupperman 1994]. The instruments used are divided into three catalogues: the conventional diffractometer, the Fourier correlation spectrometer and the Energy-dispersive Neutron Transmission Spectrometer (EDNTS).

The conventional diffractometer is based on the Bragg diffraction equation as mentioned in previous sections. It is by far the most important technique in the field of strain measurement by means of neutron diffraction, and the method is available at almost every neutron source.

The Fourier correlation spectrometer [Priesmeyer 1990] operates in the reverse time-of-flight (RTOF) mode which is a method invented by Prof. P. Hiismaki, VTT Finland [Hiismaki 1985]. The neutron intensity of a steady-state reactor source can be used most efficiently by means of reverse time-of-flight. An inherent advantage of the method is the independence of intensity from instrumental resolution.

The Energy-dispersive Neutron Transmission Spectrometer (EDNTS) utilises the high resolution and statistical accuracy advantages of transmission diffraction [Jonson and Bowman 1981] and is under development. The method is equivalent to measurements in the scattering geometry of powder diffraction with $2\theta = 180°$. The system has been set up at LANSCE and some pilot experiments have been carried out: investigating the time-temperature-transformation behaviour of grey cast iron at $350°C$ and the structural

changes in a piezoelectric lead-zirconate-titanate (PZT-5A) sample. It is a promising tool to investigate real-time solid state phase transformation, hydrostatic, type-II and 2-dimensional strains in materials.

The principal problems with the development of stress measurement by neutron diffraction as a standard industrial technique are:

- obtaining stress-free lattice-spacing data (the "d_0 problem")

- handling the complications associated with texture

d_0 can be solved using either the macrostress equilibrium condition in the component [Noyan 1987]; or by considering the slope of the strain anisotropy if there is no hydrostatic stress in the region [Bourke 1991], or by measuring a small stress-free cube [Krawitz 1994] or powder of the same material as the specimen. One more solution for d_0 is called d vs $\sin^2\psi$ technique [Hauk 1982, Noyan 1985], in which a biaxial stress field must be assumed in the materials.

Texture can cause complications with the conversion of strain to stress, because the elastic constants are altered by texture. However, texture can be analysed from variations in relative amplitude of the diffraction peaks with scattering direction. While strains can be measured with either a spallation or steady-state source, spallation sources have the advantage of providing a broad energy spectrum; thus the average strain can be measured by examining many diffracting planes, a situation not practical with the monochromatic beam generally used for strain measurement at reactor sources. The stress field has to be calculated by a numerical computing method using the orientation distribution function (ODF) [Behnken 1991], if there is strong texture in the material.

2.5 Examples of Strain and Stress Measurement Using Neutron Diffraction

2.5.1 Neutron Elastic Constants and Anisotropic Effects

The measurement of the lattice strain of the (211) reflection of ordinary mild steel using a stress rig is shown in figure 2.6 [Hutchings 1992], where it is compared with the overall macroscopic strain of the sample measured simultaneously with an extensometer. The effective neutron Young's Modulus E is close to the macroscopic value, and the response is linear even in the plastic region indicating that it is the elastic component which is measured by the lattice for this reflection. On release of the applied stress there is no residual elastic lattice strain, whereas the extensometer shows a residual plastic strain of about 4%.
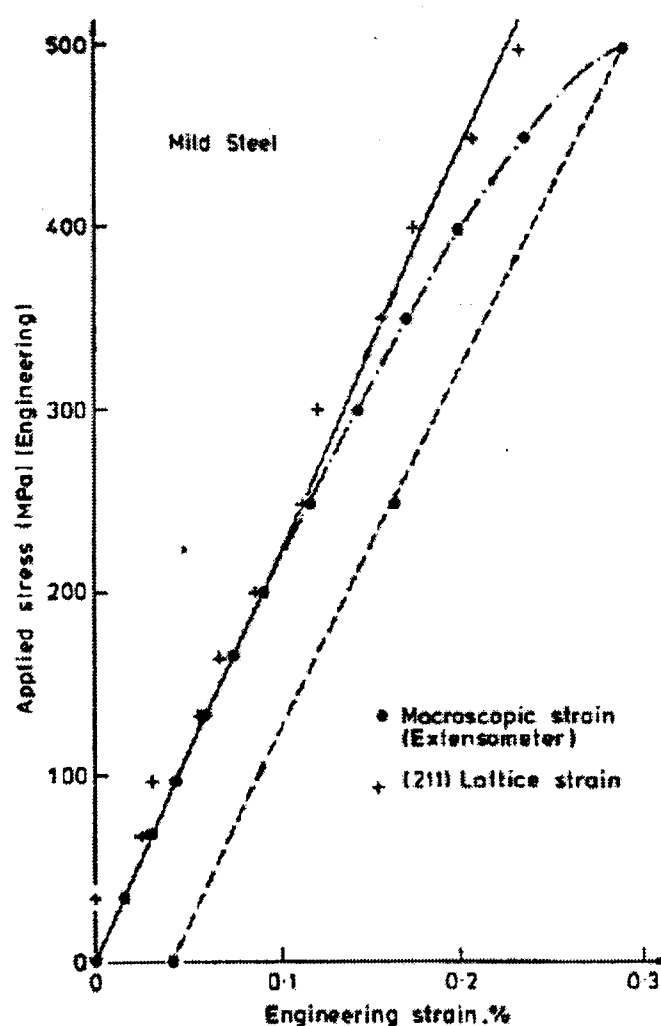
Fig. 2.6 The (211) lattice macrostrain response parallel to applied stress levels. Extensiometer measurement of the overall specimen strain is also shown.

The value of the anisotropy factor for the (211) reflection is 0.25, equal to that of the (110) and (321) reflections which are therefore expected to show similar response. These

25

three reflections are the most suitable for practical stress measurement. Other reflections do not exhibit a linear response in the plastic regime, and do show a residual lattice strain.

A typical example for residual strain measurement in an anisotropic material was given by Holden and co-workers [Holden 1988]. The residual strains in a bent INCOLOY-800 tube were measured using monochromatic neutron diffraction. It was found that there are marked and systematic differences in the amount of strain in grains with a [001] direction aligned along the axis of the tube and those with a [111] direction aligned along the tube axis (figure 2.7). Their model calculations show that these differences originate in the different yield points and elastic moduli for different crystallographic directions.
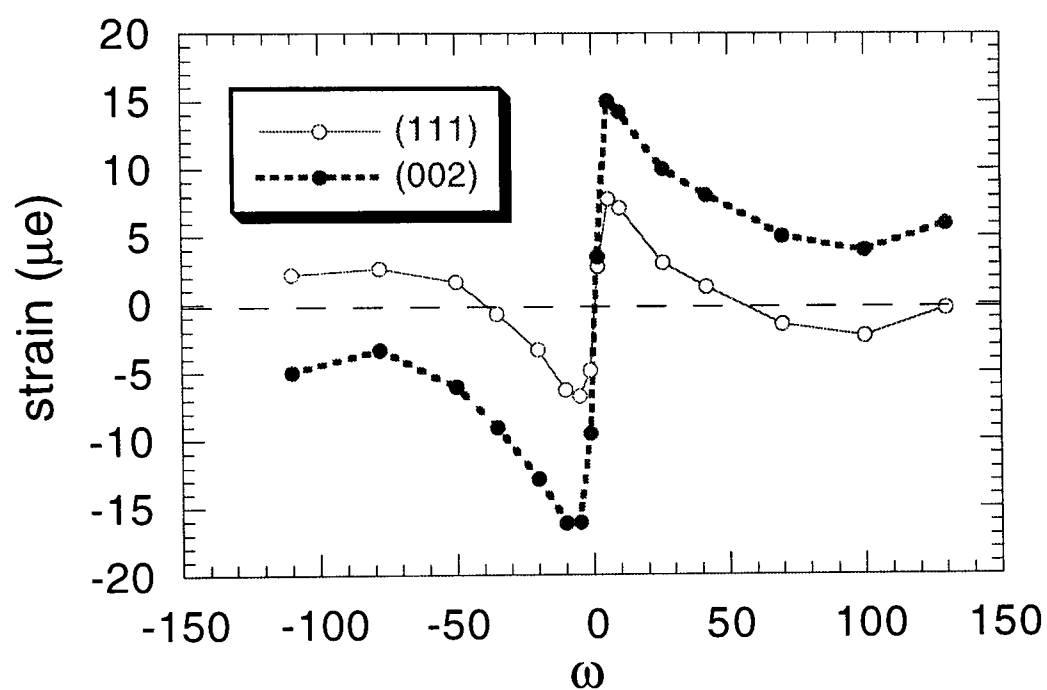
Figure 2.7 Residual strain determined by neutron diffraction in the axial direction in INCOLOY-800 tube vs angular position, ω, around the tube circumference. Large differences are observed between the strains measured with different reflections.

The measurements on annealed mild steel have revealed interesting behaviour of the lattice strain on entering the plastic regime as the stress exceeds the yield point [Allen 1989]. The (211) Bragg peak measured by time-of-flight on the High Resolution Powder Diffraction Diffractometer at ISIS, has shown that at low stresses the peak shape is limited by the instrumental resolution, and the strain increases linearly with stress. At 250 MPa, the yield stress, there is significant relaxation in the strain, and above this stress the peak broadens rapidly showing increase in microstrain. This general behaviour is

exemplified by figure 2.8, which shows the lattice microstrain response both parallel and perpendicular to applied tensile and compressive stresses of the (310) reflection. Relaxation is observed in both directions, and the microstrain increases with stress in the plastic regime. Different reflections are found to exhibit different relaxation, which clearly depends on the amount of slip allowed by neighbouring grains, and on the anisotropy of the grains.
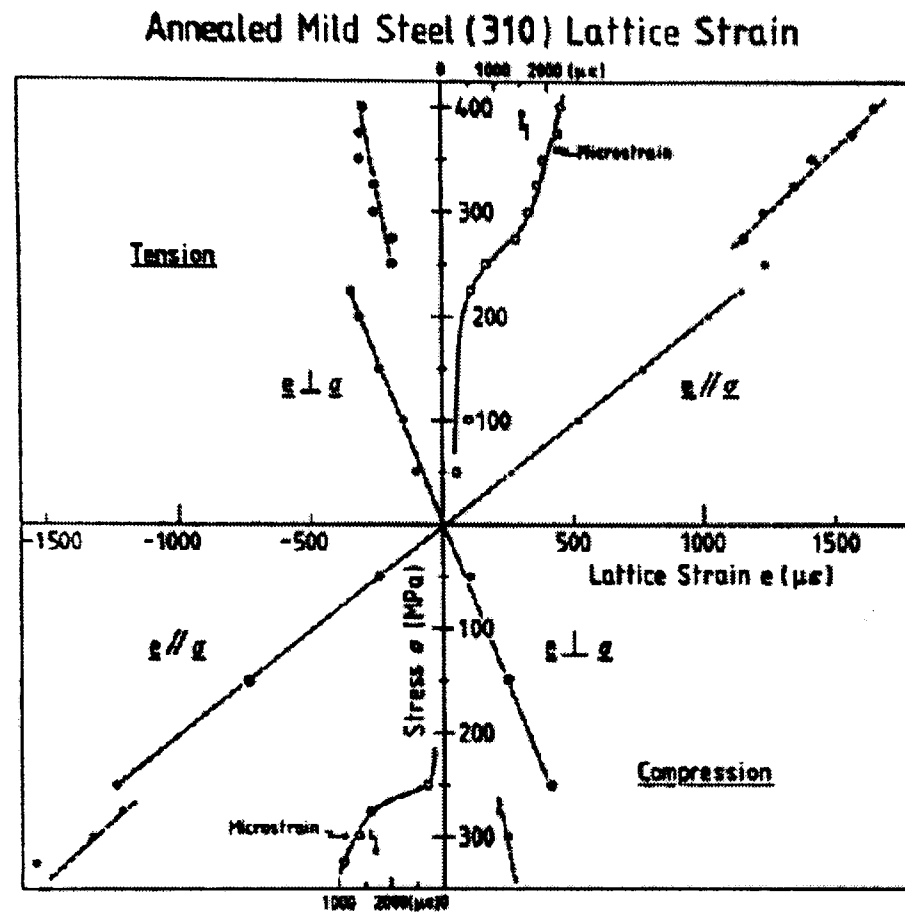
Fig. 2.8 The lattice macrostrain response from the (310) Bragg reflections in annealed mild steel, measured parallel and perpendicular to applied tensile and compressive stress. The errors are given by the size of points. The microstrain parallel to the applied stress, as given by the full width at half maximum of the diffraction peak, is also shown [Allen 1989]

2.5.2 Engineering Measurements

2.5.2.1 Residual strain distribution in railway rails

The measurement of residual stresses in railway rails [Webster 1992] provides a typical example of an engineering problem where an indirect approach is required. Railway rails

in use are very long, their cross-section is a complex shape and in the thickest part, the head, attenuation of the neutron beam is severe.

A practical economic approach is to make series of measurements on a number of sections cut from the component, to which strain gauges have been attached before cutting, and then to deduce the stresses in the original component by calculation. Some of the original stresses will have been partially relaxed, but some of the relaxation will have been recorded by the strain gauges and if a careful choice is made when sectioning it is often possible substantially to reconstruct the original stress distribution. If necessary, confirmatory measurement may subsequently be made at chosen points on a full-sized uncut component.

The rails have been sectioned to about 10mm thickness plates. In the transverse slice the longitudinal residual stresses will have been substantially relaxed but the transverse and vertical stresses, although modified, should not differ to any great extent from those in the uncut rail. In the longitudinal plate the longitudinal and vertical stresses will have suffered the least relaxation but the transverse will have been substantially relaxed. In both sets of measurements the vertical stresses measured down the centre lines should be similar to those in the uncut rail because in neither case has the vertical dimension been reduced by cutting. On the other hand the longitudinal and transverse pairs of measurements should illustrate the extent of the relaxation caused by the sectioning [Webster 1990]

In figure 2.9 the longitudinal residual stresses measured in the plate show a characteristic and pronounced variation. There is tension in the foot and in the head with balancing compression in the web. Near the running surface at the top of the head there is a thin layer of traffic induced compression which rapidly reduces to become tension in the centre of the head. The corresponding longitudinal stresses measured in the transverse slice show minimal variation.
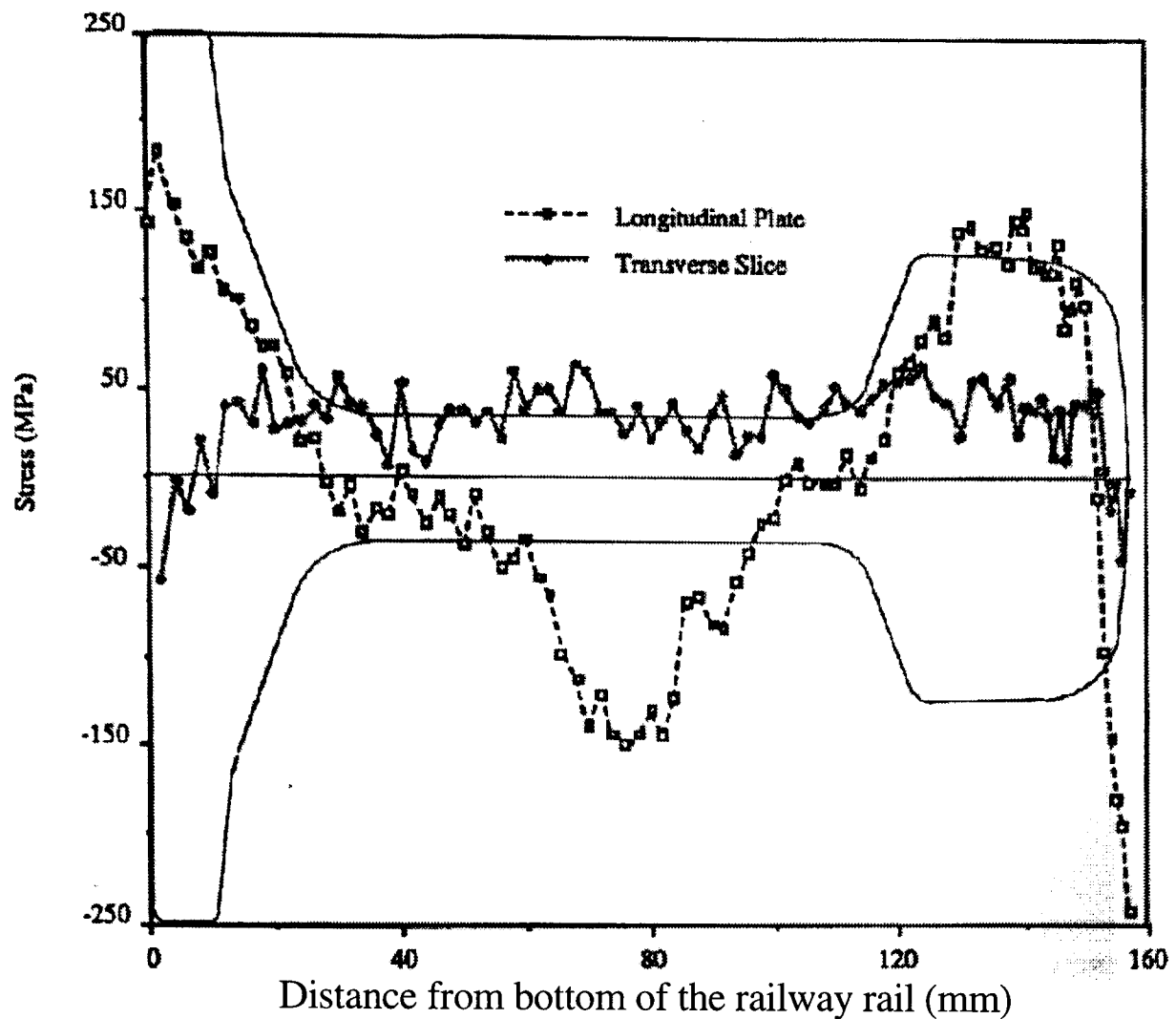
Figure 2.9 Longitudinal stresses measured down the centre-lines of transverse slice and longitudinal plate samples cut from a used railway rail.

2.5.2.2 Fatigue Cycling of a Compact Tension Specimen

A small ($31.5 \times 49.6 \times 13.1$ mm^3) compact tension specimen of BS 4360 steel was subjected to 20000 cycles of fatigue loading, with a stress intensity level varying between a minimum of K=3 and maximum of K=34 MPa mm$^{1/2}$, in order to produce a small crack of 3.6 mm length. The triaxial stress levels along the line of cracking were measured at the maximum load by bolting at the peak level, and are shown in figure 2.10. The data were taken with a gauge volume of only 1 mm^3, and used the (211) Bragg reflection [Hutchings 1990]. The stress field was found to be neither plane strain nor plane stress, states often assumed in theoretical calculations, and the peak stress levels are less than expected from theory assuming plane strain. Instrumental volume resolution could have contributed to this reduction. On removal of the bolt to give the minimum load situation, it was found that the peak level moved away from the crack tip with consequences for hydrogen or sulphur embrittlement.

29
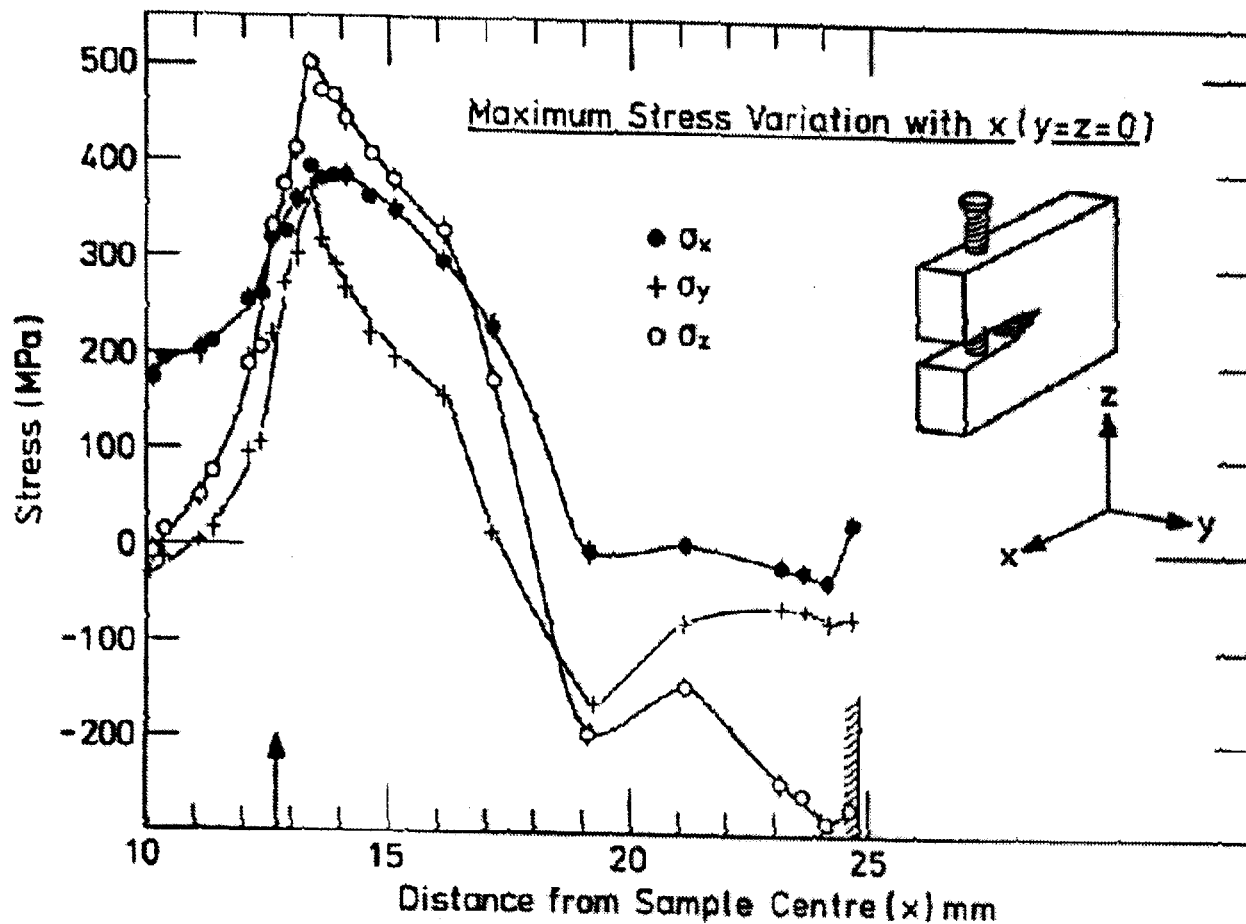
Fig. 2.10 Triaxial stress variation with position x in a cracked fatigue test specimen bolted in the maximum crack-tip stress configuration. The arrow shows the position of the crack tip on the specimen centre line, and the shaded line the outer edge of the specimen [Hutchings 1990]

2.5.2.3 Weld Components

The strain and stress variation through a section cut from a double-V weldment, fabricated from 50D C-Mn steel as shown in the inset of Figure 2.11, were measured using the (211) Bragg reflection [Allen 1985]. The dimensions of the section were 240 mm long(Y), 42 mm through the weld (Z), and 13.5 mm thick (X). In this case plane-stress should be a good approximation. The gauge volume sample was 3x3x3 mm^3, and strain data taken at 3 mm intervals were converted to stress using E=207 GPa and ν = 0.28. The resulting stress values are shown in figure 2.11. The shaded area gives the range of data taken by a destructive sectioning value of σ_z does not go to zero at the edges of the weld, although it is expected to since the stress normal to a free surface must be zero. This could be a result of an incorrect 'zero' stress reference ϕ_0 value, or the plane stress approximation used, or the fact that data could not be measured

30

actually at the surface, a potential limitation of the neutron technique except in special cases.

The d_0 problem for variable stress-free cell parameters due to metallurgical variation in weld components can be solved by using position-dependent stress-free standards [Krawitz 1994]. This method relies on the sectioning of a companion piece into small cubes corresponding to the positions of stress measurement. It has been applied to investigate the relaxation of residual stresses with postweld heat treatment in a high-performance weld [Winholtz 1995]. The measurements show that subsequent heat treatment can also alter reference cell parameter values through, for example, tempering or precipitation. The work indicates that errors in stress components as high as 700 MPa are possible in the as-welded condition. If a single constant reference standard is used for both the as-weld and postweld heat-treated conditions, both the sign and magnitude are observed to change significantly for certain components and positions.
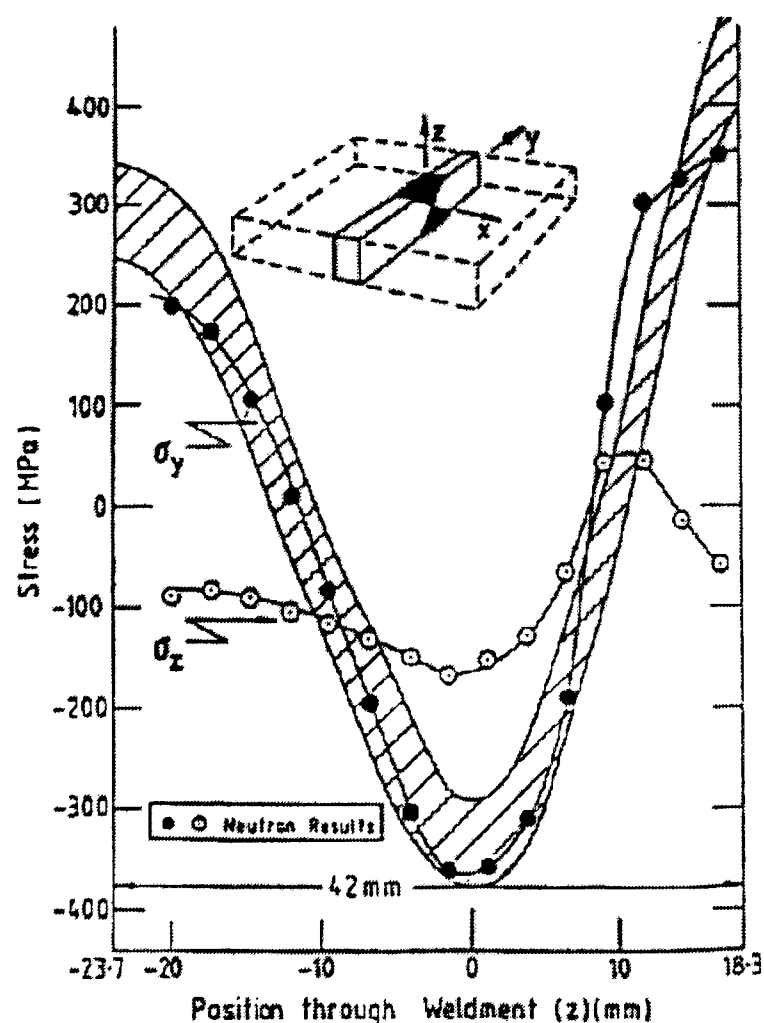
Fig. 2.11 Variation of residual stress with position through a double-V weldment sample, cut as shown in inset. The points are neutron diffraction results and the shaded area denotes the range of sectioning technique measurements [Allen 1985]

31

CHAPTER 3: INSTRUMENT DEVELOPMENT AT ISIS — ENGIN

3.1 Introduction

Commencing in 1992 the EC Brite Euram program funded a three-year project called PREMIS (PREcise Measurement of Internal Stresses within materials using pulsed neutrons). The objective of the project was to develop a routine, non-destructive method of measuring internal stresses deep within engineering materials and components by the development of a diffractometer, ENGIN at ISIS, the world's strongest pulsed neutron source.

ENGIN is a dedicated strain measurement diffractometer, incorporating, for the first time, the use of focusing collimators to achieve a sampling volume less than $2\,mm^3$, with a 2-D array of detectors to shorten data acquisition time while retaining good strain sensitivity. Two 90° scattering angles are used to enable the simultaneous measurement of strain in two perpendicular directions.

As a pulsed source the method of determining wavelength, λ is to measure the time of flight, T, of the neutron over a known flight path, L, from the source (T= 0) to sample and subsequently over the scattering path to the detector. From equation (2.37) and (2.42), one can obtain:

$$\lambda = \frac{0.003955T}{L} \tag{3.1}$$

where λ is in angstroms, T in microseconds and L in meters. The neutron wavelength and its time of flight (TOF) have a linear relationship. The neutron beam at a pulsed source is polychromatic and, using the TOF method, the wavelengths are discriminated

by their time of arrival at the detector, facilitating the measurement of different d-spacings at a fixed scattering angle.
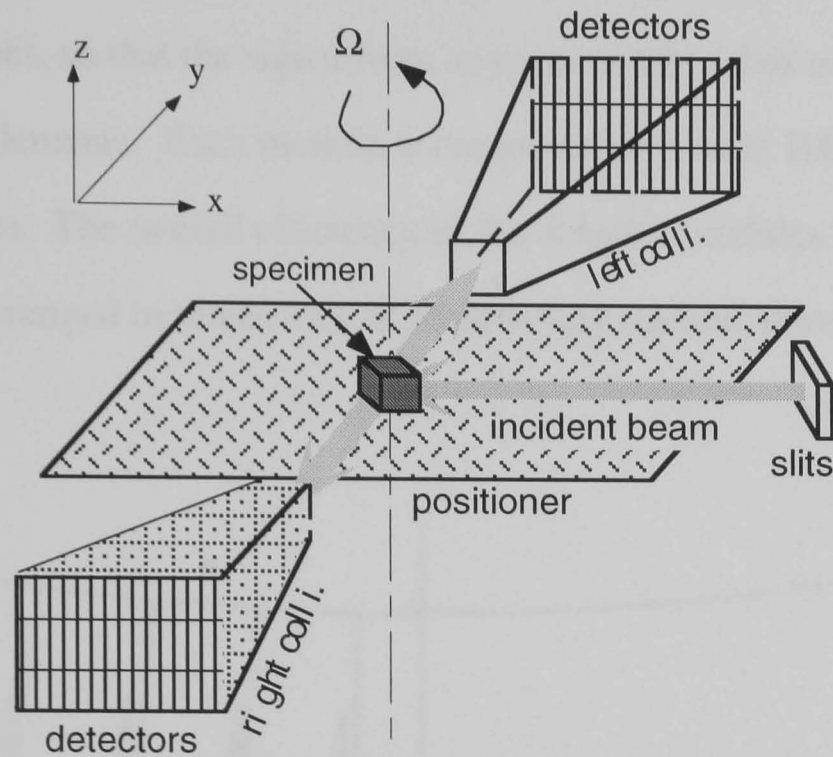
Figure 3.1 Arrangement of ENGIN's assembles

It should be emphasised that ENGIN operates in a fundamentally different manner from the conventional reactor-based counterparts. Instead of measuring Bragg reflections by scanning a detector from low to high 2θ scattering angles, ENGIN uses the pulsed white beam nature of ISIS to measure Bragg reflections at fixed scattering angles ($2\theta = 90°$), monitoring the time of arrival of the neutron after the initial neutron burst produced in the target.

3.2 Collimators and Detectors

There are two collimators (figure 3.1). Each has 40 gadolinium oxide coated mylar foils giving 41 line of sight paths for neutrons. The detector area is 230 mm by 300 mm, and is shielded by boron carbide (figure 3.2).
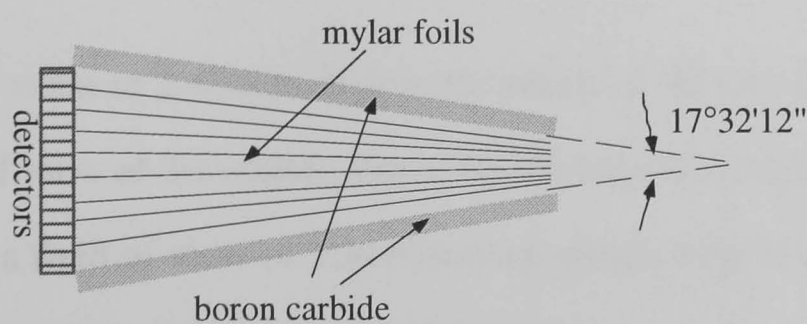
Figure 3.2 Structure of collimator

The detector is constructed by a fibre coupled V-shaped scintillator (figure 3.3). The detector modules possess 5 mm resolution. The 45 elements are $2C_n$ coded into 10 photo multiplier (PM) tubes, so that the signal from any pair of PM tubes uniquely specifies one of the 45 detector elements. Each module is composed of 3 units 100 mm high, each with 45 detector elements. The overall efficiency of the detector modules is 50% at 1 Å. There are 135 detectors arranged in three rows of 45 detectors stacked above each other behind both collimators.
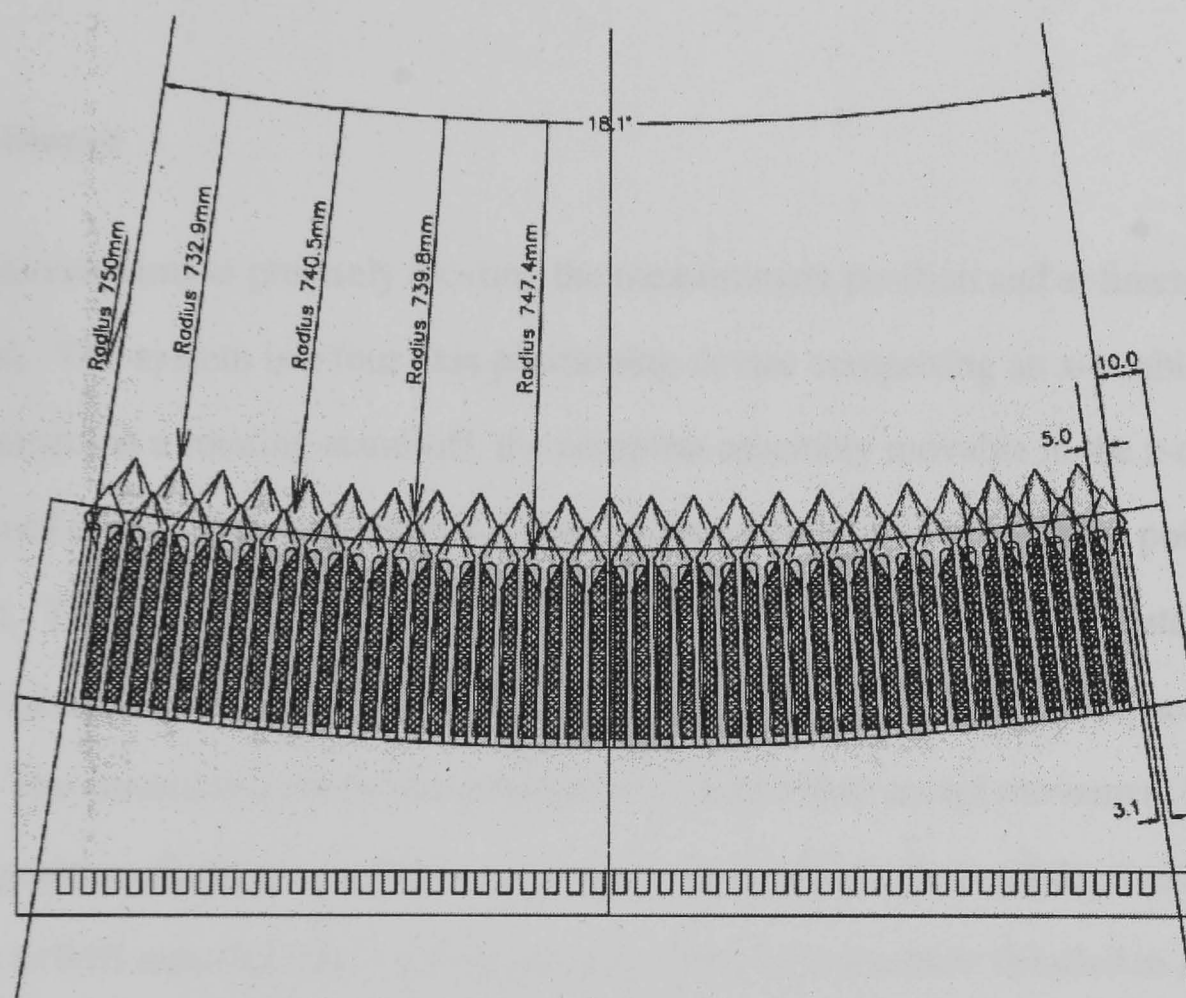
Fig. 3.3 Structure of the detector bank

The collimators' spatial resolution was measured by scanning a 3.2 mm iron rod across the front of the collimator in 0.5 mm steps, at each stage summing the count from all 40 detector elements over a range encompassing the <110> iron peak, and normalising this to the total number μA-hrs in the run as shown in figure 3.4.

This gives a FWHM value of 2.45 mm, before the width of the iron rod is deconvoluted. Assuming the field of view of the collimators to be effectively triangular, deconvolution of the iron rod gives a field of view of 1.34 mm from which 80% of the neutrons are seen, and a total width of the field of view of 3.3 mm.

34
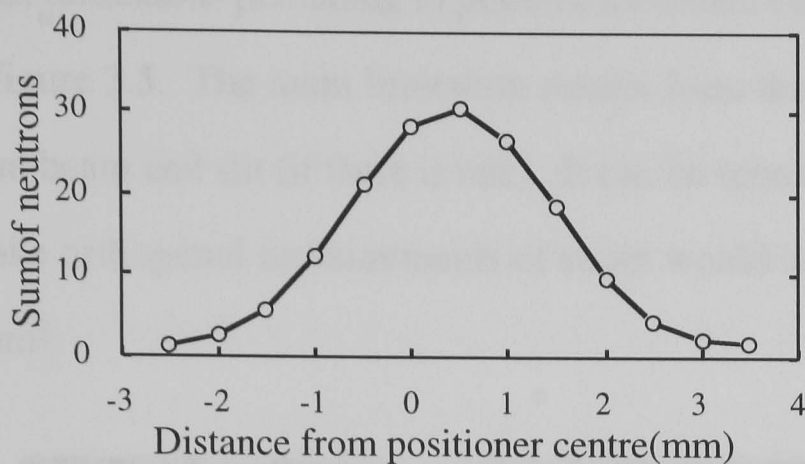
Fig. 3.4 Measured spatial resolution of the collimator

3.3 Positioner

The positioner aims at precisely locating the measurement position and at functioning auto-scan. The system is a four axis positioning device comprising an x-y table (Figure 3.1) mounted on a rotating stand-off, the complete assembly movable in the z-direction by a geared drive. The x-y table has 125 mm of movement about the centre point in each direction. The z drive has a total of 250 mm movement and the maximum distance between beam line and positioner is 300 mm in the z-direction. The load capacity is 250 kg. The control system for the positioner is modified to accept movement inputs and outputs position displays in millimetres for x, y and z dimensions and degrees for Ω, accurate to 0.01 mm and 0.01°, which are controlled by commands detailed in Appendix 2. The movement of the positioner has also been designed to reduce the acceleration forces felt by the sample using s-curve profiling of programmed or jog moves.
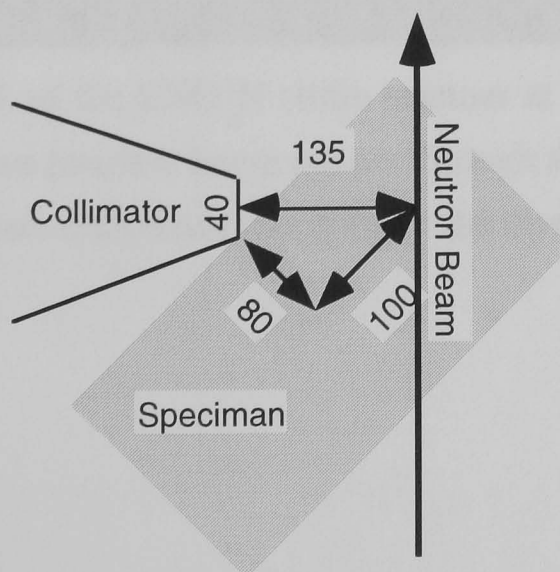
Figure 3.5 Physical space limits

The physical spatial limitations pertaining to putative specimen components and structures are illustrated in figure 3.5. The main limitation results from the proximity of the collimator, incident beam and slit (if there is one). It can be seen that the largest body that can be used to make orthogonal measurements of strain would have dimensions 160x160x300+ mm³.
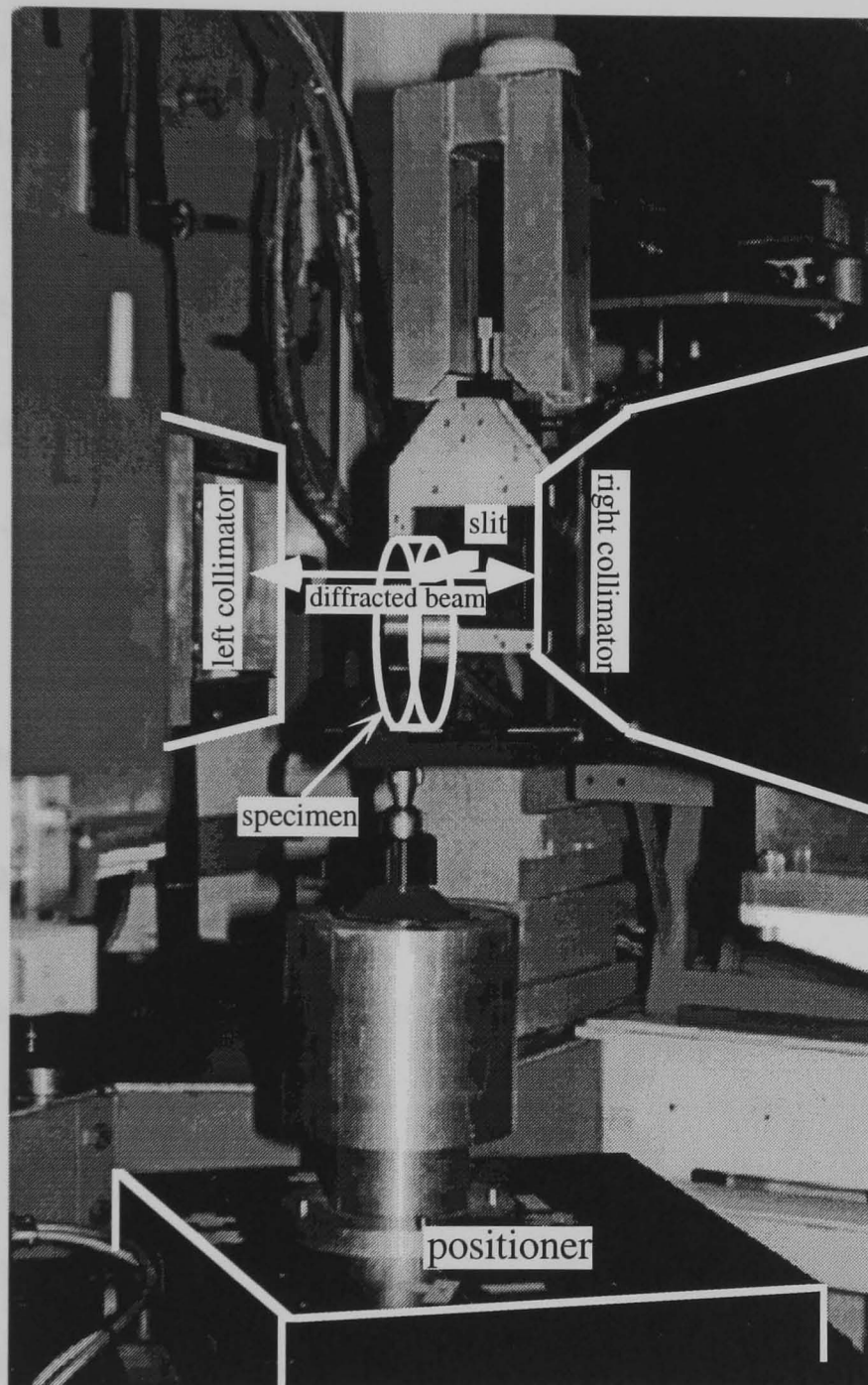
Figure 3.6 Photograph of the ENGIN strain scanner at ISIS. The "white" beam from the slit as an incident beam passes through the specimen (a ring) and is diffracted into two collimators locating at the directions perpendicular to the incident beam.

3.4 Collimating the Beam

The beam collimation is provided by a pair of orthogonal mounted fixed slits made from sintered boron carbide. A range of slit size has been made, allowing a wide range of square and rectangular beams to be provided. The whole assembly is cantilevered from a linear translation stage and has a small overall area, so that it can be brought very close to the sample. For large samples if the sample surface is 45° to the slit frame the minimum distance between the slit and the measurement point is 30 mm. No vibration can be transmitted to the slit assembly as translation of the slits is performed by a stepper motor system, which can be moved under command file control if necessary.

The hardware of the ENGIN has been described in the above. A photo of ENGIN is shown in figure 3.6.

3.5 Beam Characteristics

3.5.1 Beam Divergence Angle

The divergence angle of the incident neutron beam at ENGIN is given by

$$\Theta \sim \frac{(W+w)}{L} \tag{3.2}$$

where w is half width of the slit near the sample, W is the half width of the slit at the moderator and L is the distance between the two slits (Figure 3.7).
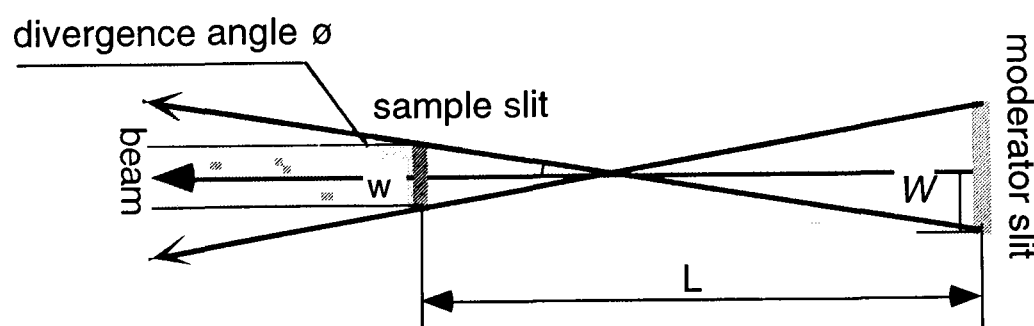
Figure 3.7 Calculation of beam divergence angle

For ENGIN, L=13595 mm, W=40 mm and w=1 mm. So, $\Theta = \frac{41}{13595} = 3\times10^{-3}$ (rad.)

This suggests that the slit should be moved to specimen as close as possible to avoid the

37

beam divergence. However, the divergence angle may be smaller than this if more slits are put into the incident beam.

3.5.2 Intensity of the Incident Beam

The maximum size of incident beam is about 20x20 mm^2 which defined by the guide-tube size between sample and the moderator. The incident beam intensity is wavelength-dependent and relies on type of moderator as shown in figure 3.8. One can see that there are more neutrons in 1-4 Å region for the methane 4 (CH_4) moderator than for water moderator.
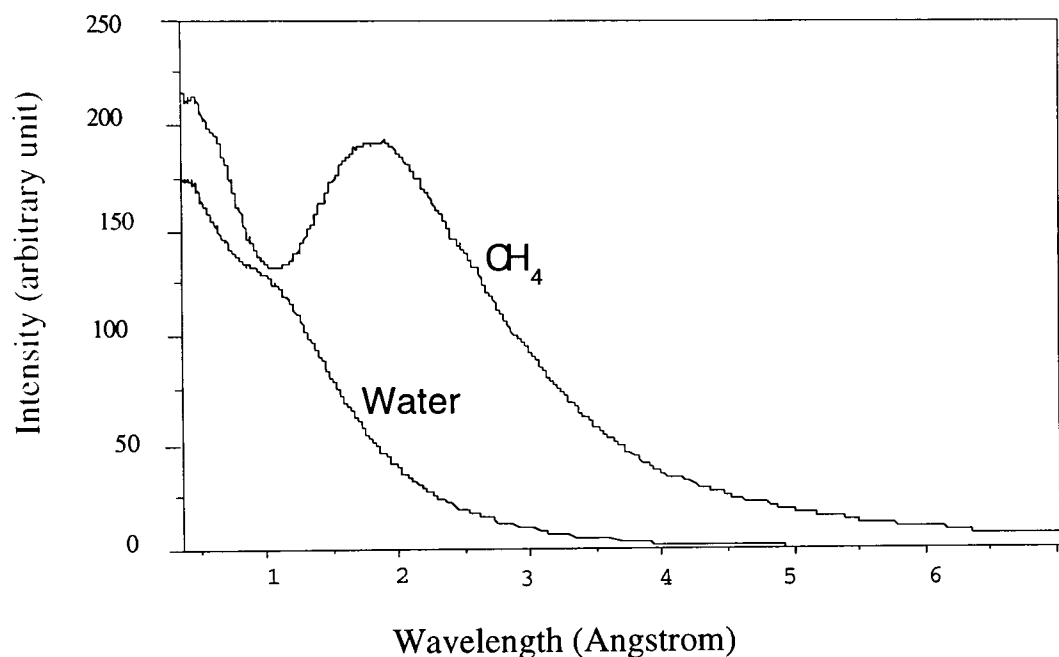
Fig. 3.8 Comparison of the intensity of the incident beam using different moderator: water and methane

3.6 Software

3.6.1 Instrumental Control and Data Acquisition

On PREMIS software was developed for the control of all the procedures involved in data acquisition and analysis of spectra on ENGIN. The control system consists of three sub-systems: data acquisition; positioner; and slit control systems. All the commands can be operated in the local VAX computer environment and the latter two also can be operated locally with control panels.

ENGIN instrument control and data acquisition are performed by a Micro VAX 3200 workstation, known as the Front End Microcomputer (FEM). The current instrument settings are contained in a file known as the Current Run Parameter Table (CRPT) and whilst a run is in progress the data is temporarily stored in the Data Acquisition Electronics (DAE). Once ending a run the contents of the CRPT and DAE are written to a data file on the FEM which is automatically archived to optical disk, part of the central VAX8650 (HUB) computer system. Each of file transfer is facilitated by a cluster system which joins the FEM and the HUB via an ETHERNET link.

Full analysis of ENGIN data is possible using either the TEB 3200 or the HUB computer from a local or remote terminal. It should be noted that inspection of data of a current run is only permitted if the user is logged on as [TEB] on the FEM computer. Outside of this special case, data can be inspected from the user's own account following the installation of a suitable login procedure. All data display and reduction programs simply use the run number for reference. The raw data file must, however, be on disk. Recent data sets are stored in TEB$DISK0:[TEBMGR.DATA] whereas older data may need to be restored from optical disk.

3.6.2 Data Display and Manipulation – GENIE

GENIE is a data display and manipulation software package that is standard for all instruments at ISIS. A full explanation of GENIE is available [David 1986]. The GENIE program allows modification of experimental spectra, such as the addition of spectra and major features such as model fitting and external user-definable functions which are of particular use with ENGIN data.

3.6.3 Data Analysis

The task of the data analysis software is to get precise information from experimental results. To achieve this the first task is to create focused data files from each of the individual detector elements to the single spectrum in which the individual spectrum is shifted so that peaks from a standard sample (silicon or CeO_2 powder) of each element are made to lie upon one another and the final single spectrum has to be normalised by vanadium spectrum for intensity balance of individual peak.

After focusing, the data can be analysis either by one of the Reitveld methods [Young 1993], Pawley technique [Toraya 1993], utilising a suite of "in-house" written and supported programs based on the Cambridge Crystallography Subroutine Library (CCSL) for pattern fitting or by profile refinement in GENIE for only single peak fitting. The former is basically a least square fitting method and was simplified for cubic-structure powder refinement for ENGIN, which has been modified to provide a set of interactive command files operating within GENIE in order to calculate the position, the height and the width of each peak as well as lattice parameters. The programmes in this thesis called CAILS (Cell And Integrated intensities Least Squares) are controlled by different cards, by which the fitting model is defined in various parameters, such as background, peak scale, cell parameters, isotropic widths, anisotropic widths and zero/anisotropic shift, etc. These programs in batch mode enable many runs to be analysed in one batch, up to ten ranges of time-of-flight, with selectable options for the refinement procedures of the parameters mentioned above. Typical crystal data file can be seen in Appendix 2 and detailed data analysis precedure can be found in Appedix 5.

3.7 Calculation of Intrinsic Resolution of ENGIN

3.7.1 Introduction

The resolution of a diffractometer, $\Delta d/d$, is a measure of the spread in the Bragg reflection for a given d-spacing, and is of paramount importance in determining its overall quality. On a time-of-flight diffractometer using equation (2.43),

$$d = \frac{ht}{2mL\ sin\theta} = f(t, L, \theta) \tag{3.3}$$

Mathematically [Windsor 1981], one can differentiate this expression with respect to each variable, giving the change Δd caused by a small change in each variable, Δt, ΔL and $\Delta \theta$

$$\Delta d = \frac{\partial f}{\partial t}\Delta t + \frac{\partial f}{\partial L}\Delta L + \frac{\partial f}{\partial \theta}\Delta\theta \tag{3.4}$$

so that,

$$\Delta d = \frac{h}{2mL sin\theta}\Delta t - \frac{ht}{2m sin\theta L^2}\Delta L - \frac{ht\ cot\theta}{2mL}\Delta\theta \tag{3.5}$$

If one assumes that all of the variables act independently, the overall resolution is

$$\frac{\Delta d}{d} = \left[\left(\frac{\Delta t}{t}\right)^2 + (cot\theta\Delta\theta)^2 + \left(\frac{\Delta L}{L}\right)^2\right]^{1/2} \tag{3.6}$$

It has three major contributions: a time uncertainty, Δt; an angular uncertainty, $\Delta\theta$ and a flight path uncertainty, ΔL.

3.7.2 Time Uncertainty

The main contribution to Δt is the moderation time of the neutron. The mechanism of neutron production and moderation at a spallation source is a complicated process and, thus, it is not surprising that the pulse shape is of a complex nature [Ikeda 1985]. Furthermore, the FWHM (full width half maximum) of the skew shape of neutron

41

moderation is dependent on wavelength as seen in Figure 3.8 [Taylor 1984]. A second factor affecting the time uncertainty in time-of-flight measurements is the channel width Δt_{ch}. This always has a square distribution $n_2(t)$. For the purpose of this calculation, it is assumed that the distribution of moderated neutrons and channel neutrons are normalised Gaussians, so the convoluted distribution from summing the two Gaussians has a FWHM of [Windsor 1981]

$$\Delta t = \left[\Delta t_m^2 + \frac{8\ln 2}{12} \Delta t_{ch}^2 \right]^{1/2} \tag{3.7}$$

From Figure 3.9, it can be seen that the FWHM of moderated neutrons is 28 µs at 15 MeV (equivalent to a wavelength of 3 Å) and as $\Delta t_{ch} = 5$ µs for ENGIN, the time uncertainty is 28.2 µs.
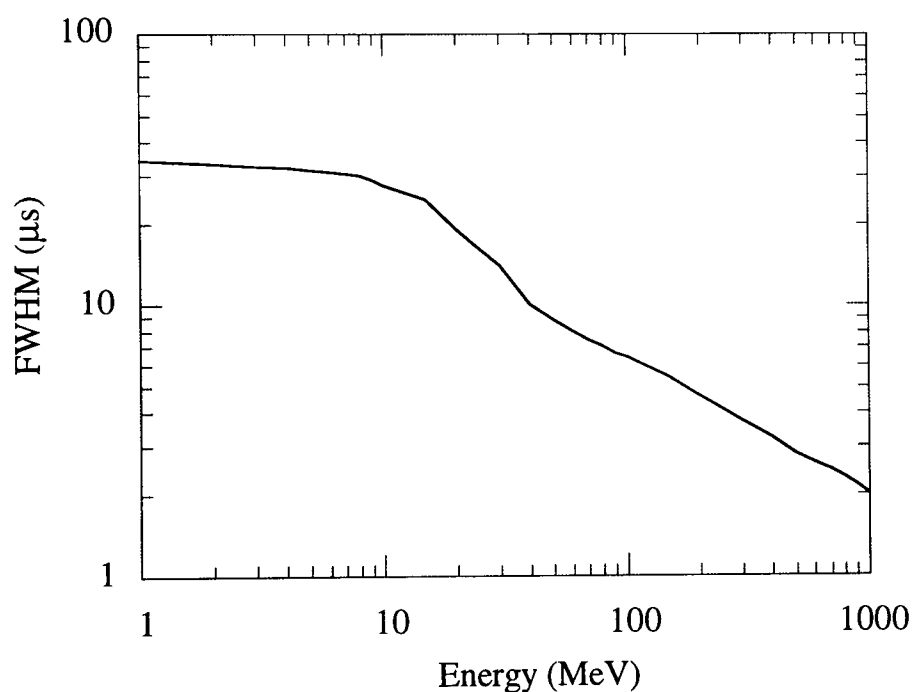
Figure 3.9 The predicted FWHM of the six faces of the SNS moderator based on Monte Carlo calculation as a function of energy [Taylor 1984]

3.7.3 Flight Path Uncertainty

The error in flight path arises chiefly due to finite size of the sample and detector. It does not include a contribution from the moderator thickness which has been conventionally included in the definition of its pulse duration Δt_m. For a rectangular sample with dimensions 2b across the beam and thickness 2a, the RMS (root mean square) distance spread is

$$\Delta L_s = \frac{1}{\sqrt{3}} \left[b^2(\sin 2\theta)^2 + a^2(1-\cos 2\theta)^2 \right]^{1/2} \qquad (3.8)$$

So if $b = 0.7$ mm (The collimators at ENGIN have an 1.4 mm resolution along beam), $a = 5$ mm, equivalent to $1.4 \times 1.4 \times 10$ mm^3 gauge volume, $2\theta = 98°45'$ then $\Delta L_s = 2.8$ mm.

3.7.4 Angular Uncertainty

The uncertainty in (half) scattering angle is a consequence of neutron beam divergence. For the purposes of this calculation the contribution to the resolution function due to beam divergence has been ignored. In consequence, the resolution increases linearly with flight path, and the maximum resolution is obtained in backscattering geometry with $\theta = 90°$ i.e. $\cot\theta \rightarrow 0$. However, the detector's angular uncertainty can not be ignored, which is

$$\Delta\theta_D = \frac{\text{detector width}}{\text{distance (sample to detector)}} \qquad (3.9)$$

$$= \frac{5}{750} = 6.7 \times 10^{-3} \text{rad}.$$

The radial collimator does not change the angular uncertainty since it has the same angular divergence as the detectors. Moreover, for a given flight path the resolution for a time-of-flight diffractometer is almost constant. This resolution characteristic is extremely important since the extraction of the maximum resolution information is not favoured at one, restricted, high resolution region of the diffraction pattern.

3.7.5 ENGIN Resolution

Thus the resolution of ENGIN is estimated as:

$$\frac{\Delta d}{d} = \left[\left(\frac{28.2}{8183}\right)^2 + (6.7 \times 10^{-3}\cot(49°22'30''))^2 + \left(\frac{2.8}{15000}\right)^2 \right]^{1/2} \qquad (3.10)$$

$$= [(3.4)^2 + (4.4)^2 + (0.19)^2]^{1/2} \times 10^{-3}$$

$$= 5.6 \times 10^{-3}$$

Analysis of equation (3.10) shows that the angular uncertainty of the detector and the time uncertainty from the moderator have the strongest effect on the resolution of ENGIN. The resolution of ENGIN has been calculated to be 5.6×10^{-3}, which is comparable to that of both HRPD (2×10^{-3}) and POLARIS' (6×10^{-3}) [Boland 1992]. Ways of improving the resolution would be to decrease the size of individual detector modules or to improve the performance of the moderator.

In the above calculation, the following factors have not been taken into account:

- The variables in Equation (3.5) may not be independent.

- The effect of detector thickness

- Focusing errors

However, it is important to realise that the resolution of ENGIN does not mean that one can measure the strain to only 5600 $\mu\varepsilon$. The resolution tells when peak overlap may occur. The strain sensitivity [Lorentzen 1991] of ENGIN is orders of magnitude much better than the instrumental resolution, and is typically of the order of $\pm5 \times 10^{-5} \sim \pm1 \times 10^{-4}$ which is 50–100 times smaller than the FWHM of an individual Bragg peak.

3.8 Validation of ENGIN — Comparison of Strain Measurement in a Plastically Compressed Ring with that from Other Sites

In order to compare measurements on ENGIN to those made at other neutron diffractometers, strain distribution in a ring, which has previously been analysed by FE (finite element calculation) and measured at LANSCE and at CRNL, has been determined using ENGIN. The ring is described in detail in reference [Holden 1992]. It is a diametrically compressed ring with single phase austenitic stainless steel (21Cr-6Ni-9Mn). A special thermomechanical procedure has been used for fabricating the plate materials which resulted in mean grain size of about 25.3 μm, no precipitates of second phase particles and no preferred orientation.

The area analysed was at the west arm of the ring in the hoop direction as shown in figure 3.10. The gauge volume used was 2x2x4 mm^3. All ENGIN data was refined for the parameters: background, peak scale, cell parameters, isotropic widths, anisotropic widths except correction for cubic anisotropic. The result compared with that from other sites is plotted in figure 3.10. It can be seen that these measurements agree well each other.
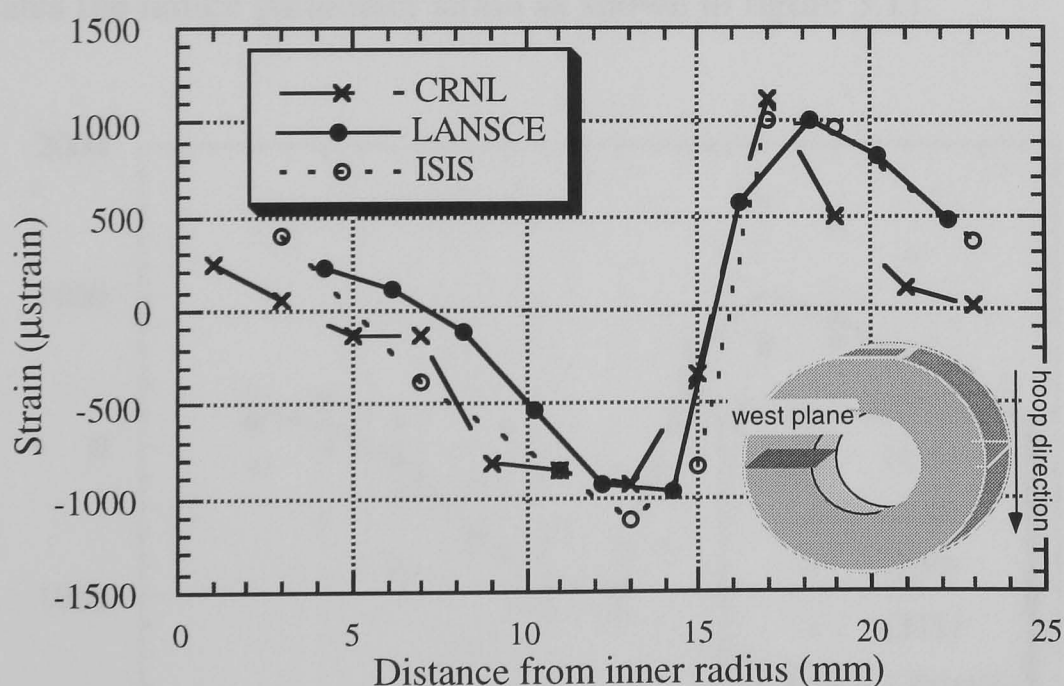
Figure 3.10 Comparison of strain measurements from different neutron sources. The typical statistical error is ±50 $\mu\epsilon$.

3.9 Lattice Parameter Strain

Since ENGIN is an energy-dispersive neutron spectrometer, the strain is obtained by refining whole pattern of spectrum using either Rietveld refinements, or Pawley method, which is a method using least squares minimisation procedures, we define it as LP (lattice parameter) strain. The least squares minimisation procedures aim at making a good fit to the spectrum using the chi squared value, χ^2 statistic [David 1992]:

$$\chi^2 = \frac{1}{N-P+C}\sum_i w_i[Y_i(obs)-Y_i(calc)]^2 \qquad (3.11)$$

where N is the number of observations; P is the number of variables; C is the number of constraints and w_i is a weight function of standard deviation, $\frac{1}{(standard\ deviation)^2}$. If we consider the anisotropy of a material, every peak might shift a different amount under load as the compliance of a material is direction-dependent. Using Pawley refinement without considering anisotropy results in the stronger and more-shifted peak with less standard deviation contributing more to the lattice parameter strain, which can be derived from equation (3.11). For example, the lattice parameter strain of hoop direction in the ring is decided by the four biggest peaks, (111), (200), (220) and (311). Thus those peaks dominates the lattice parameter strain as shown in figure 3.11.
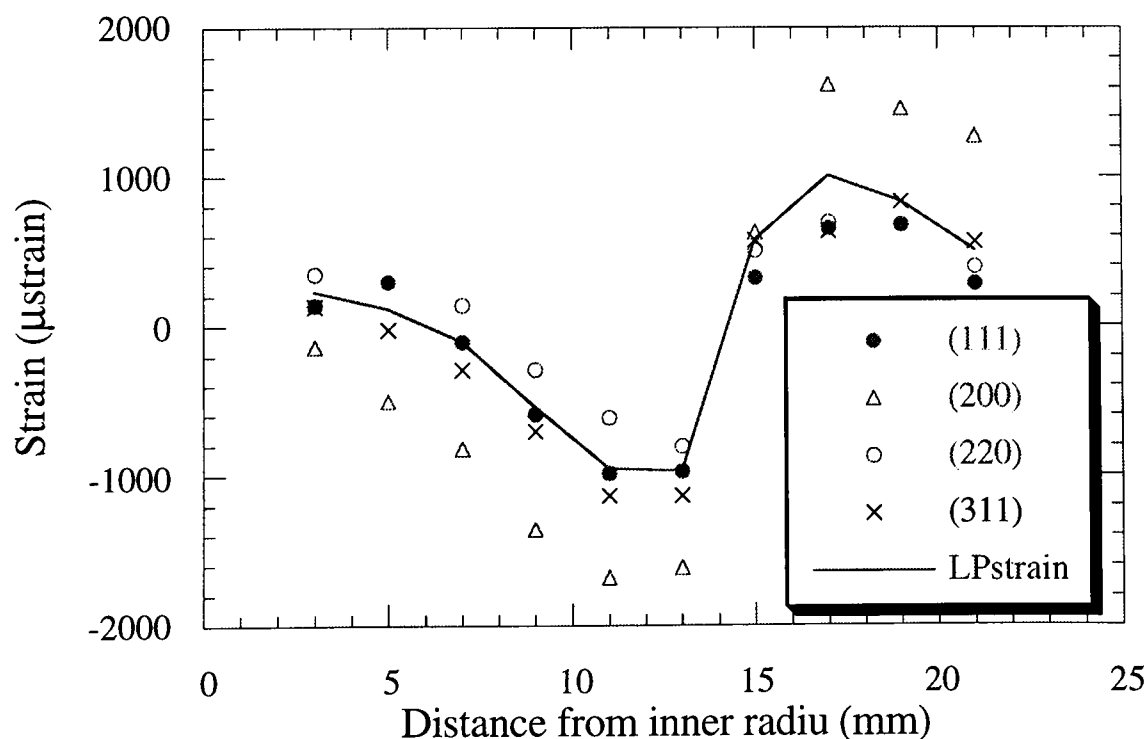
Figure 3.11 Comparison of lattice parameter strain and the strains derived from individual reflections [Bourke 1991].

It is well known that the difference of peak shifts depends on the degree of anisotropy of materials. The degree of anisotropy of material is given by [Windsor 1991]:

$$A' = \frac{2(S_{11}-S_{12})}{S_{44}}$$ (3.12)

where S_{ij} is the single compliance constant of the material. The anisotropy of aluminium is negligible as its degree of anisotropy is 1.2, which is very close to isotropic materials ($A' = 1$) and is much less than iron (≈ 2.5). In fact the LP strain is dominated by an "averaging" over several principal reflections locating in the region of 0.9-2.5 Å due to the Maxwellian distribution of neutron intensity at ISIS (see figure 3.8 and chapter 2.3.1), in which there are (200), (220), (400), (331) and (422) reflections for aluminium; and (211), (220), (310), (321) as well as (330) reflections for iron. Among them the (211), (220), (321) and (330) reflections in iron are the best reflections for stress measurement as those reflections have the same anisotropy factor [Hutchings 1991]:

$$A_{hkl} = \frac{(h^2k^2+h^2l^2+k^2l^2)}{(h^2+k^2+l^2)^2} = 0.25$$ (3.13)

and they exhibit a linear response even in the plastic regime. Of course one should use the lattice parameter strain with caution if there is a strong texture in the materials.

CHAPTER 4: NEAR-SURFACE STRAIN MEASUREMENT

4.1 Introduction

It is important to measure near-surface strain for the characterisation of some surface treatment techniques such as shot-peening and coating, as near-surface residual stresses significantly affect the fatigue life of components. X-ray diffraction is a common tool to measure near-surface stress, but even when it is used destructively by layer removal it is limited to a depth ≈ 100 microns at most [Ruppersberg 1993]. The high penetration of neutrons uniquely allows the strain to be measured deep (several cm) inside a component. As large stress gradients can occur near the surface in components, precise near-surface strain measurement is required, which involves both an accurate determination of measurement position and reduction of any systematic errors. To achieve these two objectives, attention must be paid to effects from the relatively large gauge volume and the instrumental configuration. Precise near-surface strain measurements rely on:

- precise determination of the gauge volume position relative to the sample surface

- calculation of the 'centre of gravity' of the near-surface gauge volume which depends on the shape of the gauge volume and the detected beam intensity.

- evaluation of any anomalous surface effect of the diffractometer on strain determination, which is controlled by instrument characteristics such as the collimators' and detectors' positions relative to the sample.

The following sections will discuss the above topics in detail .

4.2 A Methodology for Near-surface Strain Measurement

4.2.1 Precise Determination of Measurement Position

4.2.1.1 Model of diffraction intensity calculation

Although optical alignment aids, such as lasers, theodolites and telescopes are essential for setting up translator systems and the initial alignment of specimens, in order to obtain the highest spatial measurement precision it is necessary to use the neutron beam itself to determine surface location. The sample position is determined by fitting the data from a fast scan, which is performed as the gauge volume enters the sample, to a modelling intensity calculation . The following is the modelling calculation.

The total number of neutrons (the diffracted intensity) of a Bragg reflection measured in a time-of-flight powder diffraction experiment is given by Buras and Gerwards [1975],

$$I_{hkl} = \frac{I_0(\lambda)\varepsilon(\lambda)\lambda^4 V_s A_{hkl}(\lambda) E_{hkl}(\lambda) j |F_{hkl}|^2 \cos \Delta\theta}{4 V_c^2 \sin^2\theta} \qquad (4.1)$$

where

$I_0(\lambda)$	= incident neutron flux at wavelength λ, units of neutron neumber
$\varepsilon(\lambda)$	= detector efficiency at wavelength λ, dimensionless
$A_{hkl}(\lambda)$	= attenuation coefficient for reflection hkl, (cm^{-1})
$E_{hkl}(\lambda)$	= extinction coefficient for reflection hkl, (cm^{-1})
V_s	= sampling volume, (cm^3)
V_c	= unit cell volume, (cm^3)
j	= reflection multiplicity, dimensionless
F_{hkl}	= structure factor, (cm^2)
2θ	= Bragg angle, (degree)
$\Delta\theta$	=diffraction peak width, (degree)

Equation (4.1) is valid for a full Debye-Scherrer cone. For the case of surface scanning, taking only the diffracted volume, $V_s(x,y,z)$, and the attenuation, e^{-kl} [Bacon 1975] into account, and ignoring any incoherent scattering and texture variation, the diffracted neutron intensity is obtained as:

$$I(L) = \int_{V_s} I_i(x,y,z)\, e^{-kl}\, dv \qquad (4.2)$$

where I_i is the intensity relevant to the spacial distribution of the detected beam; k, the total attenuation coefficient given as $k = \mu + bN$, where μ is the linear absorption coefficient; b, the coherent scattering cross section of a single atom; N, atomic density of the sample; l, the path length and L, the distance from sample surface to top of gauge volume, which is a function of gauge volume size (f,g,h). The integration is performed over the diffracted volume, V_s. After fitting the modelling calculation to a rapid scanning one can then obtain the specimen surface position relative to the gauge volume.

(a)
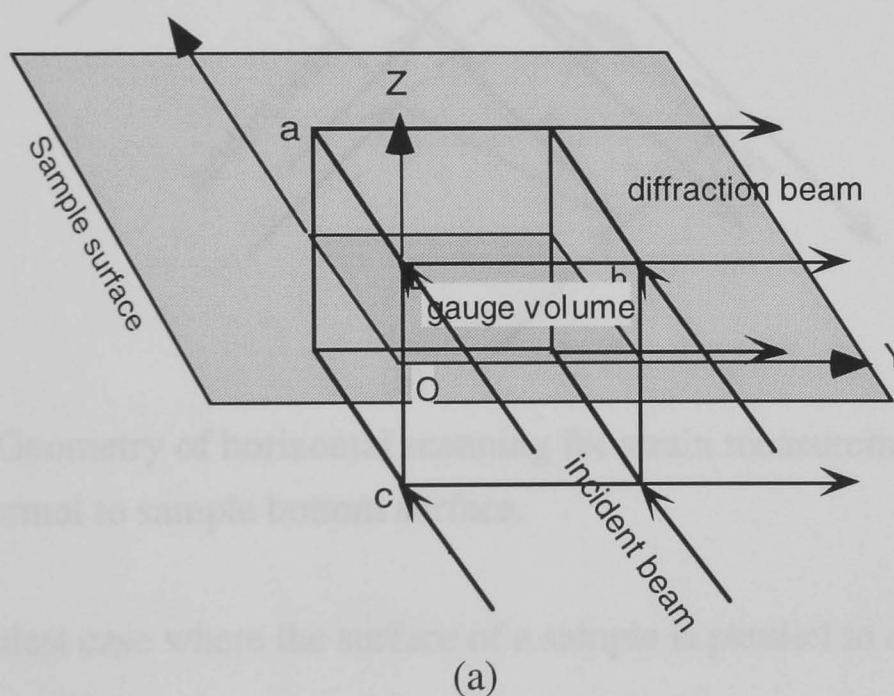
Fig. 4.1(a) Geometry of vertical scanning for strain measurement at the direction parallel to sample bottom surface

4.2.1.2 Application of the model

On ENGIN there are two principal geometries: the vertical scanning geometry (figure 4.1 (a)) represents the case where the strains measured are in the directions parallel to the

sample surface; the horizontal scanning geometry (figure 4.1 (b)), where the strain measured are in the direction perpendicular to the sample surface. Noted that the gauge volume is not cubic, which is the usual situation on ENGIN: the focusing collimators are fixed and the shape of the gauge volume is varied by changing incident beam collimation.

The spacial distribution of the detected beam intensity is a function of the gauge volume's dimensions. The FWHMs (full-width-at-half-maximum) of the detected intensities in the three dimensions are used in the calculation of the detected intensity as an approximation: two dimensions are defined by the slits, and the third dimension is a Gaussian distribution defined by the focusing function of the collimator [Wright 1994].

(b)
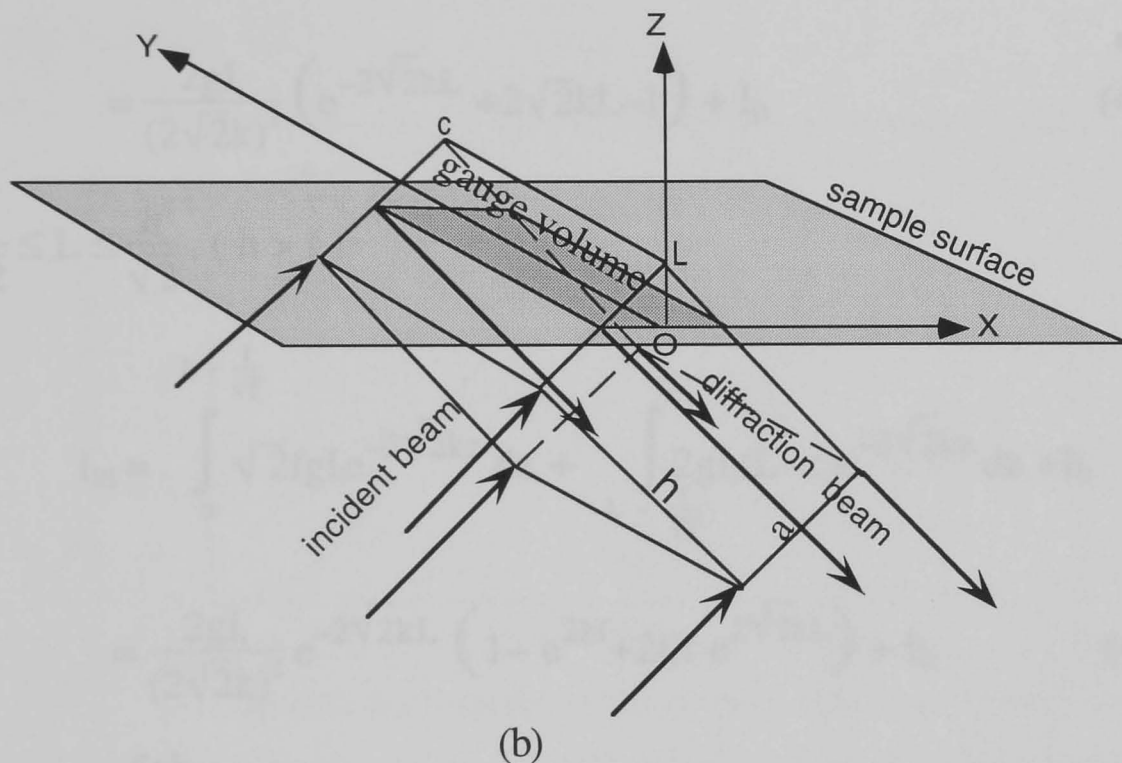
Fig. 4.1(b) Geometry of horizontal scanning for strain measurement at the direction normal to sample bottom surface.

Consider the simplest case where the surface of a sample is parallel to one of the gauge volume surfaces shown in figure 4.1(a). Accordingly the intensity $I_i(x,y,z)$ in equation (4.2) is a constant. The intensity, in terms of L, is given by

$$I(L) = I_i L \qquad\qquad (4.3)$$

where the maximum of L is the maximum dimension of the gauge volume perpendicular to sample surface. From equation (4.3) it can be seen that when the gauge volume completely enters into the sample, the detected neutron intensity reaches a maximum value providing that there is no change in texture along the L direction.

51

We can also consider the more common and complex case where the gauge volume enters into the sample from one of its edges as shown in figure 4.1(b). Calculations of the detected intensity for the case have to be performed for five different regions:

a. $L \leq 0$,

$$I_I = I_b \qquad\qquad (4.4)$$

b. $0 \leq L \leq \dfrac{f}{\sqrt{2}}$,

$$I_{II} = \int_0^L 2gI_i(L-z)e^{-2\sqrt{2}kz}\, dz + I_b$$

$$= \frac{2gI_i}{(2\sqrt{2}k)^2}\left(e^{-2\sqrt{2}kL} + 2\sqrt{2}kL - 1\right) + I_b \qquad\qquad (4.5)$$

c. $\dfrac{f}{\sqrt{2}} \leq L \leq \dfrac{h}{\sqrt{2}}$, $(h > f)$

$$I_{III} = \int_0^{L-\frac{f}{\sqrt{2}}} \sqrt{2}fgI_i e^{-2\sqrt{2}kz}\, dz + \int_{L-\frac{f}{\sqrt{2}}}^L 2gI_i(L-z)e^{-2\sqrt{2}kz}\, dz + I_b$$

$$= \frac{2gI_i}{(2\sqrt{2}k)^2}e^{-2\sqrt{2}kL}\left(1 - e^{2kf} + 2kf\, e^{2\sqrt{2}kL}\right) + I_b \qquad\qquad (4.6)$$

d. $\dfrac{h}{\sqrt{2}} \leq L \leq \dfrac{f+h}{\sqrt{2}}$,

$$I_{IV} = \int_0^{L-\frac{h}{\sqrt{2}}} 2gI_i\left[\frac{f+h}{\sqrt{2}} - (L-z)\right]e^{-2\sqrt{2}kz}\, dz + \int_{L-\frac{f}{\sqrt{2}}}^L 2gI_i(L-z)e^{-2\sqrt{2}kz}\, dz$$

$$+ \int_{L-\frac{h}{\sqrt{2}}}^{L-\frac{f}{\sqrt{2}}} \sqrt{2}fgI_i e^{-2\sqrt{2}kz}\, dz + I_b$$

$$= \frac{2gI_i e^{-2\sqrt{2}kL}}{(2\sqrt{2}k)^2}\left(1 + e^{2\sqrt{2}kL} - e^{2kh} - e^{2kf}\right) + \frac{gI_i}{2k}[(f+h) - \sqrt{2}L] + I_b \qquad (4.7)$$

e. $L \geq \dfrac{f+h}{\sqrt{2}}$,

52

$$I_V = \int_{L-\frac{f+h}{\sqrt{2}}}^{L-\frac{h}{\sqrt{2}}} 2gI_i \left[\frac{f+h}{\sqrt{2}} - (L-z)\right] e^{-2\sqrt{2}kz} \, dz + \int_{L-\frac{f}{\sqrt{2}}}^{L} 2gI_i(L-z) e^{-2\sqrt{2}kz} \, dz$$

$$+ \int_{L-\frac{h}{\sqrt{2}}}^{L-\frac{f}{\sqrt{2}}} \sqrt{2}fgI_i \, e^{-2\sqrt{2}kz} \, dz + I_b$$

$$= \frac{2gI_i e^{-2\sqrt{2}kL}}{(2\sqrt{2}k)^2} \left(1 + e^{2k(f+h)} - e^{2kh} - e^{2kf}\right) + I_b \quad (4.8)$$

The intensity was obtained for a gauge volume having dimensions 1.4x2.5x2.5 mm³, and are shown in figure 4.2.
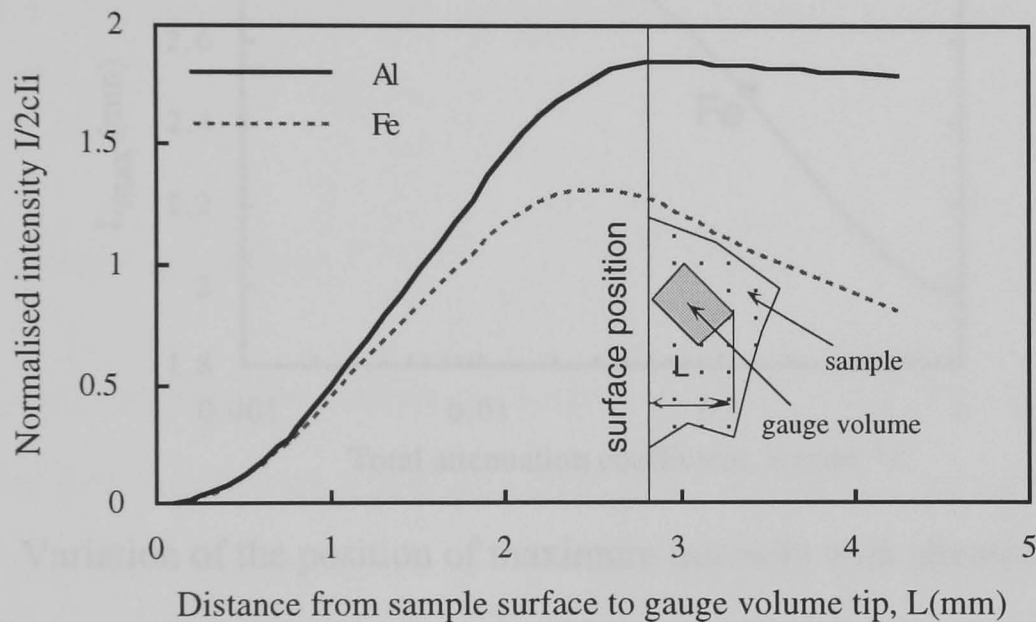
Figure 4.2 Intensity variation as a 1.4x2.5x2.5 mm³ gauge volume enters the sample surface

In region I, the background intensity, I_b, is a constant. For the region II, one can see that

$$\frac{\partial I_{II}}{\partial L} = \frac{gI_i}{\sqrt{2}k}\left(1 - e^{-2\sqrt{2}kL}\right) > 0 \text{ (when } kL > 0) \quad (4.9)$$

the intensity increases as L varies, but there is no intensity peak.

For region III, we have

$$\frac{\partial I_{III}}{\partial L} = \frac{gI_i}{\sqrt{2}k} e^{-2\sqrt{2}kL}\left(e^{2kf} - 1\right) > 0 \quad (4.10)$$

and the intensity increases monotonically as in region II. When

53

$$\frac{\partial I_{IV}}{\partial L} = \frac{gI_i}{\sqrt{2k}} \left[e^{-2\sqrt{2}kL}\left(e^{2kf} + e^{2kh} - 1\right) - 1 \right] = 0 \qquad (4.11)$$

so the distance from tip of the gauge volume to the sample surface when the diffracted intensity reach maximum value is:

$$L_{max} = \frac{\ln\left(e^{2kf} + e^{2kh} - 1\right)}{2\sqrt{2}k} \qquad (4.12)$$

The plot of the peak position of the detected intensity for different amount of attenuation is shown in figure 4.3.
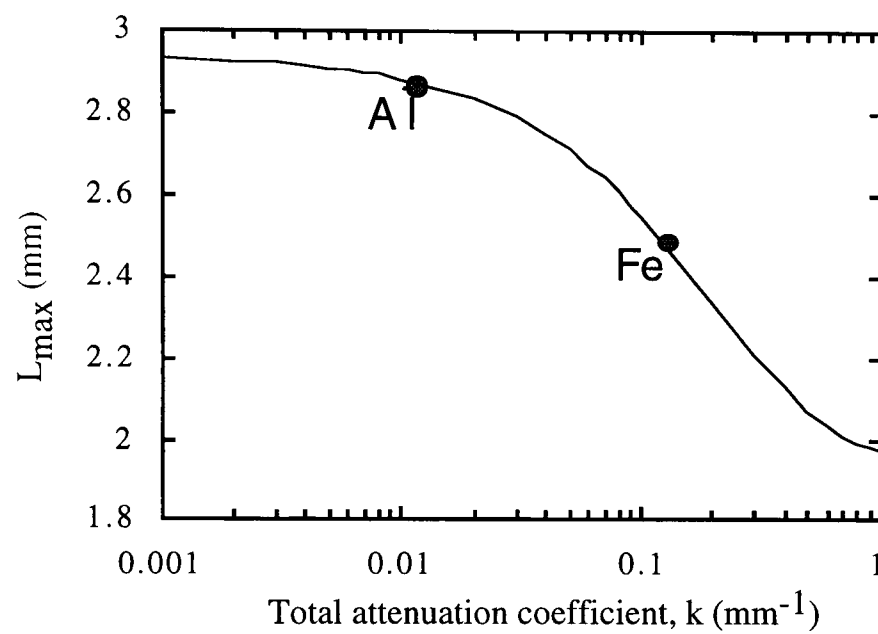
Fig. 4.3 Variation of the position of maximum intensity with attenuation.

Noted that when the detected intensity reaches a maximum value the gauge volume does not completely enter into sample. For example, for a $1.4 \times 2.75 \times 2.75$ mm^3 gauge volume in aluminium, ($k_{Al} = 9.83 \times 10^{-3}$ mm^{-1}), $L_{max} = 2.88$ mm; whilst for iron ($k_{Fe} = 0.112$ mm^{-1}), $L_{max} = 2.52$ mm; and when $L = (f+h)/\sqrt{2} = 2.93$ mm the gauge volume just immerses in the sample. The distance between the point where the detected intensity reaches a maximum value and where the gauge volume completely enters sample is ≈ 0.4 mm for iron.

In region V, the detected intensity decreases monotonically as only attenuation in the sample has an effect on the detected intensity.

Therefore, having obtained experimental data of diffracted intensity against L, the distance from surface to the gauge volume tip, the specimen surface position can be precisely determined by adjusting background and gauge volume position in a least-square fitting.
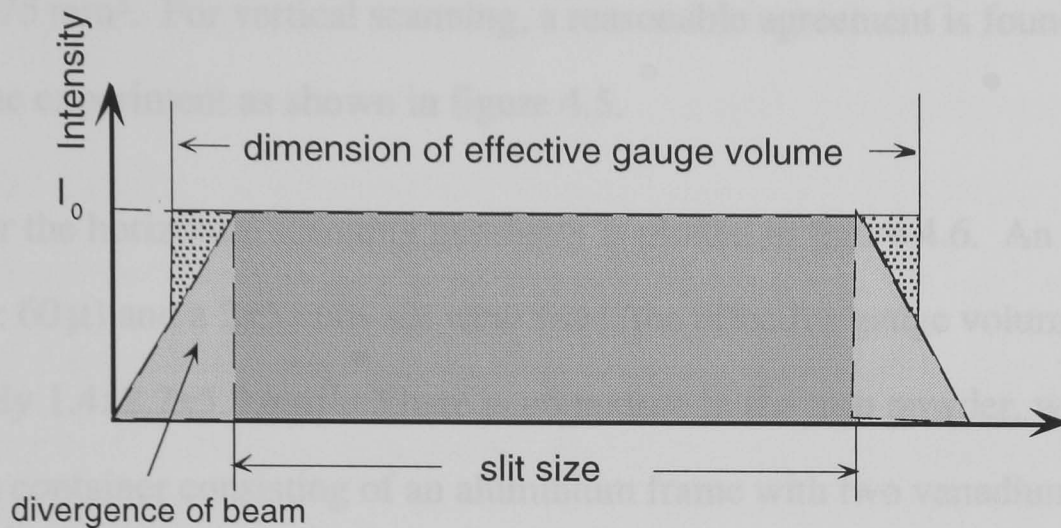
Figure 4.4 Two dimensions of the gauge volume defined by slit size.

4.2.1.3 Model validation

This model is used routinely for finding the surface on ENGIN and two examples will be given here. The first involves an aluminium plate where a $2x2$ mm^2 incident beam slit was used. Taking the beam divergence ($3x10^{-3}$ rad.) into account, a gauge volume of $2x3.5x3.5$ mm^3 is defined by the slits which are 250 mm from the sample and the collimation function.
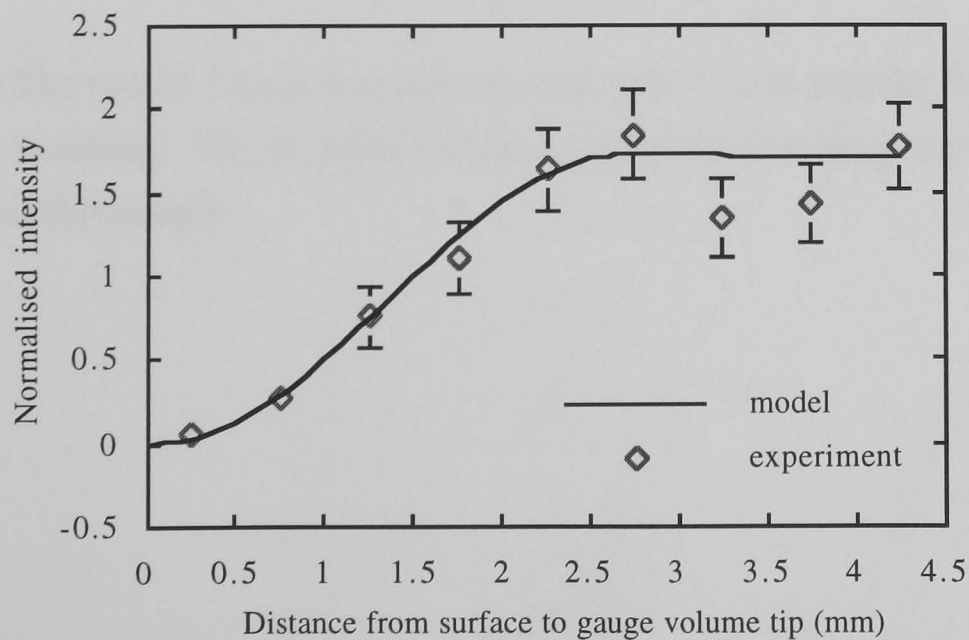
Figure 4.5 Comparison of the model and experiment for vertical scanning in aluminium.

55

To simplify the geometrical distribution of the incident beam intensity, the FWHM (full-width-at-half-maximum) of the detected intensities were used (figure 4.4) so that the spacial distribution of the detected intensity in the three orthogonal directions is assumed to have the shape of a square pulse. Hence, the effective gauge volume size is $1.4 \times 2.75 \times 2.75$ mm^3. For vertical scanning, a reasonable agreement is found between the model and the experiment as shown in figure 4.5.

The result for the horizontal scanning geometry is plotted in figure 4.6. An iron powder (particle size: 60μ) and a 2×5 mm^2 slit were used, the effective gauge volume is therefore approximately $1.4 \times 2.2 \times 5.2$ mm^3. There is no texture in the iron powder, which was placed into a container consisting of an aluminium frame with two vanadium windows. It can be seen that the model fits the experimental data well using published values of the attenuation coefficient* in both cases.
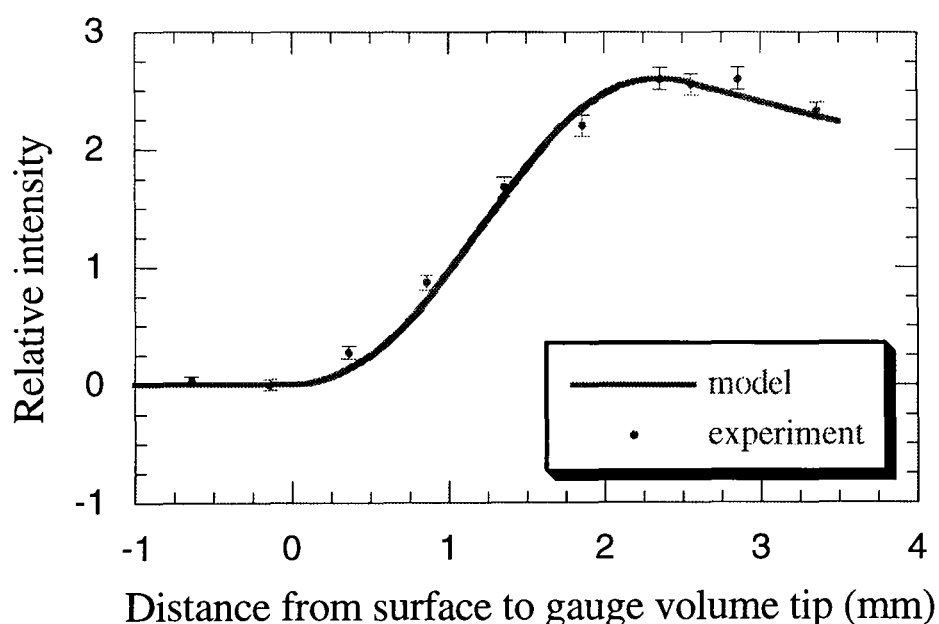
Figure 4.6 The model fitting for experimental data of iron powder for horizontal scanning. The negative distance represents that the gauge volume is outside of the sample.

---

* The attenuation coefficient for secondary extinction is an average of all peaks for ENGIN, which is approximately the value at 1.08Å. If there is a strong texture in materials, the attenuation coefficient for secondary extinction will be different.

4.2.2 Calculation of Gauge Volume Centroid

When measuring strains in components that possess near-surface strain gradients, a relatively high number of measurements need to be made. As typical gauge volume dimensions are large compared to the distances over which large strain gradients occur, then measurements are often taken with the gauge volume only partially immersed in the component and the effective measurement position (centroid) should be the geometrical centre of the immersed part. In addition, the geometrical centre for a large attenuation material is not the centroid even when the gauge volume is completely immersed in the sample. Under these conditions it is important to know where the 'centre of gravity' of the diffracting volume is.

This is achieved by calculating the centroid of this volume, which represents the effective diffraction position for strain measurement. If the gauge volume is completely immersed in the specimen, the centroid is simply its geometrical centre, provided that the spatial distribution of the diffracted intensity possesses a certain symmetry at the geometrical centre. However, when the gauge volume partially enters the specimen, the position of the centroid relies on two functions. One is the function of the diffracted volume, $V(x,y,z)$. The other is the spatial distribution function of the detected intensity, $I(x,y,z)$. The term 'detected intensity' is used here because for ENGIN the spatial distribution of the intensity depends not only on the spatial intensity distribution of the incident beam and the diffraction homogeneity of the specimen, but also on the focusing effect of the collimators. To calculate the position of the diffraction centroid, we use the fact that the total amount of diffracted neutrons in both halves of the gauge volume separated by the centroid position should be equal, and hence obtain the following equation:

$$\int_0^L I(x,y,z)\, dv = 2 \int_0^r I(x,y,z)\, dv \tag{4.13}$$

where the left-hand side integrates over the whole diffracted volume; the right hand side either over the half of the volume from sample surface to the centroid, or from the

centroid position to the tip of the gauge volume; L is the distance from the tip of gauge volume to sample surface; and r is the distance from the sample surface to the diffraction centroid.
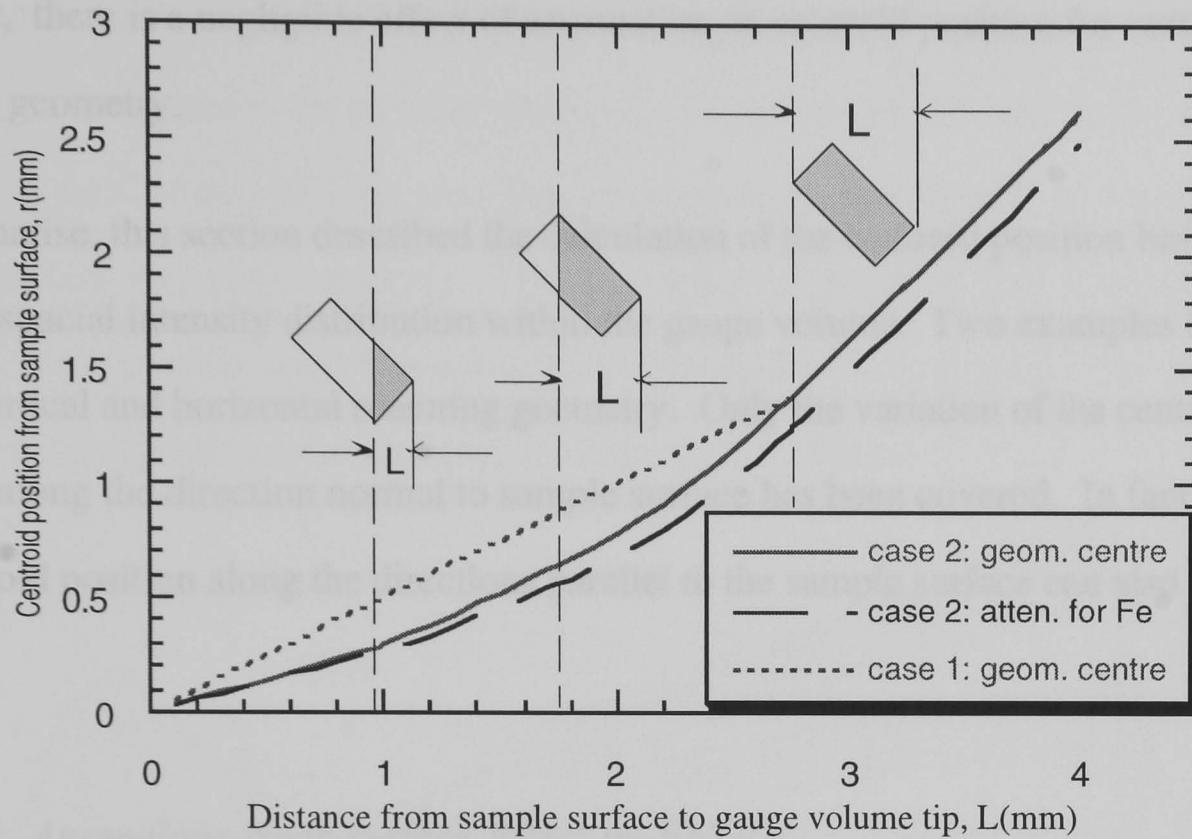
Figure 4.7 Centroid position relative to L, the distance from sample surface to gauge volume tip. The dotted line represents the vertical scanning geometry in figure 4.1(a), The solid and dashed lines represent the horizontal scanning geometry in figure 4.1(b) for iron, without and with attenuation, respectively.

If a gauge volume having the typical shape shown in figure 4.1(b) is considered, assuming that the spatial distributions of the detected intensity in the three orthogonal directions are three square pulses and the specimen possesses homogeneous diffraction properties, then the position of the geometrical centroid can be calculated as described in Appendix 3. Of course, the centroid position will also be affected by the distribution of the diffracted intensity within the gauge volume, which is associated with sample attenuation and the spatial intensity distribution of the incident beam. For the case of iron, even when the gauge volume is completely immersed in the sample, the difference of the centroid position is 0.13 mm for a 1.4x2.5x2.5 mm^3 gauge volume in the horizontal geometry. The result of these calculations is plotted in figure 4.7. The solid line represents the situation shown in figure 4.1(b), the dotted line represents the case shown in figure 4.1(a) with a square-pulse intensity distribution, and the dashed line

represents the case which is described in figure 4.1(b) after the attenuation is taken into account. It can be seen from figure 4.7 that the geometrical centroid position is closer to the sample surface for vertical scanning geometry, than for horizontal scanning geometry. However, there is a negligible effect of attenuation on centroid position for vertical scanning geometry.

To summarise, this section described the calculation of the centroid position based on the detected spacial intensity distribution within the gauge volume. Two examples have been given: vertical and horizontal scanning geometry. Only the variation of the centroid position along the direction normal to sample surface has been covered. In fact, shifts of the centroid position along the directions parallel to the sample surface can also occur.

4.2.3 Anomalous Near-surface Effect on ENGIN

A near-surface effect occurs when the gauge volume straddles the sample surface or an internal interface between two phases, or where the distribution of the phase being measured is not homogeneously distributed within the gauge volume. This occurs in single detector systems [Bourke 1990] as well as in the multi-detector system at ISIS. The effect results from a bias of the average diffraction length and volume for each individual detector [Harris 1995] as shown in figure 4.8. This causes an apparent peak shift in the spectrum in each detector, and hence pseudo-strain. Generally, the differences of gauge volume size and shape, as well as of the attenuation between the standard run for creating focusing routines and runs for measurements, can result in pseudo-strain. On ENGIN, it is more difficult to quantitatively model the effect due to a more complicated geometry: the radial collimator possesses 40 vanes and there are three banks of 45 detectors behind it [Wright 1994]. Nevertheless, a set of experiments with a powder specimen were carried out on ENGIN to evaluate the effect and to validate the simulation of Monte Carlo method [Harris 1995].

It is necessary to use both vertical and horizontal geometry for three-dimension strain measurements. However, there should be no surface effect for vertical scanning as the three banks of detectors are equivalent to each other when the gauge volume enters the sample along the z-direction. Powder specimen were used in both cases as no type I strain and texture exist in the powder specimen. Two types of powder, iron and aluminium (particle size: 60μm), were put into containers consisting of an aluminium frame with two vanadium windows. The two vanadium windows (0.1 mm thick) act as surfaces for the powder specimen due to its unique diffraction property. The first set-up of geometry is the horizontal scanning as shown in figure 4.9.
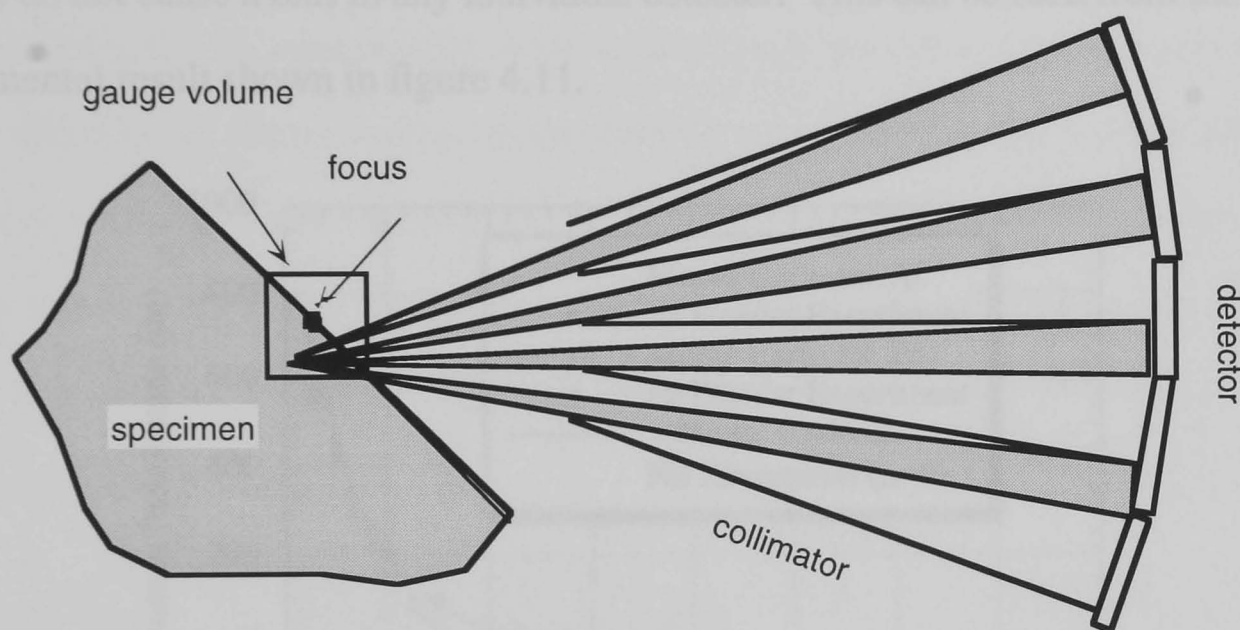
Figure 4.8 Changes in average diffraction length and volume for individual detectors on ENGIN.

The results for the case shown in figure 4.9 using iron and aluminium powders are shown in figure 4.10. The calculation of centroid position was obtained by applying the principle described in chapter 4.2.2. It can be seen that a similar near-surface pseudo-strain distribution was found in iron and aluminium powders, although the attenuation coefficient
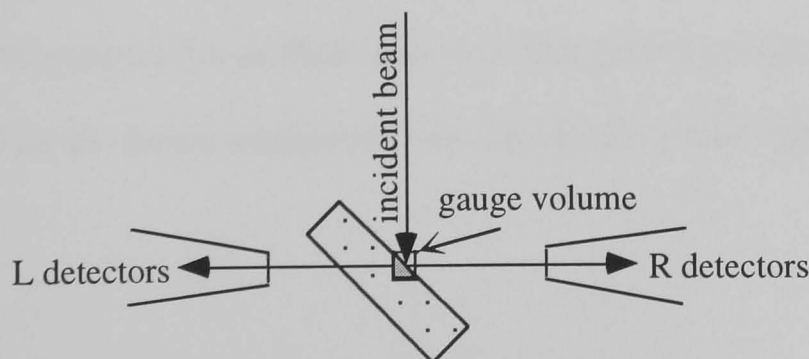
Figure 4.9 Horizontal scanning set-up

of iron is nine times larger than that of aluminium. The more the gauge volume travels out of the sample, the larger the pseudo-strain. The largest pseudo-strain occurs at 0.17 mm from the sample surface: it is 600 $\mu\varepsilon$ for the iron powder specimen. Monte Carlo simulation for the case of figure 4.9 agrees well with the powder experiment, as shown in figure 4.10.

The second experimental geometry is the vertical scanning as shown in figure 4.1(a). In this case no pseudo-strain occurs when the gauge volume scans through the sample surface, because the flight length of neutrons from different areas and the diffraction volume do not cause a bias in any individual detector. This can be seen from the experimental result shown in figure 4.11.
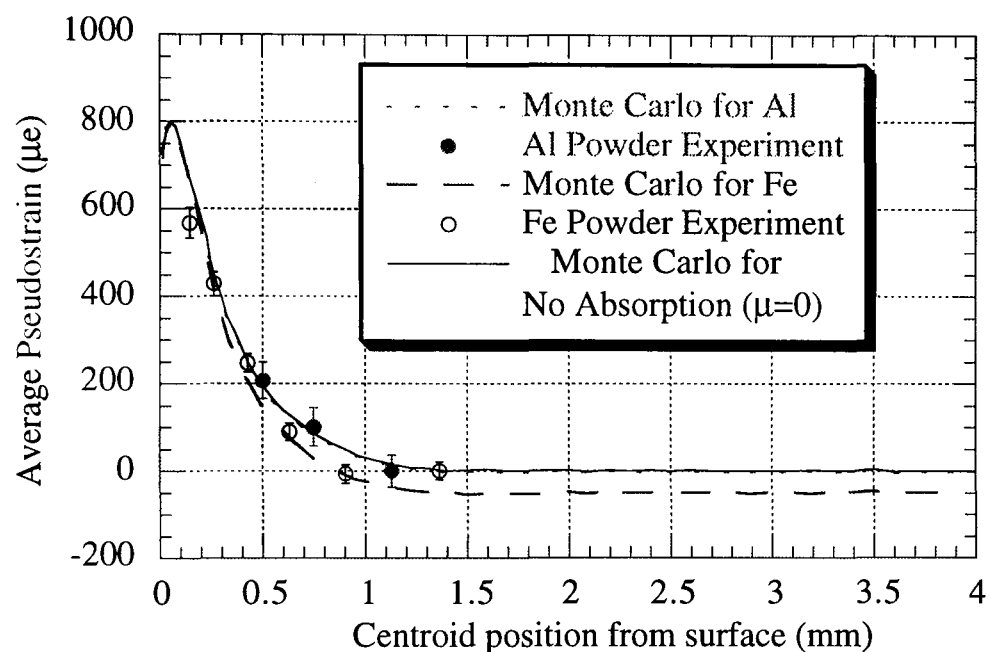
Figure 4.10 Comparison of pseudo-strains measured in iron and aluminium powders and stimulated using Monte Carlo method for the right-hand scanning set-up and the right-hand detectors.

To correct the pseudo-strain effect for horizontal near-surface scanning, except Monte Carlo simulation and powder scanning, one also can compare the strains measured in the same direction in both geometries as there are two orthogonal groups of detectors on ENGIN which allow us to obtain strains in four directions in two subsequent measurements.
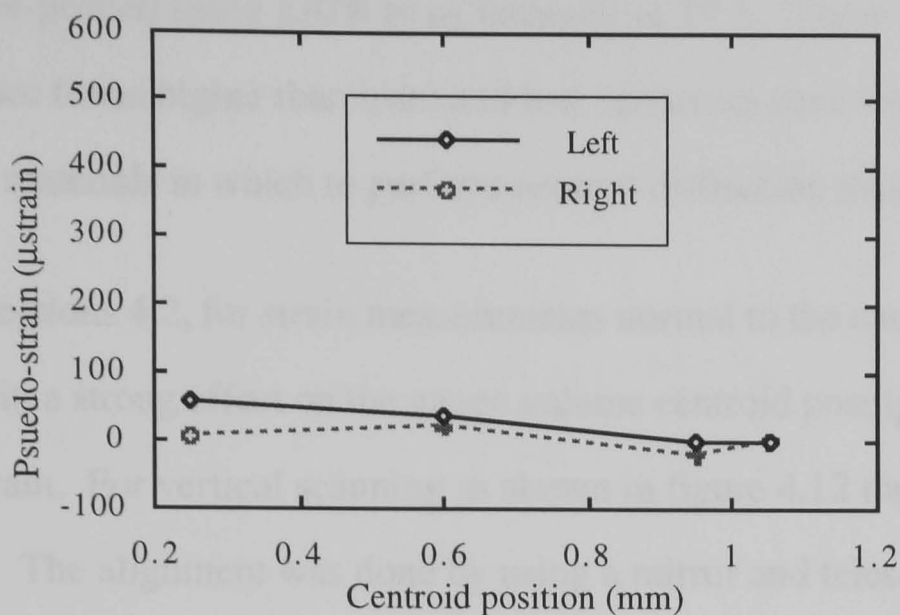
Figure 4.11 Surface effect for vertical scanning geometry.

As a summary, for the near-surface strain measurement normal to a sample surface, the surface effect of the measurement system must be taken into account. For a multi-detector system with radial collimators like ENGIN, it is essential to characterise the geometry and to correct the anomalous effect to achieve high performance (less than 50 $\mu\varepsilon$) on near-surface strain measurements, particularly for horizontal scanning.
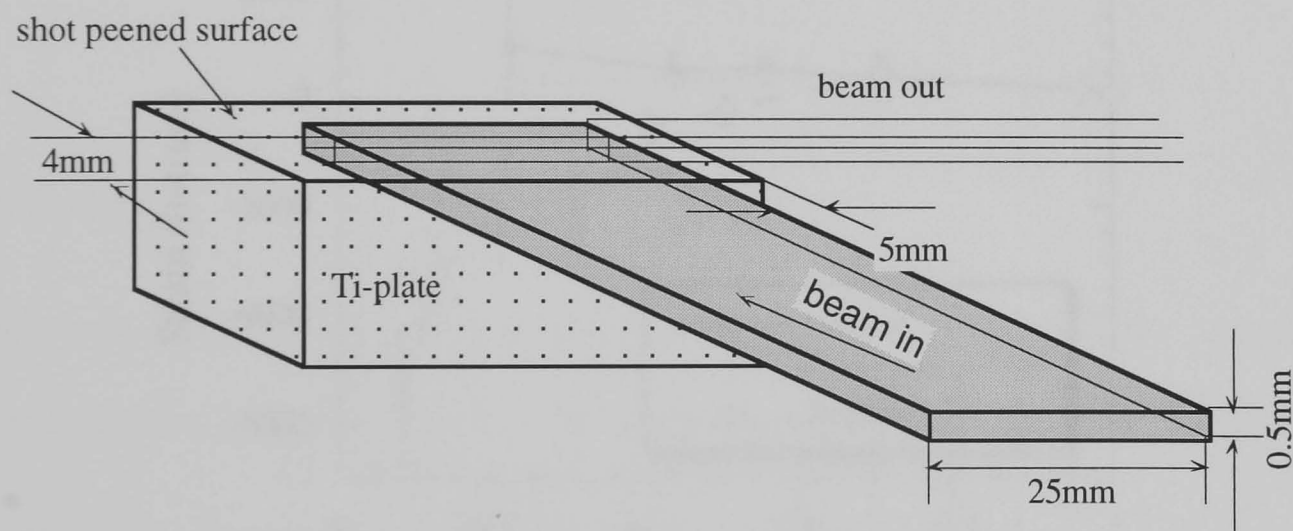
Figure 4.12 Dimensions of gauge volume and measurement position

4.3 Example — Near-Surface Stresses in A Shot - Peened Titanium Alloy

To illustrate the methodology outlined above the residual strain was determined in a shot peened titanium alloy surface. Shot peening is a method of producing compressive residual strain (stress) in the surface region of components to improve their resistance to fatigue. The α-β alloy IMI-318 (Ti-6Al-4V) finds many applications in gas turbine engines. The specimen was an IMI 318 alloy plate with dimensions of $23 \times 20 \times 50 \, mm^3$.

62

Its surface was shot-peened using 230 R to an intensity of 20 A. These alloys possess high absorption (two times higher than iron) and low scattering (one fourth of iron), hence are difficult materials in which to perform neutron diffraction strain measurement.

As mentioned in sections 4.2, for strain measurements normal to the sample surface high absorption results in a strong effect on the gauge volume centroid position and on the surface pseudo-strain. For vertical scanning as shown in figure 4.12 the gauge volume is $1.4x25x0.5$ mm^3. The alignment was done by using a mirror and telescope to confirm that the slit is parallel to the shot-peened surface. Figure 4.13 shows the strain distributions near the shot-peened surface in the directions normal and parallel to the surface. It also shows the correction for the strain normal to the surface using the methodology developed in section 4.2. Only the in-plane stress employing vertical geometry has been calculated since the in-plane stresses dominate the resistance to fatigue, and is shown in figure 4.14.
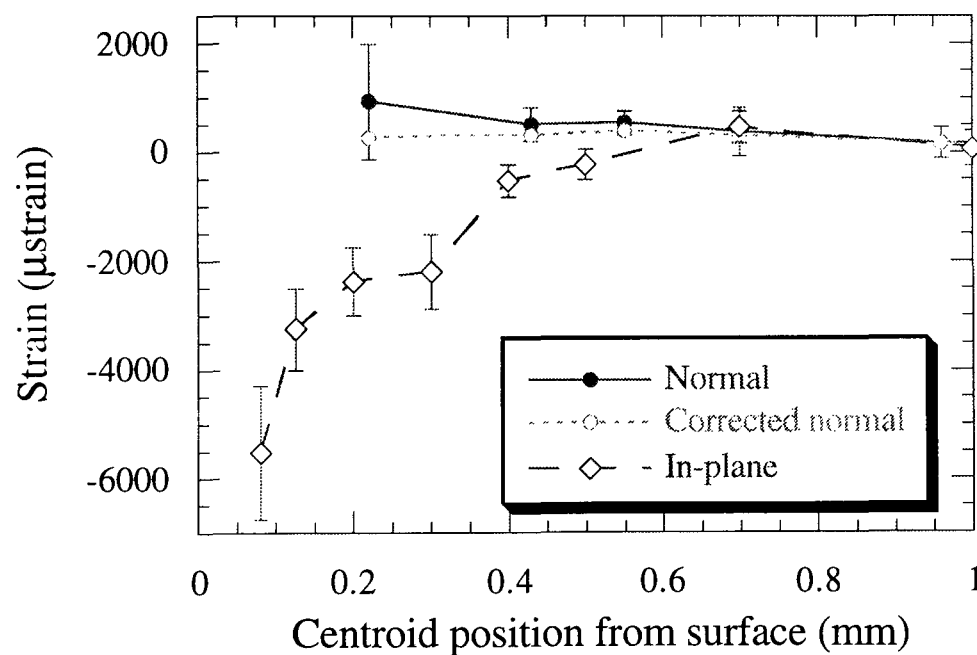
Fig. 4.13 Strain distribution near the shot-peened surface and the correction for the strains normal to the surface.

The strain-free data was obtained at a point 2 mm from the shot-peened surface assuming that there is no effect of shot-peening. The in-plane stress is mainly compressive, with a peak tensile stress of 100 MPa at 0.7 mm, and becomes zero at about 0.6 mm from surface. At 0.08 mm from surface the stress is most compressive, −800 MPa. The stress measured by neutron and X-ray diffraction is comparable bearing in mind that the neutron
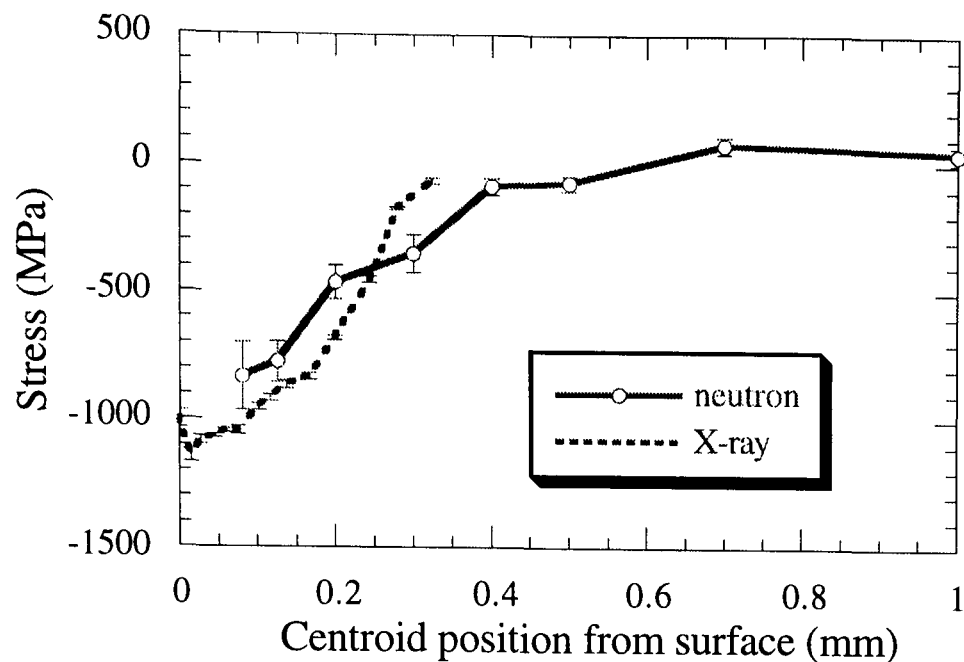
Fig.4.14 In-plane stress distribution near the shot-peened surface. Comparison of Neutron and X-ray diffraction measurements. The X-ray measurement was made by Collin Small of Rolls Royce plc.

measurement is averaging over a larger gauge volume and over all reflections of the material, whereas the X-ray measurement is derived from only one reflection, $(21\bar{3}3)$ with much smaller gauge volume.

4.5 Summary

The strain measurement near surfaces by neutron diffraction requires the measurement position to be precisely determined. These can be achieved by

• an intensity calculation and data fitting from a rapid scan

• a modelling calculation of centroid position based on gauge volume size and attenuation

Furthermore, the pseudo-strain from the surface effect needs to be corrected using results from either a powder scan or a Monte Carlo simulation. In addition it is also possible to make a correction by comparing strain measurements for the same direction and positions in both geometrical set-ups. In this case more attention has to be paid to the error caused by gauge volume averaging.

The set-up of the vertical geometry in fig.4.1(a) where one of the gauge volume surfaces is parallel to the sample surface, has a small systematic error than that of horizontal geometry, where the gauge volume enters the sample from one of its edges. However, strain measurement must be normally carried out using both geometries if one wants to obtain the strains in three principle directions. A 0.1 mm position precision and high strain precision can be achieved after all the correction techniques are applied. This makes the neutron diffraction technique become a complement of X-rays for strain measurement near a surface, and can uniquely measure the strain from 0.1 mm below sample surface.

CHAPTER 5: 3-D RESIDUAL STRESS DISTRIBUTION SURROUNDING A COLD-EXPANDED HOLE IN A HIGH STRENGTH ALUMINIUM PLATE

5.1 Introduction

Rising demand for longer lives in both civil and military aerospace is likely to ensure that the economical lives of some aircraft structures will be dictated by their long-term fatigue performances. Generally, the primary source of fatigue damage (cracking) is at mechanical joints, and the problem becomes more important as the demand for minimum structural weight to improved aircraft performance increases. Mechanical joining methods are commonly used in aircraft structures. The transfer of loads from one structural assemble to another is accomplished either through the joining bolts in shear, or by friction at the contacting surfaces by means of fastener clamping. So, particularly at high shear load transfer joints, where thin or thick components are jointed, fastener holes can become the major source of fatigue cracking [Mann 1983 and Schwarmann 1982].

Cold expansion techniques have been used for over thirty years to produce fatigue life enhancement and have been reviewed by Champoux [1986]. Superposition of the residual stresses near the hole with service loads leads to improvements in fatigue life either by delaying or suppressing crack initiation, or more often by reducing fatigue crack growth rates. Expansion is achieved using prescribed levels of mandrel interference. The optimum degree of mandrel interference for a particular application will, however, depend on the local geometry of the component; and fatigue life predictions of structures containing such expanded holes rely critically on estimates of the residual stress distribution surrounding the hole. Increasing importance is being given to the three

dimensionality of the residual stress distribution produced by split sleeve expansion. It has been suggested from fractographic evidence that the residual stress distribution varies across the thickness of the plate [Ozelton 1986 and Pell 1989]. In particular it has been suggested that a larger residual compressive hoop stress is generated at the mandrel outlet face of the plate than at the mandrel inlet face.

Neutron diffraction is a useful tool for non-destructive determination of the 3-D stress field deep in components. Instrument development and measurement technique improvement at ISIS have made these measurements feasible despite the need for great care in locating the measurement position (to an accuracy of 0.1 mm) and scanning for long time. Although the measurements of the 3D residual stress distribution at the hole have been made by a destructive method - a modified Sachs method [Ozdemir 1993]— this chapter will present measurements using neutron diffraction for comparison of these two methods.

5.2 Experimental Details

5.2.1 Precise Determination of Measurement Position

A more detailed description of the complete stress measurement of neutron diffraction is given in chapter 2 and chapter 5, but the basic experimental set-up is covered here as can be seen in figure 5.1. In order to obtain the highest precision, a number of careful measurements were carried out to precisely determine the position of the gauge volume with respect to the specimen surfaces. The full stress tensor approach used here also required measurements to be made accurately along the three principal axes which were known due to the symmetry of the hole expansion process.

To accurately measure the position of the gauge volume with respect to the component, fast surface scanning was used, subsequently fitting the data to a model describing the intensity variation as the gauge volume enters the material. This gave the gauge volume position to an accuracy of 0.1mm. The angular orientation of the sample was achieved by

placing the specimen at the centre of a prismatic orthogonal square frame, which was constructed so that the point equidistant from the two most orthogonal faces was known. Using a high accuracy metrology table, a known point on the specimen was located at this point before the frame was transported to the neutron source. This enabled measurements to be made along the principal directions to within 1°.
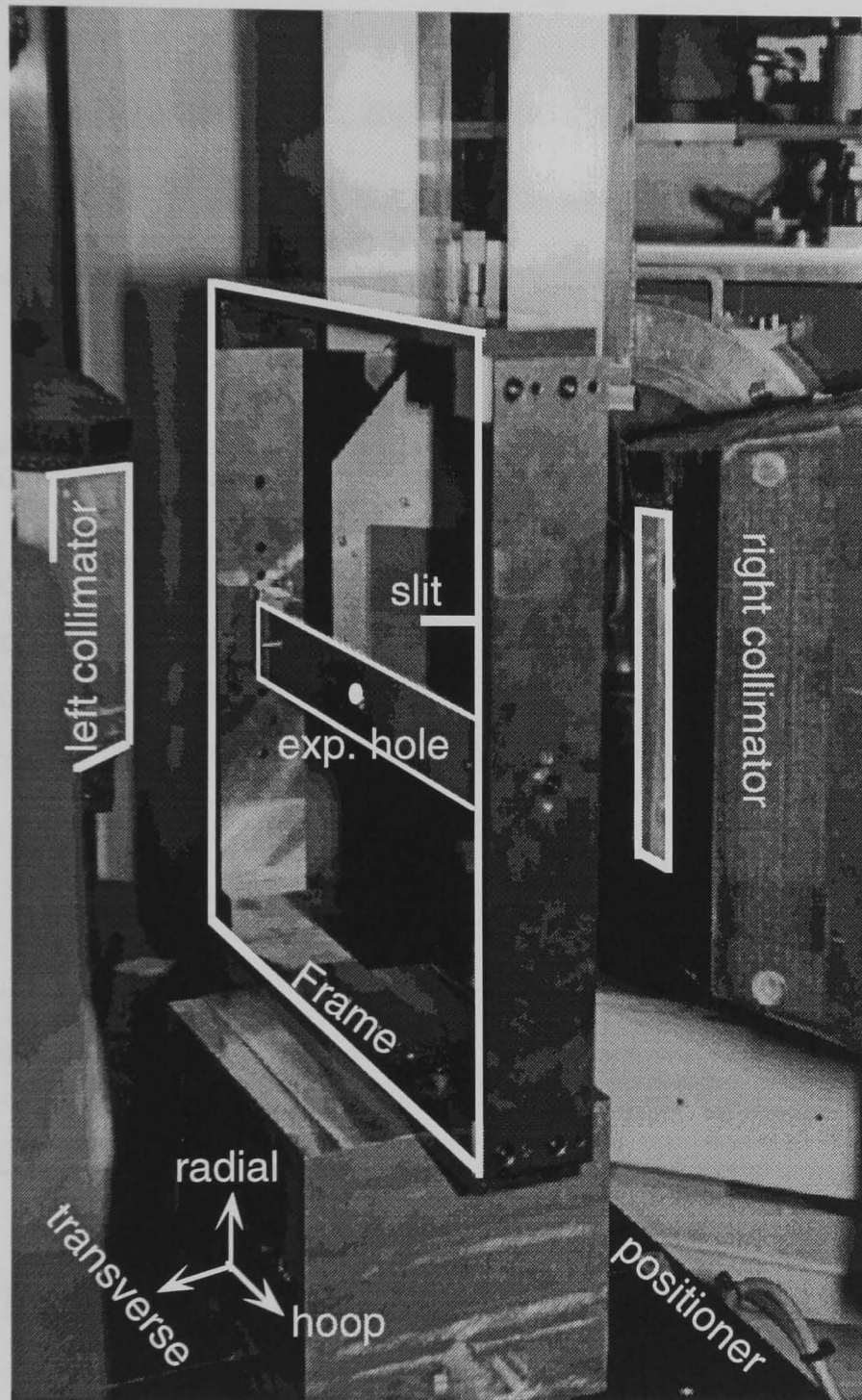
Figure 5.1 Experimental set-up for strain measurement surrounding a cold expanded hole on ENGIN

5.2.2 Stress Distribution Around the Cold-Expanded Hole

The dimensions of the component are shown in figure 5.2. A series of measurements of the hoop and transverse strains were made in the zx plane at the positions shown in figure 5.2. The frame and hence the specimen was then rotated by 90° and measurement of the

radial and transverse strains were made at the same positions in the zx plane of the component. The refinement of all the runs was carried out using a Pawley refinement method. Thus the residual strain distribution is represented by the lattice parameter strain, e.g. the strain calculated by

$$\varepsilon = \frac{\Delta a}{a_0} \qquad (5.1)$$

where Δa is the lattice parameter shift, and a_0 is the strain-free lattice parameter. Figure 5.3 shows the residual strain distribution along the mid-thickness of the plate ($x=2.5$ mm). The strain-free value, a_0, was obtained by measuring a point 100 mm away from the hole.
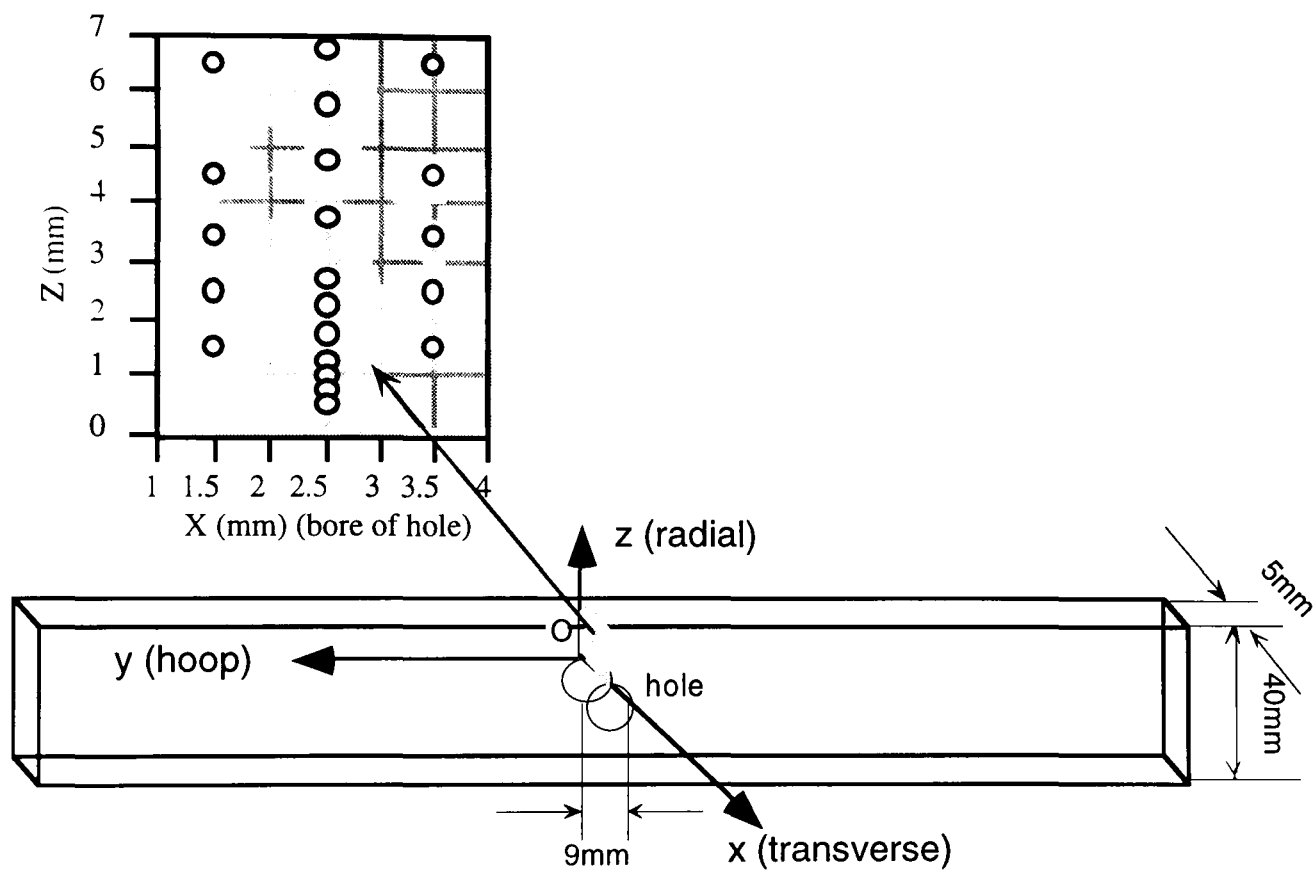
Figure 5.2 Dimensions of the cold expanded hole and measurement positions.

The stress distribution in isotropic polycrystalline materials is calculated from the measured strains by

$$\sigma_{ij} = \frac{E}{1+v}\, \varepsilon_{ij} + \frac{vE}{(1+v)(1-2v)}\, \delta_{ij}\varepsilon_{kk} \qquad (5.2)$$

where k is a dummy suffix summing over all k (e.g., $\varepsilon_{kk}=\varepsilon_{11} + \varepsilon_{22}+\varepsilon_{33}$); δ is Kronecker's delta function; E, the Youngs modulus; v, the Poissons ratio.
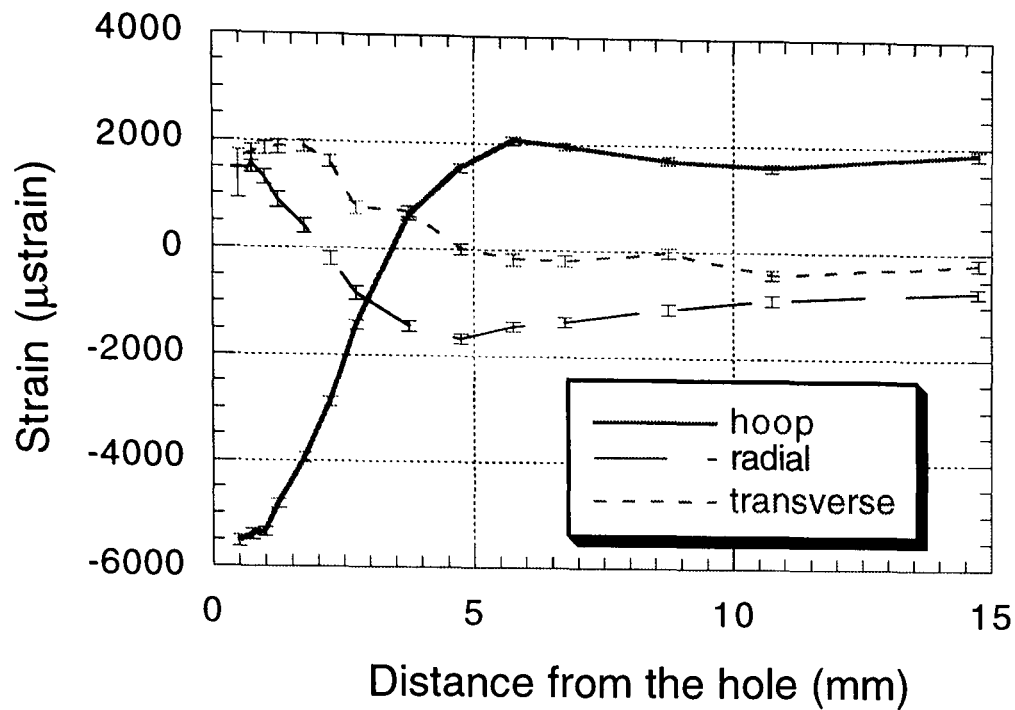
Figure 5.3 Strain distribution in the centre of the plane, as a function of position from the hole.

The residual stress distribution near the hole was calculated from the strain distribution measured by neutron diffraction, using equation (5.2), assuming that:

- the three measurement directions coincide with the principal axes of the component.

- the aluminium plate is an isotropic polycrystalline material.
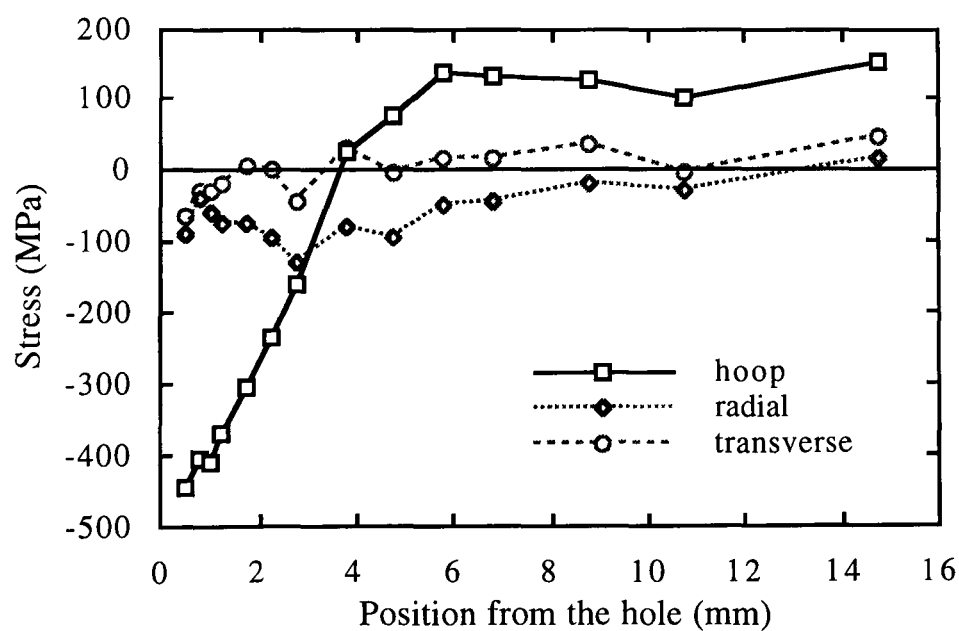
Figure 5.4 Stress distribution in the centre of the plane, as a function of position from the hole. The typical error is ±40 MPa.

It can be seen from figure 5.4 that the general shape of the residual stress distribution is as expected, and shows reasonable correlation with previously published estimates of the distribution obtained from destructive mechanical tests [Ozdemir 1993] except that there

70

was no evidence of stress relaxation near the hole. The accuracy of these measurements is dependent on how well we can control or compensate for systematic errors. These are the errors which will make the experimental results differ from the "true" values. The peak positions and hence the lattice parameters, may be affected by a greater or lesser degree by type I, II and III residual stresses, prior plastic deformation and instrument effects (chapters 4 and 5). The following analysis will focus on the likely effects from instrumental errors and the use of a large gauge volume compared to the scale of the residual stress gradients.

5.3 Discussion

5.3.1 Correction for Surface Effect

A pseudo-strain can be measured when the gauge volume straddles the sample surface so that only part of the collimating detector sees all of the gauge volume (chapter 4). Additionally, a large systematic error can arise from insufficient measurement time, due to reduction of the diffraction volume near the surface (Appendix 4). For the case of the cold expanded hole in the aluminium plate, only the radial strain measurement was affected as the other strains were measured by scanning the gauge volume vertically through the component surface. For this case an empirical instrumental correction was achieved based on the knowledge that the radial stress should become zero as the surface is approached. Inspection of the radial stress as it approaches the surface of the hole in figure 5.4 shows that there is clearly an error, as it deviates sharply from zero just where we expect the surface effect to become significant. Thus the radial strains in this area were linearly extrapolated so as to produce a zero radial stress. The subsequent corrected results of the residual stress distribution along the mid-thickness line is shown in figure 5.5. Although the residual stress distribution is substantially unchanged there is now some evidence of stress relaxation near the hole. Based on these corrected results, and in combination with surface residual stress measurements made by X-ray diffraction a 3D hoop residual stress map may be constructed using the principal of minimum curvature.

This is plotted in figure 5.6. It can be seen from figure 5.6 that there is a larger residual compressive hoop stress at the mandrel outlet face of the plate than at the mandrel inlet face.
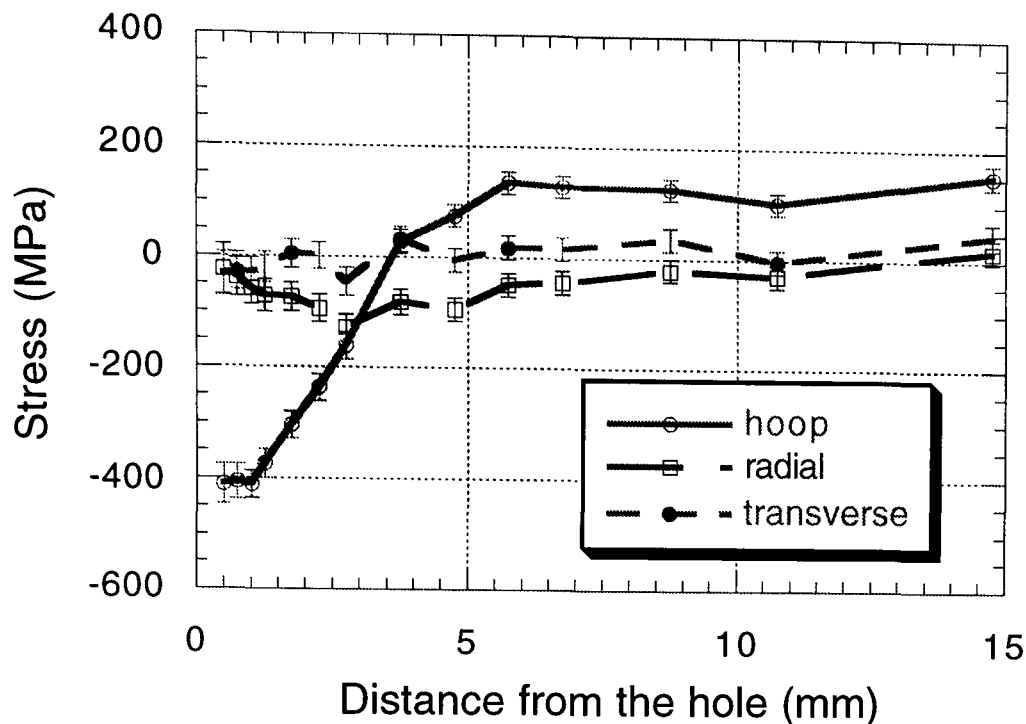
Figure 5.5 Stress distribution after correction, in the centre of the plane, as a function of position from the hole.

5.3.2 The Gradient Effect of Gauge Volume Averaging on Interpreting Strain

The measured strain distribution from neutron diffraction is likely to be markedly different from the real strain distribution in areas of rapidly changing strain gradients, due to the relatively large gauge volume used in neutron diffraction. This is why the evidence of relaxation at the hole edge seen in the neutron measurements (figure 5.6) is not as pronounced as in the mechanical measurements made using the modified Sachs technique (figure 5.7).

Unfortunately it is not feasible to convert the 'averaged' neutron strain measurements to a 'real' distribution, but an interesting comparison is to compare the neutron distribution to that produced by averaging the strain distribution measured by Sachs measurement over a similar measurement volume size i.e. 2.5 mm. Such a Sachs "average" and the neutron strain data for the middle plane position (x=2.5) are plotted in figure 5.8. The neutron diffraction can not show substantial strain relaxation unless a deconvolution algorithm can
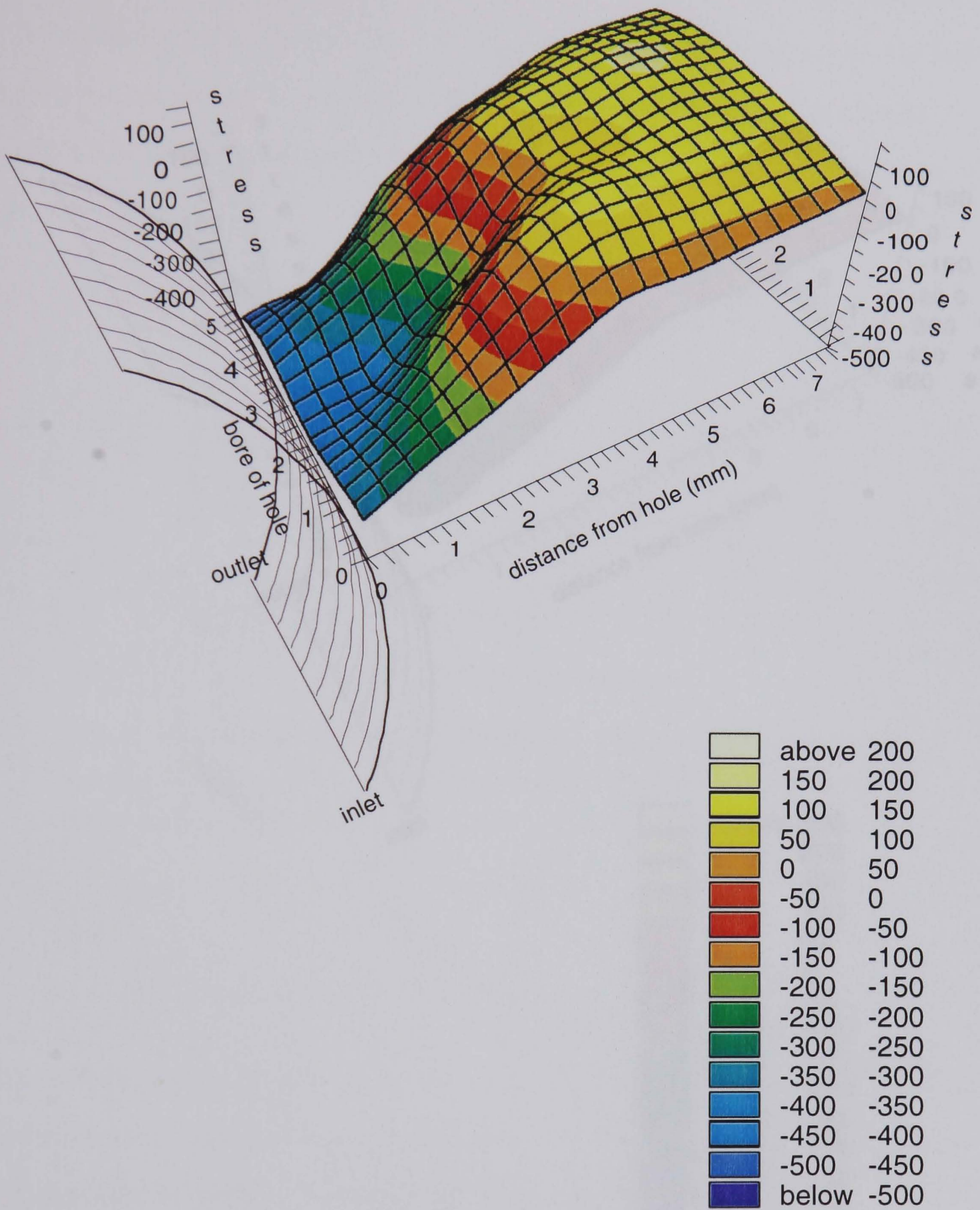
Figure 5.6 Hoop stress distribution near the hole measured by neutron diffraction (stress unit: MPa).
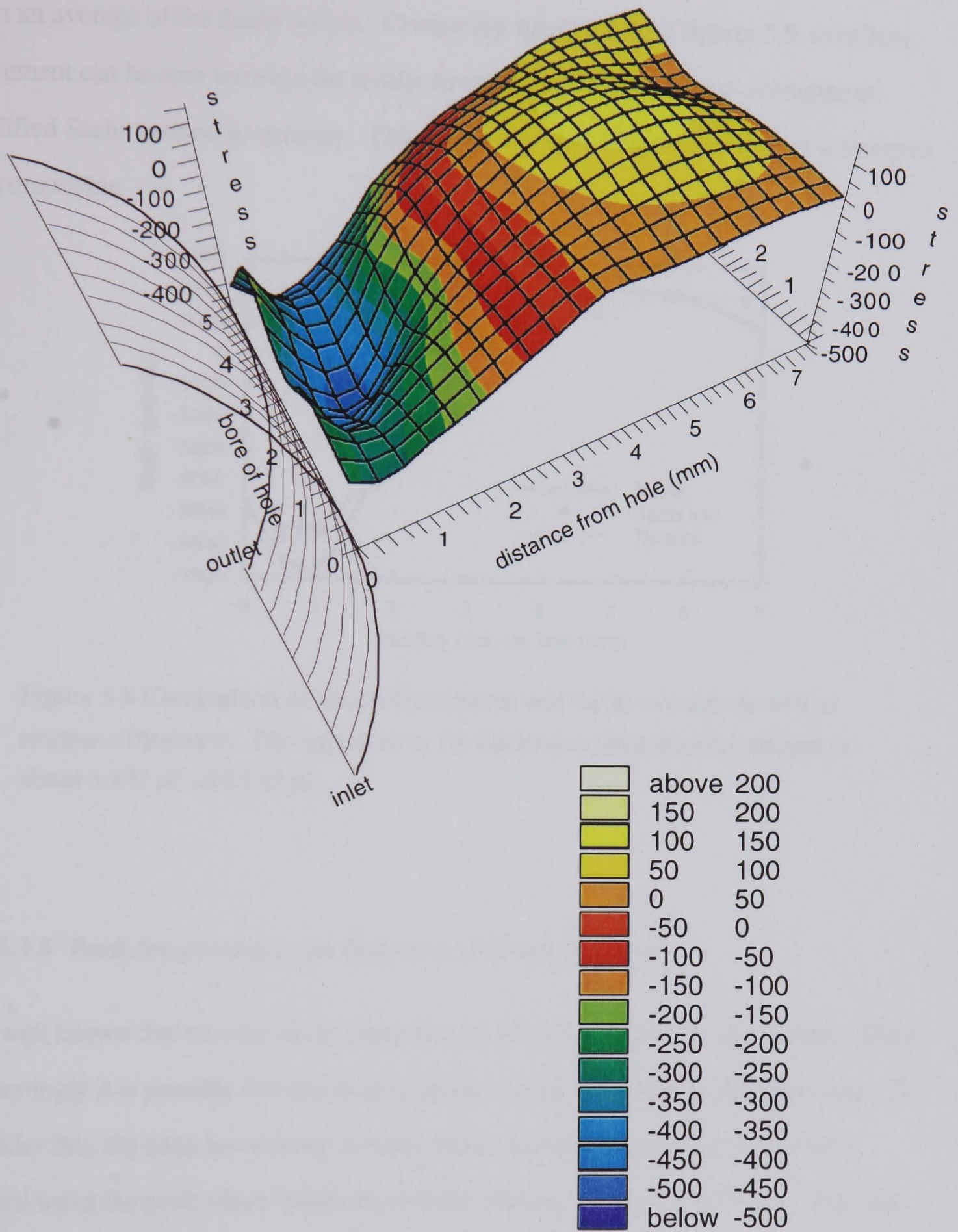
Figure 5.7 Hoop stress distribution near the hole measured by modified Sachs method. (stress unit: MPa)

above	200
150	200
100	150
50	100
0	50
-50	0
-100	-50
-150	-100
-200	-150
-250	-200
-300	-250
-350	-300
-400	-350
-450	-400
-500	-450
below	-500

be developed. A similar effect is found on the 3-D residual stress distribution around the hole as can be seen from figure 5.9, which shows a 3-D plot of the stresses calculated from an average of the Sachs values. Comparing figure 5.6 with figures 5.9, excellent agreement can be seen between the results from neutron diffraction and averaging of modified Sachs method in quantity. This shows that both stress measurement techniques are compatible.
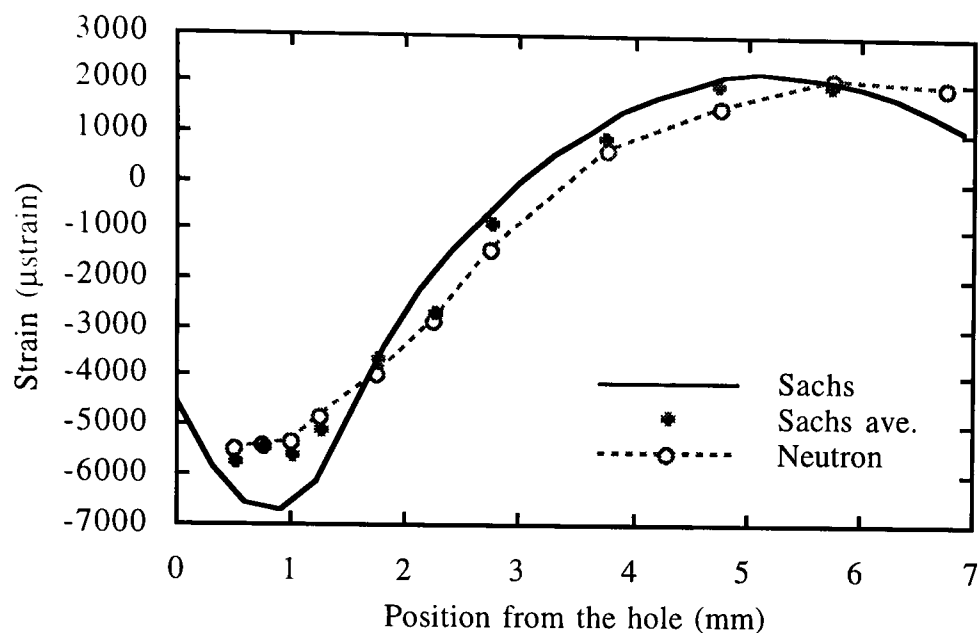
Figure 5.8 Comparison of strains from Sachs and Sachs average as well as neutron diffraction. The typical error for Sachs and neutron measurement is about ± 100 $\mu\varepsilon$ and ± 50 $\mu\varepsilon$.

5.3.3 Peak Broadening as an Indicator of Strain Gradient

It is well known that microstrain in materials can affect the diffraction peak width. More interestingly it is possible that macrostrain gradient also may cause peak broadening. To consider this, the peak broadening in recent strain measurements analysis has been studied using the peak-shape functions with the Pawley refinement software. The peak shape depends on several physical factors, notably the pulse shape, moderator physics, instrumental resolution and sample effects. A reasonable approximation to the powder diffraction peak shape has been found to be [Ikeda 1985] (* represents convolution):

$$P(t) = \frac{t^2}{2\tau_f^3}\exp\left(\frac{-t}{\tau_f}\right) * \left\{(1-R)d(t) + R\left(\frac{1}{\tau_s}\right)\exp\left(\frac{-t}{\tau_s}\right)\right\} * \frac{1}{\Sigma\sqrt{2\pi}}\exp\left(\frac{-x^2}{2\Sigma^2}\right) \qquad (5.3)$$
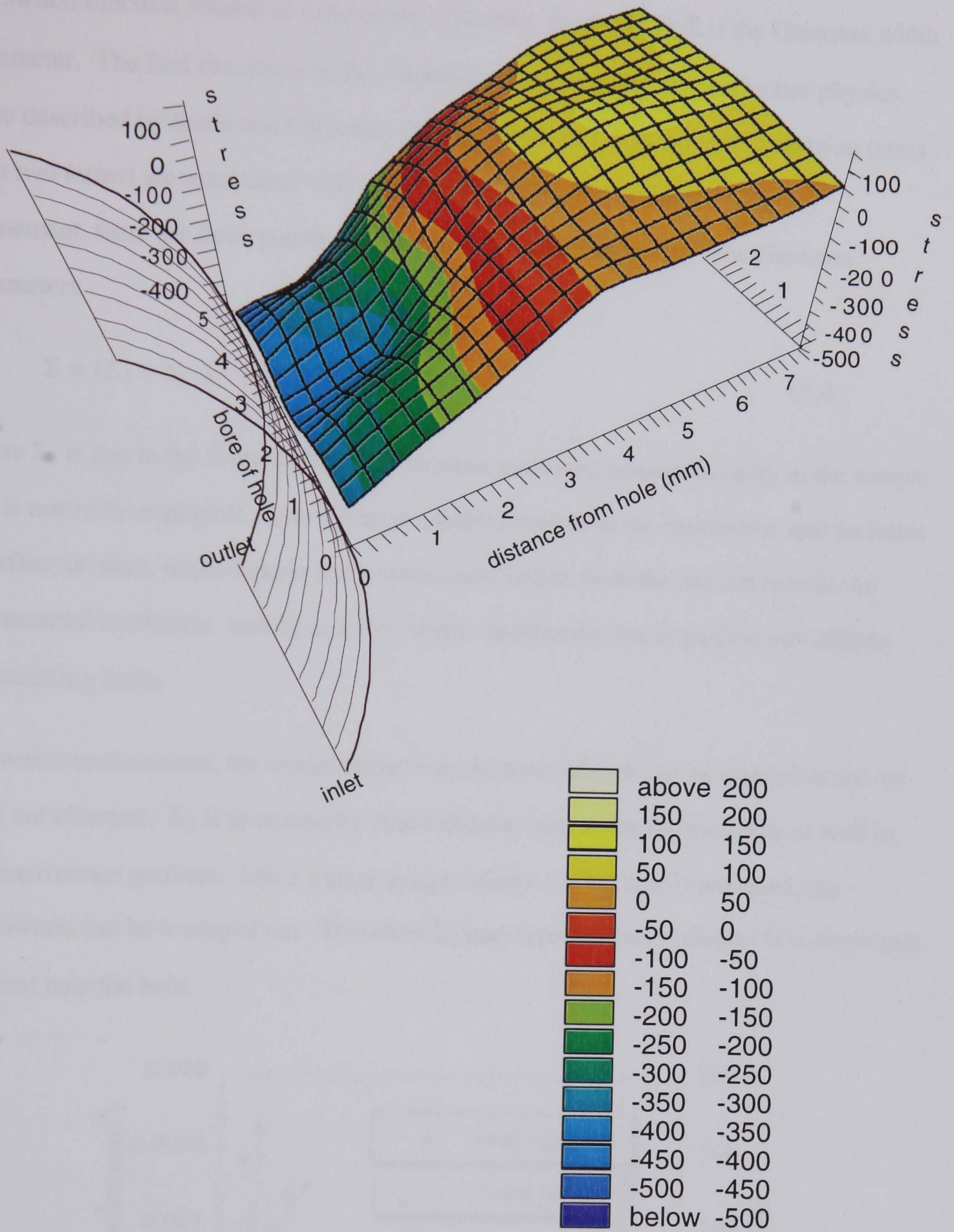
Figure 5.9 Hoop stress distribution near the hole measured by the modified Sachs method, after averaging over the gauge volume used in neutron diffraction. (stress unit: MPa)

where t is time of flight; τ_f is the fast decay constant, τ_s is the slow decay constant; R is the switch function, related to a Boltzmann function, $\exp(-E/E_0)$; Σ is the Gaussian width parameter. The first two terms in this expression, representing the moderator physics, were described by Ikeda and Carpenter [1985]. Both the Gaussian and Lorentzian terms (last two terms) are associated with instrumental and sample effects. In Pawley refinement, there are three parameters to describe peak broadening. The Gaussian parameters

$$\Sigma = (\Sigma_1 + \Sigma_2 \lambda^2 + \Sigma_3 \lambda^4)^{1/2} \qquad (5.4)$$

where Σ_1 is due to the finite width of the neutron pulse and paracrystallinity in the sample and is normally negligible, Σ_2 is the most significant term in the expression, and includes the effect of strain in the sample and a small contribution from the $\Delta\theta\cot\theta$ term in the instrumental resolution, and Σ_3 is a very small contribution due to particle size effects and stacking faults.

For strain measurement, the contribution from the term $\Delta\theta\cot\theta$ can be ignored as the set-up is not changed. Σ_2 is governed by strain effects, such as the microstrains as well as the macrostrain gradient. Since a large gauge volume ($2\times2\times2$ mm^3) was used, the microstrain can be averaged out. Therefore Σ_2 may represent the variation of macrostrain gradient near the hole.
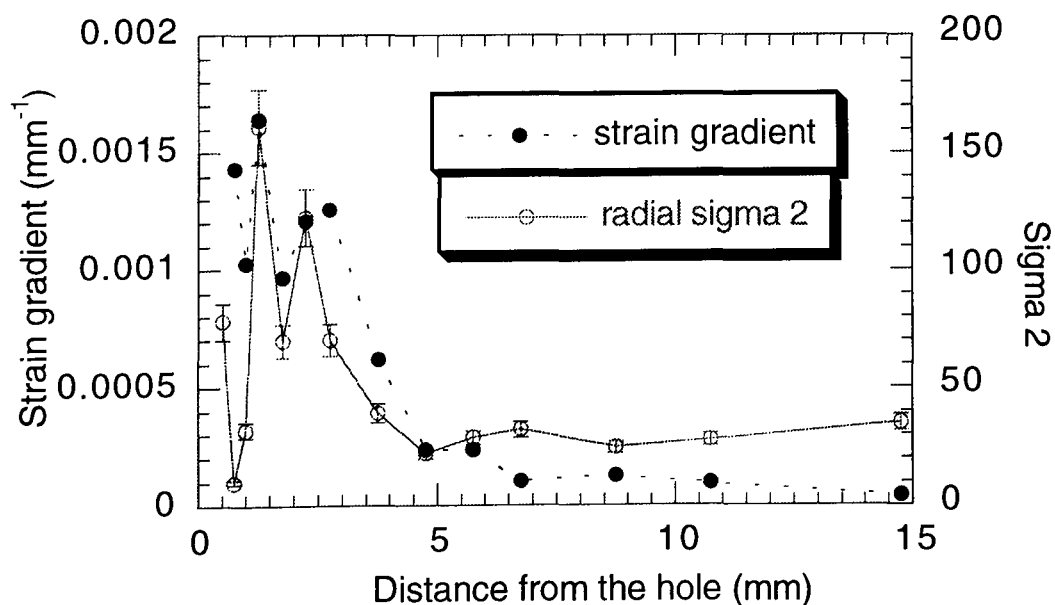
Fig. 5.10 Correspondence between sigma 2 and the macrostrain gradient.

To test this hypothesis the macrostrain gradient is plotted alongside the Σ_2 in figure 5.10. The Σ_2 reflects the trend in the macrostrain gradient well. This suggests that peak width may be used to provide extra information about the strain gradient distribution within a component, and may deserve further study into its possible use to aid deconvolution of strain data 'averaged' by the use of relatively large gauge volumes.

5.4 Summary

- A 3-D stress measurement has been made using neutron diffraction at a 4% expanded hole in a high strength aluminium alloy.

- Differences in residual compressive hoop stress distribution were detected through the thickness of the specimen, with hoop stresses being smaller at the 'inlet' side of the hole, (where the mandrel first engages), when compared to the 'outlet' side. This results is similar to that obtained using mechanical measurement.

- The correlation between the measurements from neutron diffraction and the modified Sachs method is good, providing that the gauge volume averaging effect in neutron diffraction is taken into account. This indicates that the lattice parameter strain in aluminium from neutron diffraction measurement represents the bulk property of the material.

- The variation of peak width can be used as an indicator of the variation of type I strain gradients in materials.

CHAPTER 6: MEASUREMENT OF RESIDUAL AND AT-LOAD STRAINS IN A MULTI-FASTENER LAP SPLICE JOINT

6.1 Introduction

As a significant proportion of the global aircraft fleet approach their original design lives there has been increasing activity developing and implementing fatigue and fracture damage tolerance concepts into ageing, current and next generation aircraft. Of particular interest is the development of methodologies for handling widespread fatigue damage (WFD) in geriatric aircraft. In a metallic airframe a typical form of WFD would be a large number of small fatigue cracks where each is not critical by itself but whose combined effect may seriously damage the load bearing capacity of the structure.

Widespread fatigue damage is seen at riveted lap splice joints usually in the form of multiple cracks emanating from fastener holes. To reliably predict crack growth rates and fracture strengths of lap splice joints accurate stress and fracture analyses are needed [Tan 1993] particularly for critical joints which typically use both of the most commonly used fatigue life enhancement methods: hole cold expansion and interference fit fasteners. This is best attacked by a number of parallel techniques the foremost of which is the acquisition of fatigue data from laboratory joints which accurately represent the aircraft joint under consideration particularly with respect to secondary bending and load transfer. Secondary bending are those which occur in a joint, when axial loads are applied, due to asymmetry of the structure. The load transfer is the amount of load which is transferred between the joined elements by a given fastener row — throughout an aircraft a wide variety of load transfer and secondary bending combinations occur. Analysis is

particularly difficult as the joints are complicated structural assemblies, the full stress analysis of which requires consideration of the contact stresses, in-plane geometry, bolt clearance, bolt friction, and relative motion and different load ratio between the loading bolts. In addition, even if the plates are assumed to respond linear elastically, the problem is non-linear due to the change in contact area with change in load [Naik 1991]. To complement these analytical solutions limited experimental measurements have been made on the joint surfaces [Cook 1994] by the use of instrumented fasteners [Sawyer 1994] but no previous measurements have been made of the residual and applied strains within a joint.

Neutron strain scanning uniquely allows measurement of the stain distribution within a joint and the aim of the experiment was to scan both the residual and at-load strain distributions in a multi-fastener double splice lap joint.

6.2 Experimental Details

6.2.1 Description of the Joint

The joint was developed at DRA Farnborough as a laboratory joint on which a fastener evaluation programme could be carried out to give realistic assessments of fastener performance in situations where significant secondary bending was present. The joint is shown in figure 6.1, consisting of the two 5 mm thick plates, with a bending restraint provided by the 3 mm thick plate. A double shear connection is termed the controlling section (passive fastener) as the side plate attached at this connection controls the degree of bending in the joint. Failure at the controlling section was observed in a small number of early fatigue tests and it was decided that in order to avoid further failures, the controlling section should have the fastener holes cold expanded and interference fit fasteners installed [Cook 1994]. The standard joint therefore has fixed fastener conditions at the controlling section and variable fastener conditions at the test section appropriate to the test requirements. It is important to know what effect the fastener

conditions in the test section have on the load transfer and secondary bending characteristics of the joint as they may significantly affect the fatigue endurance due to different load transfer and secondary bending conditions must be separated from changes
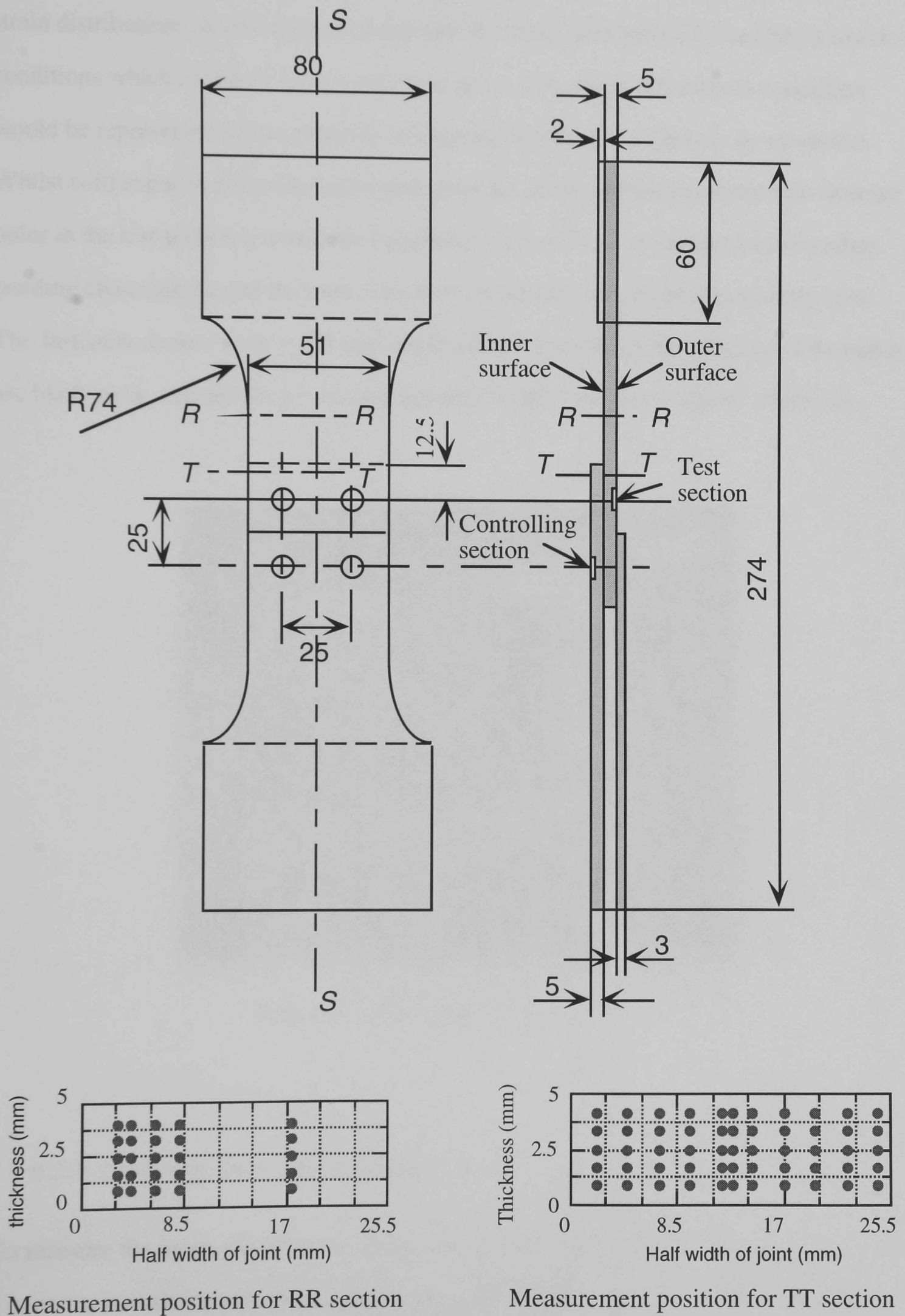
Figure 6.1 Size of the joint

in endurance due to the qualities of the different fastening systems. The object of this measurement is to investigate the load transfer and secondary bending characteristics of the joint by examination of the strain distribution present. Since the joint may be assembled with a variety of fastener conditions in the test section, which will affect the strain distributions, it was decided to examine the strain distribution in the joint at extreme conditions which are likely to be used in practice. It was argued that these conditions would be represented by the extremes in fastener fits which are likely to be examined. Whilst cold expansion would significantly alter the strain distribution around the fastener holes in the test section it would not significantly affect the load transfer and secondary bending characteristics of the joint, which are of primary concern in this investigation. The fasteners chosen were ≈ 100 µm interference, representing the extremes of fit which are likely to be selected for a 6.35 mm diameter fastener in typical aircraft structures.
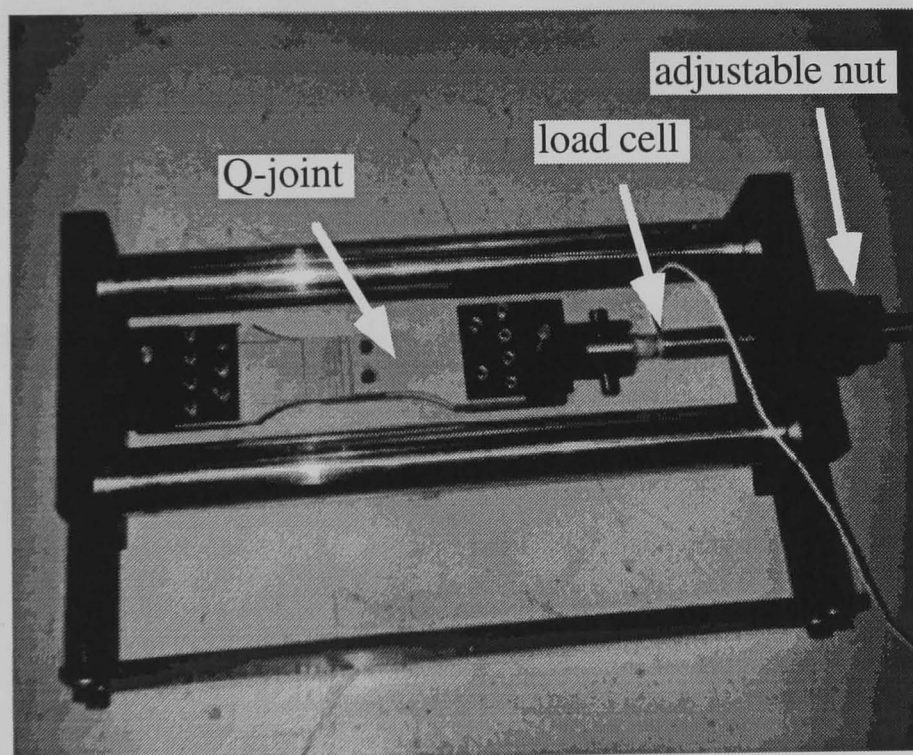
Figure 6.2 The Q-joint in the stress rig.

6.2.2 Stress Rig Description and Operation

To measure the strain distributions in the multi-fastener double splice lap joint under load, a compact uniaxial tensile stress rig was used (figure 6.2). The rig allowed unobstructed diffraction measurements through the joint and was accommodated on the positioner of

ENGIN. The specimen was attached to the rig using two plates extending to a loose fastener joint and it was precisely aligned so that torsion was avoided. The force was monitored with a load cell. The stress level was controlled by screwing the nut at the end of the rig. The orientation for measurement of strain parallel to the applied load is shown in figure 6.3. Figure 6.4 shows the measurements of strain in the same direction but without load.
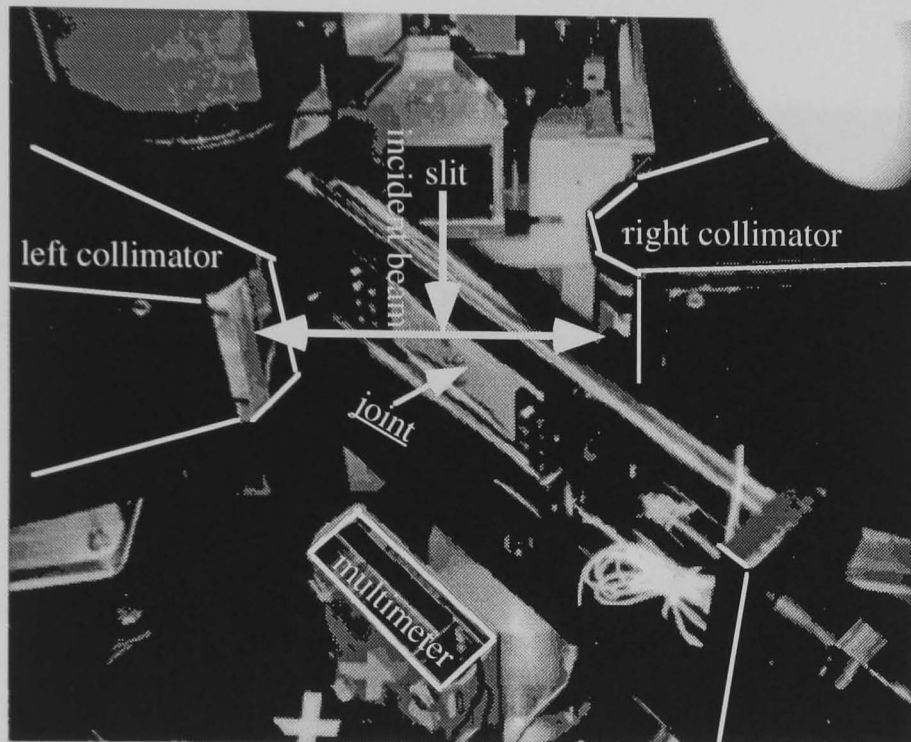
Figure 6.3 Set-up for strain measurement parallel to the load in the joint.

The joint was subjected to stress of 30 kN and held at constant stress to permit diffraction measurements on RR and TT sections in the test plate of the joint as shown in figure 6.1. Since the joint is symmetric to the $S–S$ axis, the strain distribution should be also symmetric to this axis so that measurements were only needed in half of the joint. Tensile and compression are indicated by positive and negative strain values respectively. Changes in lattice strain are expressed as $\mu\varepsilon$.

6.3 Results and Discussions

Measurements were made on the ENGIN diffractometer using a gauge volume of $1.4 \times 1 \times 3$ mm^3 for the TT section, which is a section tangential to the active fastener holes as shown in figure 6.1. For the RR section, a gauge volume of $1.4 \times 1 \times 5$ mm^3 was used. Strains were calculated from lattice parameters derived from the whole diffraction pattern

using Pawley refinement. d_0 was obtained from measurements in the test plate a long way from any mechanically induced residual stress distribution. The strain distribution for the RR and TT sections in the unloaded condition (figure 6.4) obtained from fitting a surface of minimum curvature through the data is given in figure 6.5 (a) and 6.6 (a). The joint was then mounted within a specially-designed loading rig (figure 6.3) and subjected to 30 kN tensile load along its axis. The strain distribution in the section RR and TT under load are then given in figure 6.5 (b) and 6.6 (b).
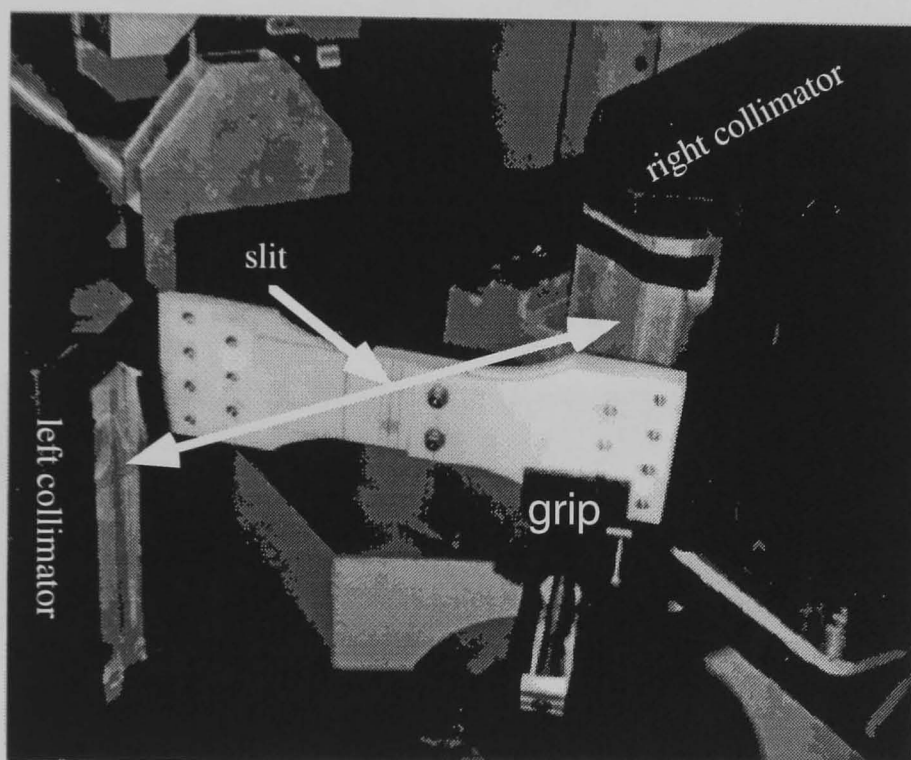
Figure 6.4 Set-up for strain measurement in the joint at zero load

Comparison of figure 6.6 (a) and (b) shows that loading has produced a substantial strain gradient on the TT section with a ≈1000 µε across the bulk of the joint. Due to the plastic deformation which occurs around interference fit fasteners and the preload applied to the fastener, there are residual strains present in the joint prior to external loading (figure 6.6 (a)). The pattern of strain distribution under 30kN load in the section is similar to that derived from finite element analysis [Cook 1994]. However, the strain gradient in the area immediately adjacent to the fastener is lower (≈500 µε) and it should be noted that this area is still in compression despite the 30kN tensile load, which is just below the load required to initiate yielding in the joint. This provides a confirmation of the excellence of the joint design as the fastener system has completely shielded the fastener hole from deleterious tensile strains under operational loading. Under these circumstance the critical fatigue location move away from the fasteners to an adjacent part of the structure.

(a) Strain on RR Section at Zero Load
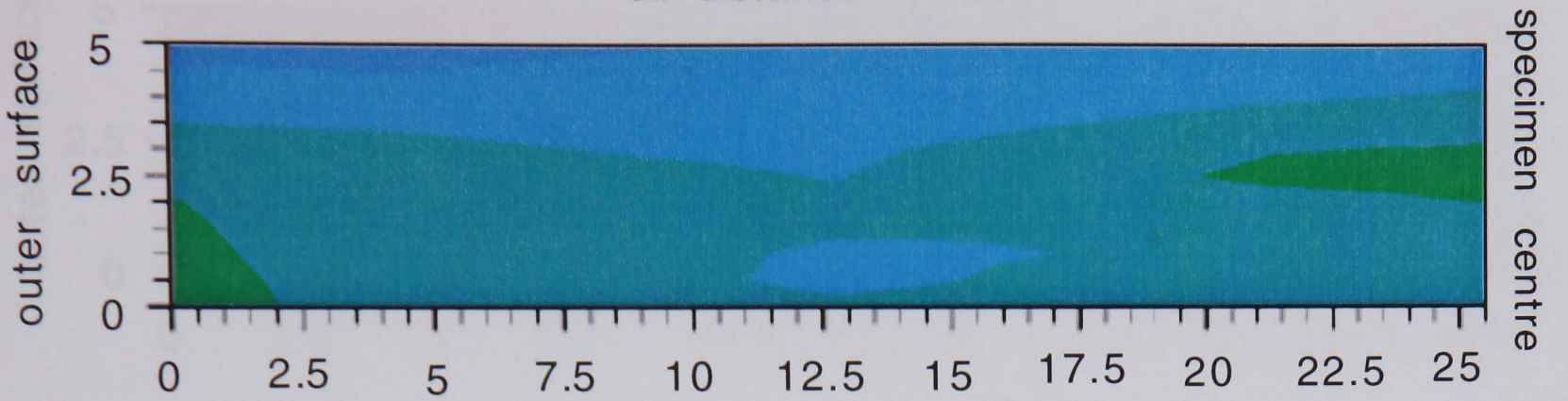
all distance in mm

(b) Strain on RR Section at 30 kN Load

all distance in mm

	(a)			(b)	
	above	1600		above	2800
	1400	1600		2600	2800
	1200	1400		2400	2600
	1000	1200		2200	2400
	800	1000		2000	2200
	600	800		1800	2000
	400	600		1600	1800
	200	400		1400	1600
	0	200		1200	1400
	-200	0		1000	1200
	-400	-200		800	1000
	below	-400		below	800
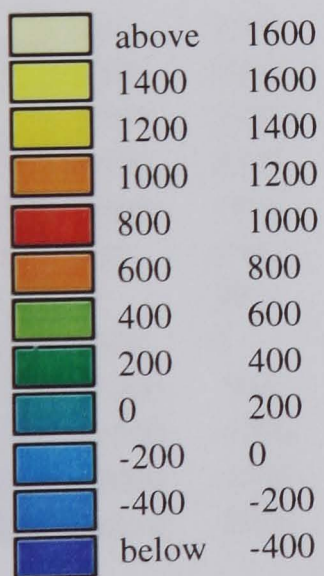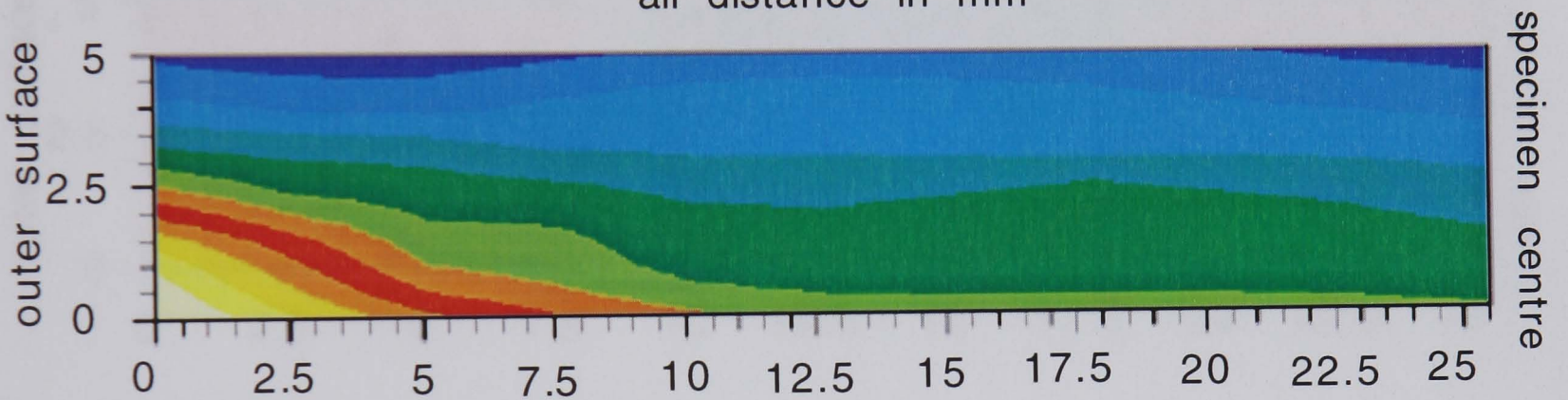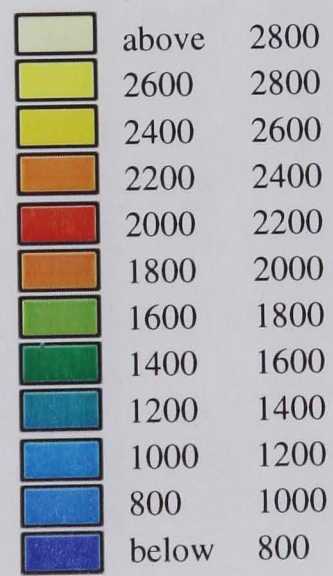
Figure 6.5 Strain distribution on RR section under zero (a) and 30 kN load (b). (strain unit: $\mu\varepsilon$)

(a) Strain on TT Section at Zero Load
all distance in mm
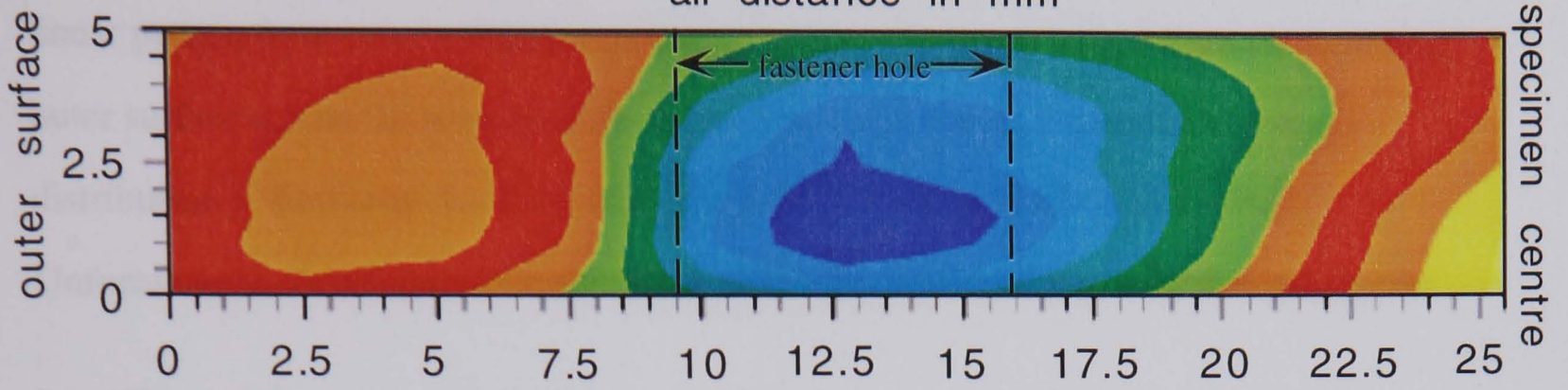
(b) Strain on TT Section at 30 kN Load
all distance in mm

above	3000
2500	3000
2000	2500
1500	2000
2000	1500
500	1000
0	500
-500	0
-1000	-500
-1500	-1000
-2000	-1500
below	-2000

(a)

above	4000
3500	4000
3000	3500
2500	3000
2000	2500
1500	2000
1000	1500
500	1000
0	500
-500	0
-1000	-500
below	-1000
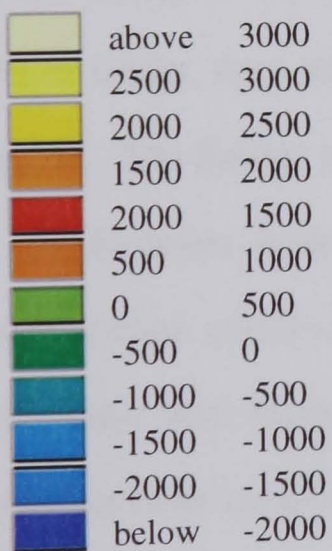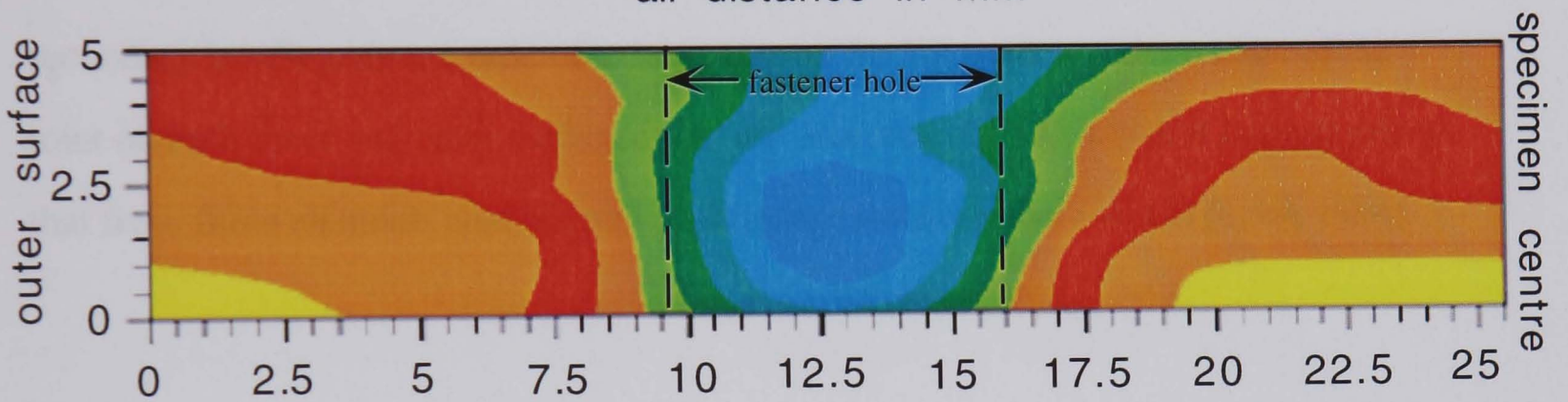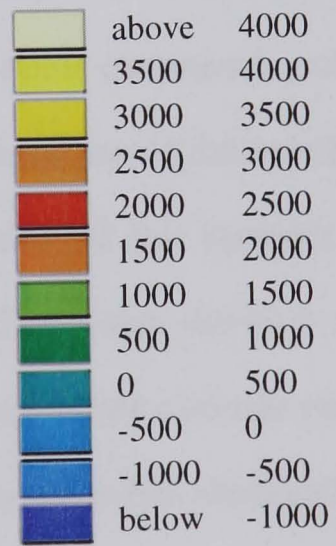
(b)

Figure 6.6 Strain distribution on TT section under zero load (a) and 30 kN load (b) (strain unit: $\mu\varepsilon$)

It was found that there is a small residual strain distribution in a random pattern on the RR section under zero load. After 30 kN tensile loading, the strain distribution presents a linear pattern from outer surface to specimen centre. There is a larger strain gradient near outer surface across the plate than that in the specimen centre. The pattern of strain distribution is similar to that obtained from finite element analysis [Cook 1994]. Unfortunately, the FE pattern could not be presented here as it is in a confidential report.

In addition to the axial strain in the section RR, there are secondary bending strains present due to the asymmetry of the joint. These are of particular importance, and have been measured by various techniques. It can be seen in figure 6.6 (b) that strains on both outer and inner faces of the specimen are different, from 800 $\mu\varepsilon$ to 2800 $\mu\varepsilon$. The secondary bending ratio, a ratio of axial strains on the RR section at the middle of the joint on both inner and outer surface of the test assemble, is 0.43 which is comparable to that from finite elements analysis and strain gauge measurement ($\approx$0.47) [Cook 1994].

6.4 Conclusions

Strain distributions on the TT section immediately adjacent to the fasteners and on a remote RR section under zero and 30 kN load have been measured using neutron diffraction technique. The former provides dramatic confirmation of the excellence of the joint design as the fastener system has completely shielded the fastener hole from deleterious tensile strains under operational loading. The latter shows a comparable secondary bending ratio with strain gauge measurement and finite element analysis. The strain distributions on both sections show similar pattern with that obtained from finite element analysis.

CHAPTER 7: CALIBRATION STRAIN MEASUREMENT FOR AN ENERGY-DISPERSIVE NEUTRON TRANSMISSION SPECTROMETER

7.1 Introduction

Conventional neutron strain measurements are achieved by recording a neutron diffraction pattern from a well-defined gauge volume but a relatively weak intensity is obtained in the detector. It has been suggested that neutron energy-dispersive transmission spectrometer possess both high resolution and intensity [Johnson 1981]. This technique uses a "white" incident beam and spectra are obtained by directly recording the total neutron cross section, e.g. the transmission beam. Obviously a pulse neutron source has an advantage to utilise the technique since the time-of-flight is available. As an elastic diffraction phenomenon, the scattering vector should be parallel to the neutron beam when the incident vector and diffracted vector parallel with each other as shown in figure 7.1. Thus the transmission spectra characterise the strains parallel to the neutron beam and the gauge volume is defined by the intersection of transmission beam and specimen.

Although application of the technique is sparse, an *in-situ* investigation of the austenite-bainite transformation in grey iron has been performed by measuring the height of Bragg edges in transmission spectra [Meggers 1994]. Strain measurement by the technique has been suggested by Johnson and Bowman for two-dimensional strain determination as in the transmission geometry information on scattering as a function of position in sample is easily preserved [Johnson 1981]. Priesmeyer has measured a shift of aluminium (200) edge up to 0.7×10^{-3} Å using this technique [Priesmeyer 1988]. However, as a new

strain measurement technique it is necessary to be calibrated. This chapter will present a theoretical analysis for this technique and a calibration strain measurement by comparing the strains measured by a transmission spectrometer and by strain gauges.
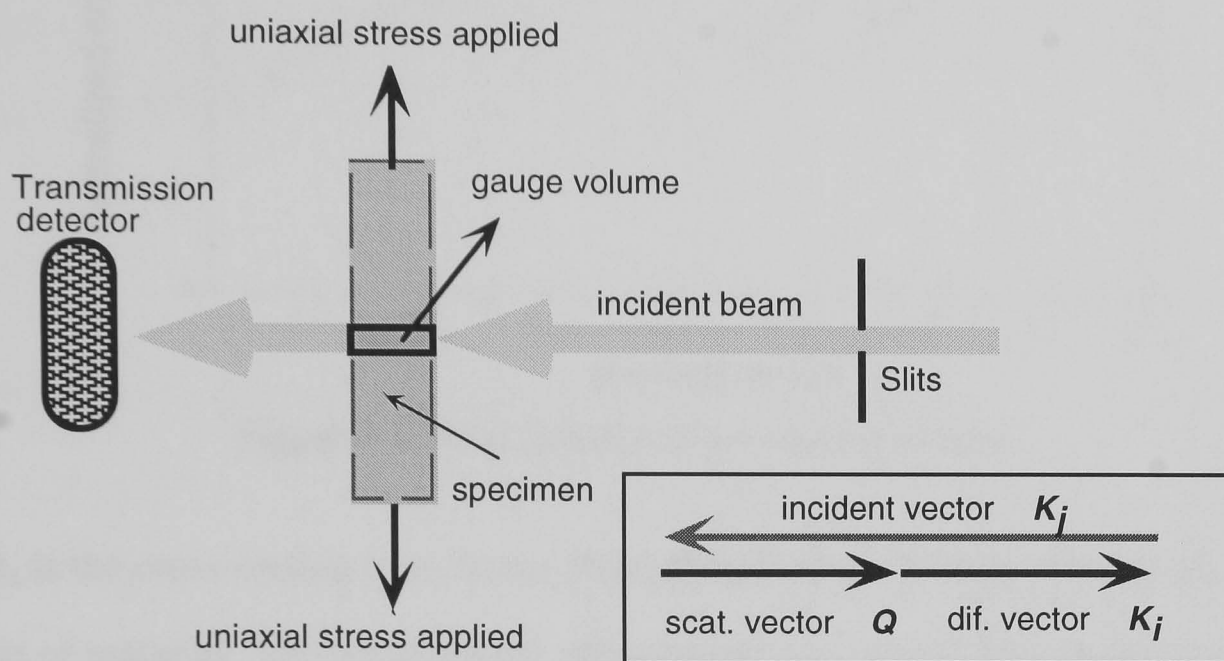
Fig. 7.1 Schematic drawing of the experiment.

7.2 Theory

The position of the Bragg edges of iron in a transmission spectrum can be calculated by its total coherent cross section (see Appendix 1):

$$\frac{N_c\lambda^2 b^2 a}{2} \sum_{\substack{hkl \\ d \geq \frac{\lambda}{2}}} \frac{[1+\cos(h+k+l)\pi]^2}{\sqrt{h^2 + k^2 + l^2}} \tag{7.1}$$

where the summation is over all planes (hkl) which are capable of giving Bragg reflections at a given neutron wavelength. N_c is the number of unit cells per unit volume. Taking the multiplicity of reflections into account in equation (7.1), one can obtain the total coherent cross section, β_c, normalised by its value at very short wavelengths, $4\pi b^2$ as shown in figure 7.2. The transmission intensity then can be obtained [Bacon 1975]:

$$I\ (L) = I_0 \exp\ (-\ (\beta_a + \beta_c)\ NL) \tag{7.2}$$
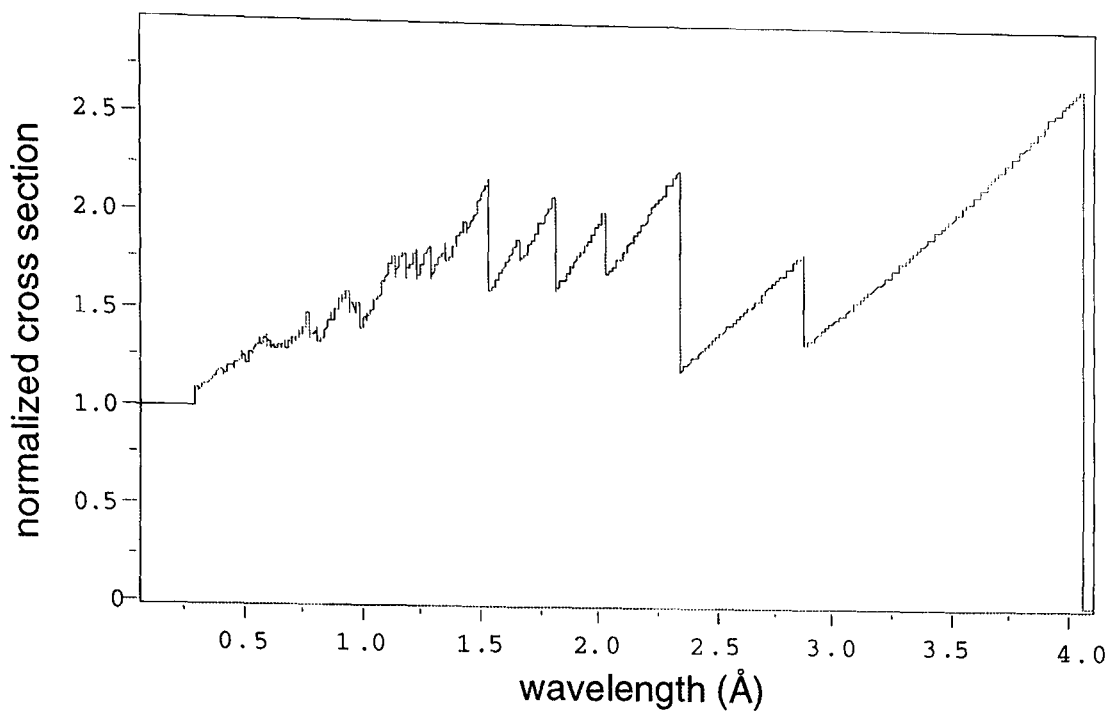
Figure 7.2 Total coherent cross section of iron

where β_a is the cross section from linear absorption; N is the density of material; L, the thickness of material. The transmission measurement is to record the spectrum with the sample of interest in the beam and again with sample removed. The transmission is then simply the ratio of the sample-in spectrum to the sample-out spectrum (both spectra have been normalized for length of run). If the sample has uniform thickness across the beam (a flat plate sample) then the transmission is:

$$T = \exp\ (-\ (\beta_a + \beta_c)\ NL) \tag{7.3}$$

Transmission spectra exhibit Bragg edges instead of Bragg peaks. These are steep decreases in the transmitted neutron intensity, due to the fact that the angular distribution of scattering from a certain lattice plane is limited by $\sin \theta = 1$: once backscattering is reached, the particular set of lattice planes will not contribute to coherent scattering. This results in a sudden decrease of the cross section and a change in transmission. From equation (7.1) and (7.2), one can see that the Bragg edges locate at:

$$\lambda_e = 2d_{hkl} \tag{7.4}$$

where d_{hkl} is the lattice plane spacing of the material. According to Bragg equation:

$$\lambda = 2d_{hkl} \sin \theta \tag{7.5}$$

90

when the diffraction angle $2\theta \leq 180°$, the plane with interplanar spacing d_{hkl} can participate in Bragg diffraction; thus the cut-off of the diffraction is at $\theta = 90°$, which is the backscattering, e.g. it is the inverse of a diffraction experiment.

The resolution of a transmission spectrometer is dominated by the moderator's time uncertainty [Windsor 1981] as the transmission Bragg edge corresponds to the inverse of backscattering and the resolution can be expressed as:

$$\frac{\Delta d}{d} = \frac{\Delta L}{L} \qquad (7.6)$$

where ΔL is the thickness of the moderator (28 mm at ISIS) and L is the distance between detector and moderator (16190 mm). Therefore the resolution of the transmission spectrometer on ENGIN is 1.7×10^{-3}, which is much better than that of the conventional diffraction geometry on ENGIN (5.6×10^{-3}) (chapter 3), even comparable to that of HRPD (2×10^{-3}).

7.3 Experimental Description

7.3.1 Stress Rigs and Samples

The experimental set-up is schematically shown in figure 7.1. The compact rigs permitted unobstructed transmission measurements through the samples and were accommodated on the positioner of ENGIN. The specimen used were medium carbon steel square bars. The compressive sample was a 10 mm wide and 25 mm long square bar except at the ends where there were two $25 \times 25 \times 10$ mm^3 plates attached to the rig (figure 7.3). The force was applied by screwing the two nuts. To avoid non-balance of the force, the strains were monitored by two strain gauges positioned on both sides of the sample. For the tensile sample, the sample was 6 mm wide and 80 mm long (figure 7.4). The force was monitored with a load cell and strains were measured by a strain gauge placed on the sample surface. The transmission spectrum was recorded by a detector with an effective area of 5×5 cm^2, giving about 10% efficiency, which was designed by

Dr N. Rhodes of ISIS. For the tensile experiment, the gauge volume was $6 \times 5 \times 5 mm^3$, and $10 \times 5 \times 5 mm^3$ for the compressive measurement.
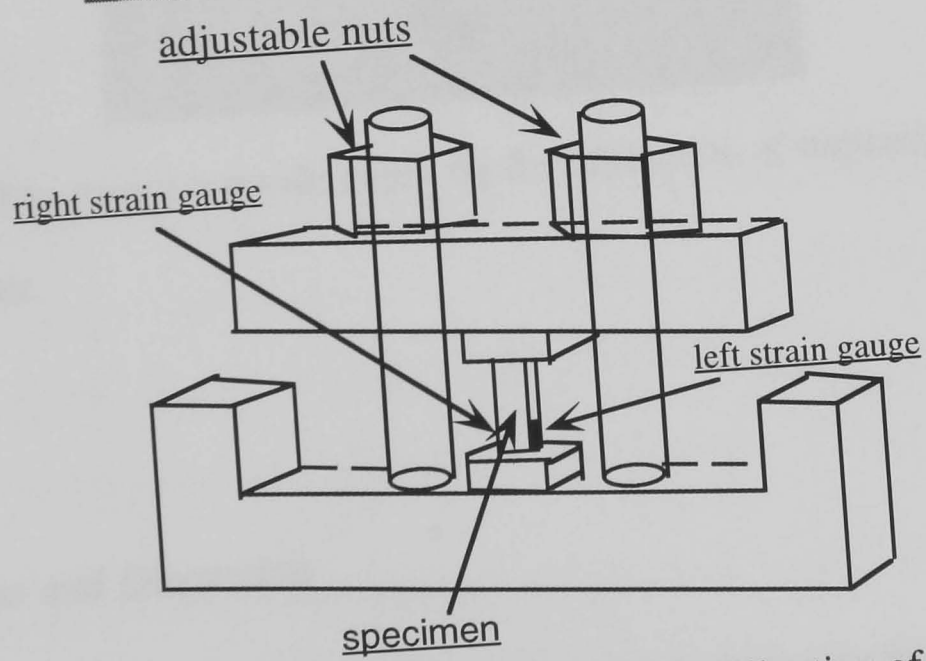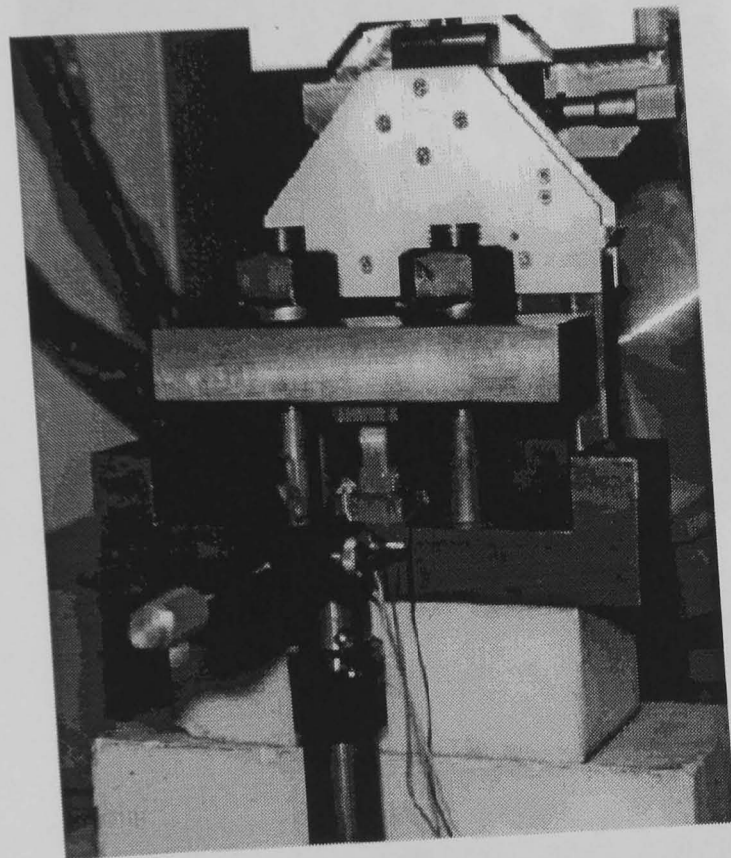
Figure 7.3 The compact compressive stress rig for calibration of transmission spectrometer.
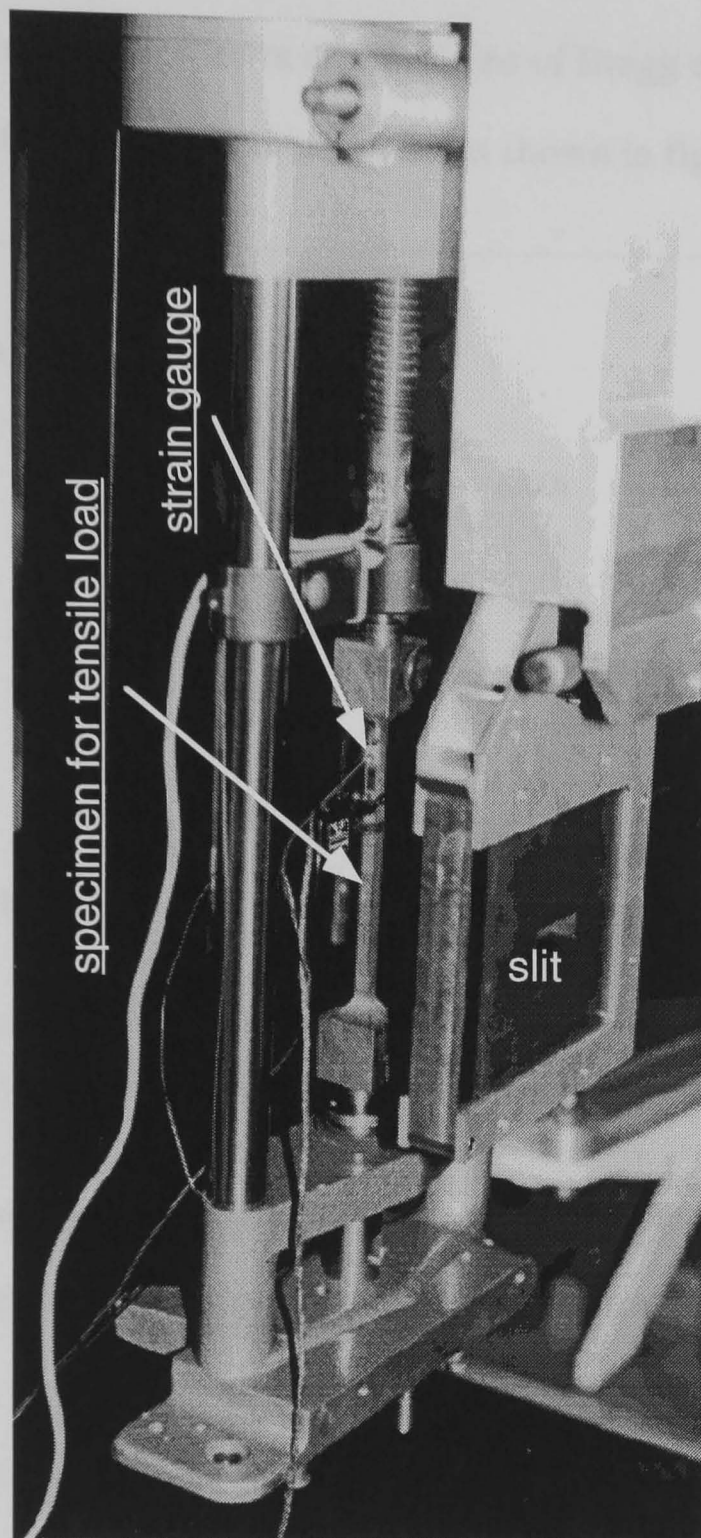
Figure 7.4 The compact tensile stress rig for calibration of transmission spectrometer.

7.3.2 Results and Discussion

Sequential loads were applied to the two bars. At each level the samples were held at constant stress to permit transmission measurement. The tensile macro-uniaxial strains recorded by the strain gauge were 0, 1000, and 1850 µε. In the case for 10 mm wide bar, the compressive macro-uniaxial strains measured by the strain gauge were 0, −1010

and −1840 με. The transmission spectra are consisted of Bragg edges and contain structure information of whole diffraction pattern as shown in figure 7.5.
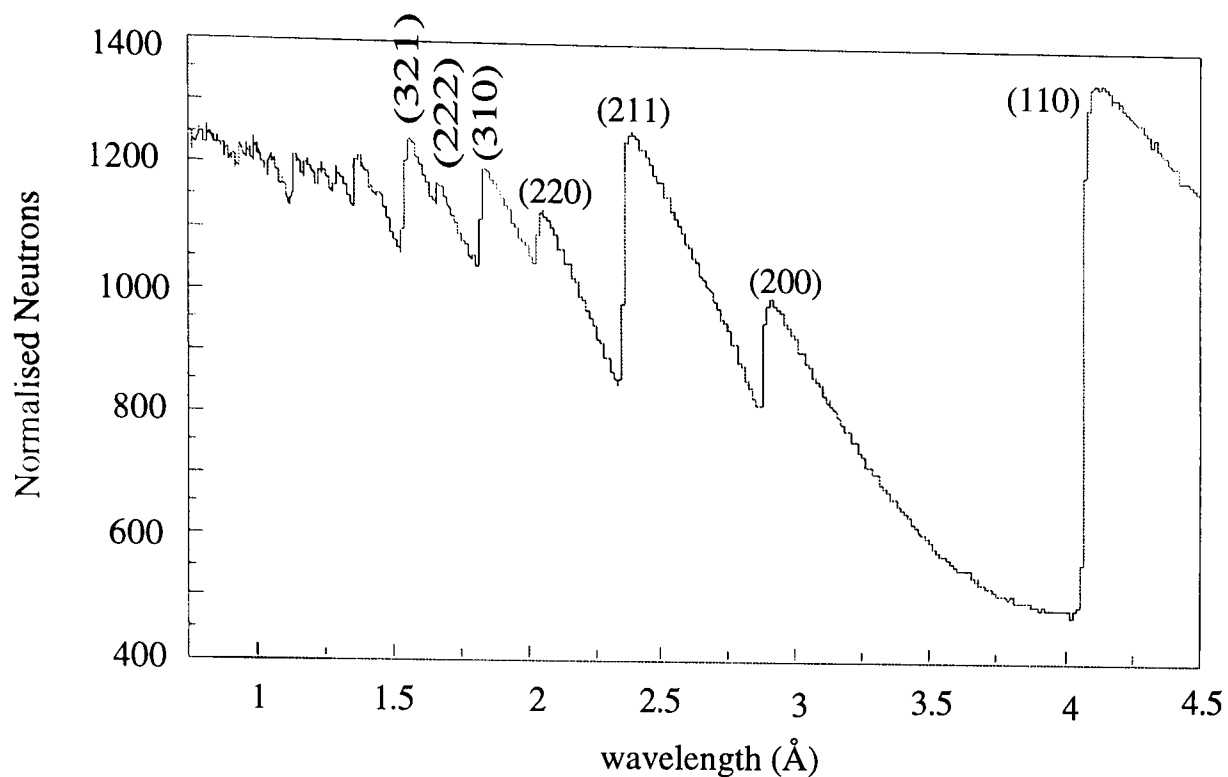
Figure 7.5 Transmission spectrum of a 10 mm wide iron bar, 500 μA.hrs (3 hrs), the slit size is 5x5 mm^2, 10% efficiency of the detector.

Individual measurements took about 2 hours and meanwhile the strains measured by the strain gauge decayed about 1%, this may cause an error. The shifts of Bragg edges were obtained by comparing the Bragg edge position at different load with that at zero load in the transmission spectra. Figure 7.6 shows that the (211) Bragg edge shift under tensile load in a 6 mm square bar. The shifts of the three largest Bragg edges, (110), (200) and (211), were obtained. The strains parallel to the neutron beam are related to the applied stress by Poisson's ratio as strain measurements of the transmission spectrometer perpendicular to the loading axis. Tension and compression are indicated by positive and negative strain values respectively. Changes in lattice strain are expressed as με.

The lattice strains for a variety of Bragg edges subject to the applied stress are given in figure 7.7, in which the line represents the strains measured by the strain gauge assuming that the uniaxial strain was homogeneously distributed in the gauge volume. The effect of residual stress in the specimen has been minimised by setting the Bragg edge under zero load as a strain-free standard.
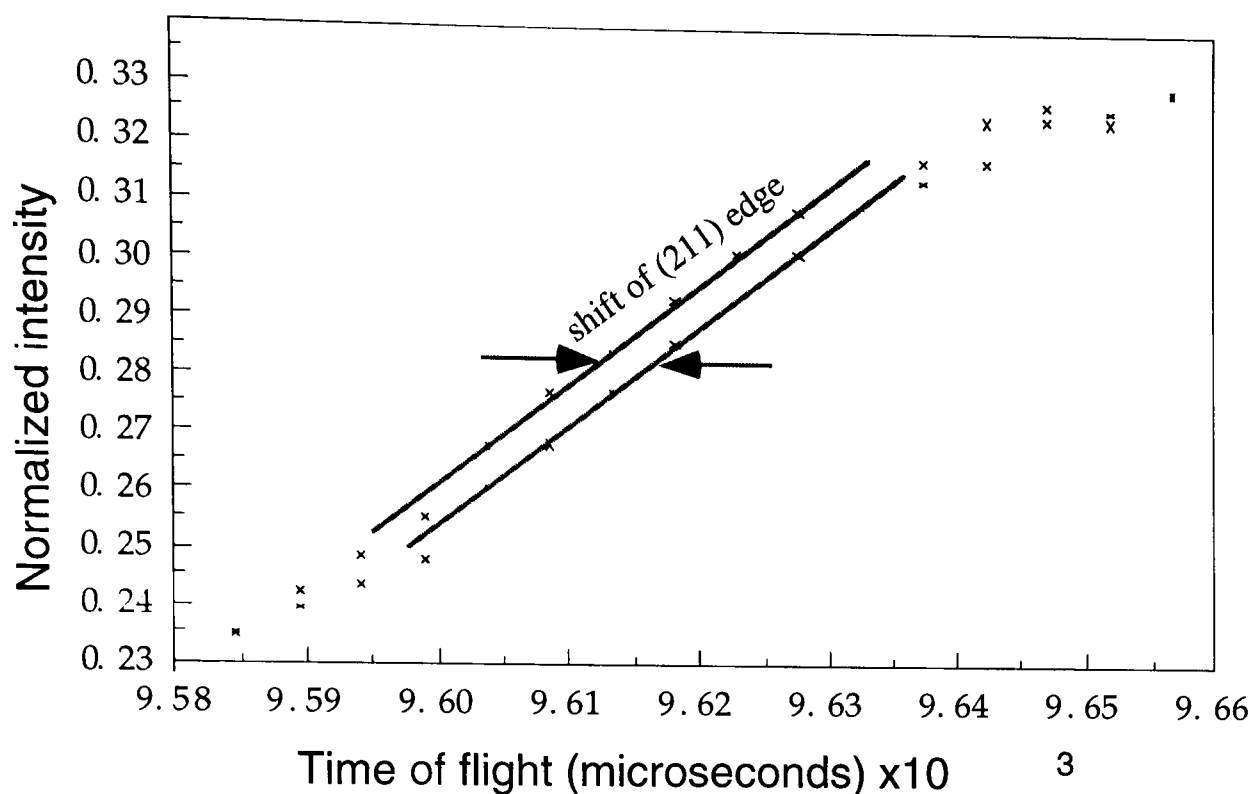
Fig.7.6 The (211) Bragg edge shift in an iron square bar under load.

The error is about ±50 µε as the efficiency of the detector is only 10%, and only individual Bragg edge was used to calculate the strains. The final strains were obtained by averaging the strains from (200), (110), (211) Bragg edges. The good agreement between the strains measured by the neutron transmission spectrometer and the strain gauge indicates that the neutron energy-dispersive transmission measurement is a feasible technique for engineering strain measurement in the direction parallel to the incident beam.

7.4 Conclusions

Calibration for neutron energy-dispersive transmission strain measurement has been made. Strains parallel to the incident beam in medium carbon steel have been simultaneously measured using the transmission technique and strain gauges. Good agreement was found.

From the experiment and analysis, one can see that the transmission geometry have several advantages over conventional diffraction geometry:

• The contribution of angular resolution to the wavelength resolution is minimised.

95
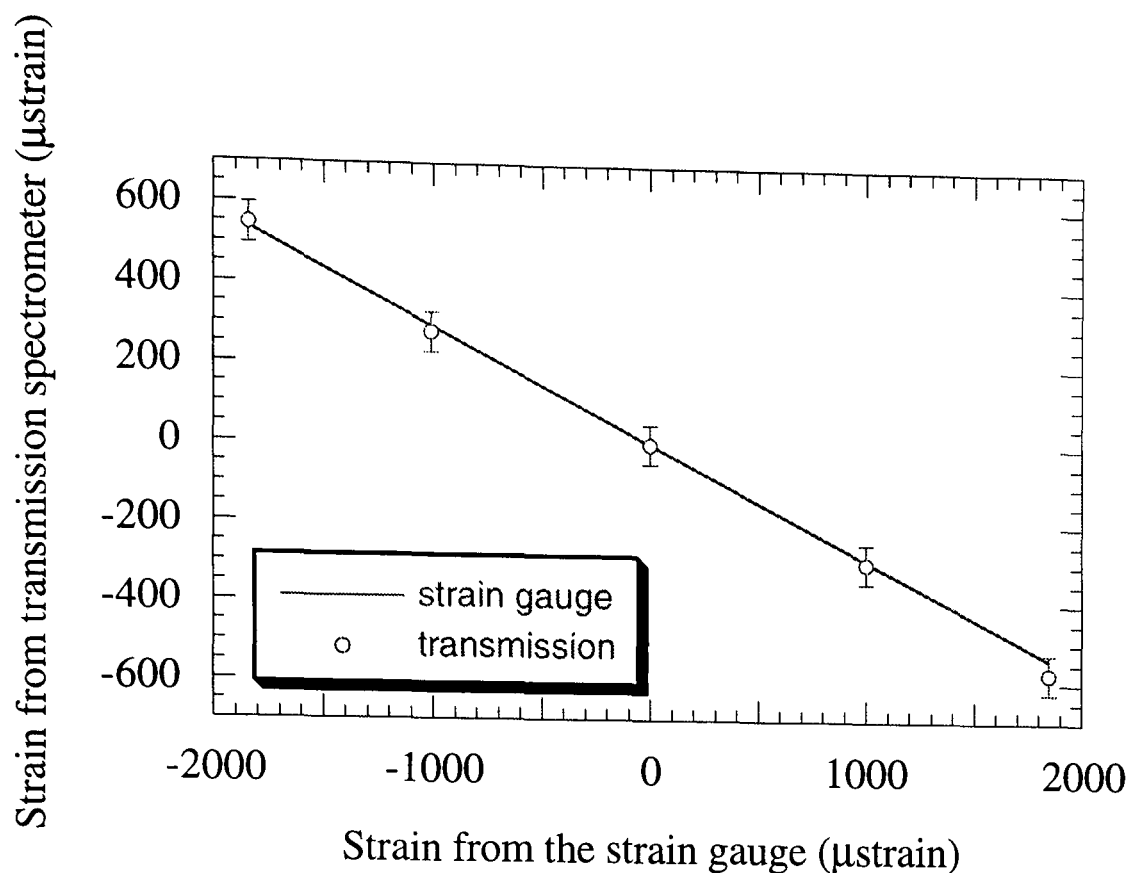
Fig. 7.7 Comparison of strains measured from the transmission spectrometer and the strain gauge. It is satisfied that the strains from transmission spectra are equal to –v (Possions ratio) times the strains from the strain gauges.

- The useful area of the neutron beam is very large.

- Sample thickness does not affect resolution so that the sample thickness may be optimised for counting statistics

- Information on scattering as a function of position in the sample is easily preserved, particularly for 2-D measurement.

The neutron energy-dispersive spectrometer can be developed to Neutron Energy-Dispersive Transmission Stroboscope with single pulse capability (only available at a spallation source), a unique instrument, which possesses high efficiency of data acquisition and high resolution, for the investigation of samples under extreme environmental conditions, which cannot be maintained over long periods of time, either ultra-high magnetic or electric fields, or ultra-high pressure, or the process of melting and solidification, which run through different metastable phases.

CHAPTER 8: EFFECT OF WAVELENGTH-DEPENDENT ATTENUATION ON STRAIN MEASUREMENT

8.1 Introduction

For most engineering components neutron diffraction measurements are made at depths up to a few centimetres. However, the neutron diffraction technique is capable of measurements at depths far greater than this. Indeed, the practical limits to such measurements are defined only by the strength of the neutron source, and the scattering and absorption properties of the material. Unfortunately, these properties usually go hand in hand and good scatterers are usually also good absorbers.

As deep measurements require longer exposures, few measurements have been made with large neutron path lengths. There have been few investigations of the effect of wavelength-dependent attenuation, though Hsu *et al* [1995] have measured compressive pseudo-strains as large as 1000 $\mu\varepsilon$ when increasing the path length to 34 mm in an iron plate, using the wavelength near a Bragg edge in a monochromatic diffractometer. This chapter will present a theoretical analysis and some dedicated experiments performed on ENGIN, to investigate the effect in aluminium and iron, by determining the diffraction pattern of a fixed gauge volume whilst differing amounts of the same material were placed in either the incident or diffracted neutron beam. Additionally, to stimulate the effect of residual strain in the material in the incident beam path, a strained steel bar was placed in the incident beam, and the Bragg edge shifts were recorded by a transmission detector. Aluminium and iron were used, as they are important engineering materials and possess different properties: the former is a low scattering and absorption material with a f.c.c. structure and the latter a higher scattering and absorption material with a b.c.c. structure.

The results and the analysis should be applicable to other engineering materials and strain measurement instruments.

8.2 Theory of Attenuation

The major effect of increasing the path length is to reduce the intensity at the detector, which leads to a requirement to increase counting times to achieve the same statistical precision. The effects of absorption and scattering on intensity can be predicted as [Bacon 1962]:

$$I(L) = I_0 \, e^{-kL} \qquad (8.1)$$

Where k is the attenuation coefficient, which is a function of the linear absorption coefficient, the total coherent scattering cross section and density of the material. The effect of coherent scattering is much larger than that of absorption in aluminium, as the linear absorption coefficient is one tenth of the total coherent scattering cross section, ($0.8 \, m^{-1}$ and $9.27 \, m^{-1}$ respectively). The total coherent scattering cross section is a function of the wavelength [Bacon 1962]. The absorption coefficent has a linear relation with wavelength but usually the variation with wavelength is small so that it is supposed to be a wavelength-independent constant. Details about the attenuation coefficient can be found in Appendix 1.

To model the effect of wavelength-dependent attenuation on peak shift, one has to calculate the total coherent cross section (secondary extinction effect), assuming that the illuminated gauge volume is an untextured polycrystalline material. The total coherent scattering cross section is then (see Appendix 1):

$$\beta_c = \frac{N_c \lambda^2}{2} \sum_{hkl} [F_{hkl}]^2 \, d_{hkl} \qquad (8.2)$$

where the sum is over all planes satisfying $d \geq \lambda/2$; N_c is the number of unit cells per unit volume; λ is the wavelength and d_{hkl} is the lattice spacing; $[F_{hkl}]^2$ is the square of the

structure factor of the unit cell for the (hkl) reflection. For the f.c.c. structure material, the structure factor square is [Bacon 1975]:

$$[F_{hkl}]^2 = b^2 \, [1 + \cos(h+k)\pi + \cos(k+l)\pi + \cos(h+l)\pi]^2 \tag{8.3}$$

and the total coherent scattering cross section is then given by:

$$\frac{N_c \lambda^2 b^2 a}{2} \sum_{\substack{d \geq \frac{\lambda}{2}}}^{hkl} \frac{[1 + \cos(h+k)\pi + \cos(k+l)\pi + \cos(h+l)\pi]^2}{\sqrt{h^2 + k^2 + l^2}} \tag{8.4}$$

Similarly, the b.c.c. structure material possesses the total coherent scattering cross section:

$$\frac{N_c \lambda^2 b^2 a}{2} \sum_{\substack{d \geq \frac{\lambda}{2}}}^{hkl} \frac{[1 + \cos(h+k+l)\pi]^2}{\sqrt{h^2 + k^2 + l^2}} \tag{8.5}$$

where a is the lattice parameter of material. From equations (8.4) and (8.5), one can see that variation of total coherent scattering section occurs in two basic ways. As can be expected, at the Bragg edges, the wavelengths satisfy:

$$\lambda_e = 2 d_{hkl} \tag{8.6}$$

where d_{hkl} is the d-spacing of the material, and there are sharp changes in the total coherent cross section, whilst between these points the variation is a more gentle function of λ^2. Thus peak shift can be explained by the fact that the reduction of intensity adds either a weight factor of $e^{-c\lambda^2}$ (c is a constant) to the peak shape function and results in negative peak shift; or a sharp variation of the intensity near transmission edge to peak shape function for peak shift depending on where the diffraction peaks locate. In other words, the effect of wavelength-dependent attenuation on strain measurement is related to all the factors determining the relative position and magnitude between the Bragg edges and the diffraction peaks, such as the experimental geometry, the crystalline structure and

texture of the material, the configuration of the instrument. The diffraction peak shift might be either positive or negative.
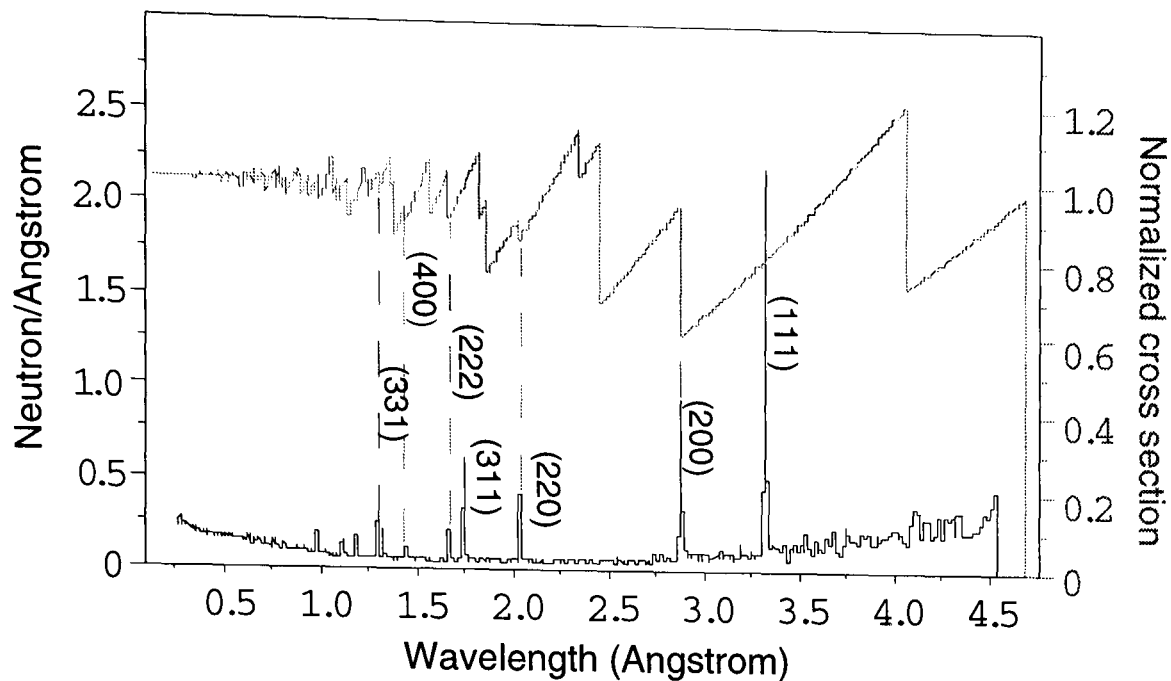
Figure 8.1 The calculated total coherent cross section of aluminium [Goldstone 1994] and its diffraction spectrum when diffraction angle is 90 degrees. It shows that when the incident beam passes through aluminium, the intensity will be reduced in such way that some aluminium diffraction peaks locate at Bragg edges.

If the diffraction angle is 90 degrees, i.e., the detectors are positioned at the direction perpendicular to the incident beam, then the Bragg equation (2.39) becomes:

$$\lambda_d = \sqrt{2}\ d_{hkl} \tag{8.7}$$

Taking into account the multiplicity of reflections in equation (8.4) and (8.5), one can obtain figures 8.1 and 8.2, which plot the cross section, normalised by its value at very short wavelengths, $4\pi b^2$, and the conventional measurements for aluminium (f.c.c.) and iron (b.c.c.) powder on ENGIN at ISIS. It can be seen that, when the neutrons travel through similar materials to the sample, each diffraction peak will sit approximately at the transmission Bragg edge if the material studied is iron; a similar effect is seen in aluminium, although few peaks are located at the Bragg edges in that case.

Both texture and strained materials in the paths may also contribute to the diffraction peak distortion since: the height of Bragg edges is controlled by texture and multiplicity of reflection [Meggers 1994], and the higher index reflections gives the lower height of

Bragg edges (see figure 8.1 and 8.2); the position of Bragg edges is affected by the strain parallel to the neutron beam (see chapter 7).
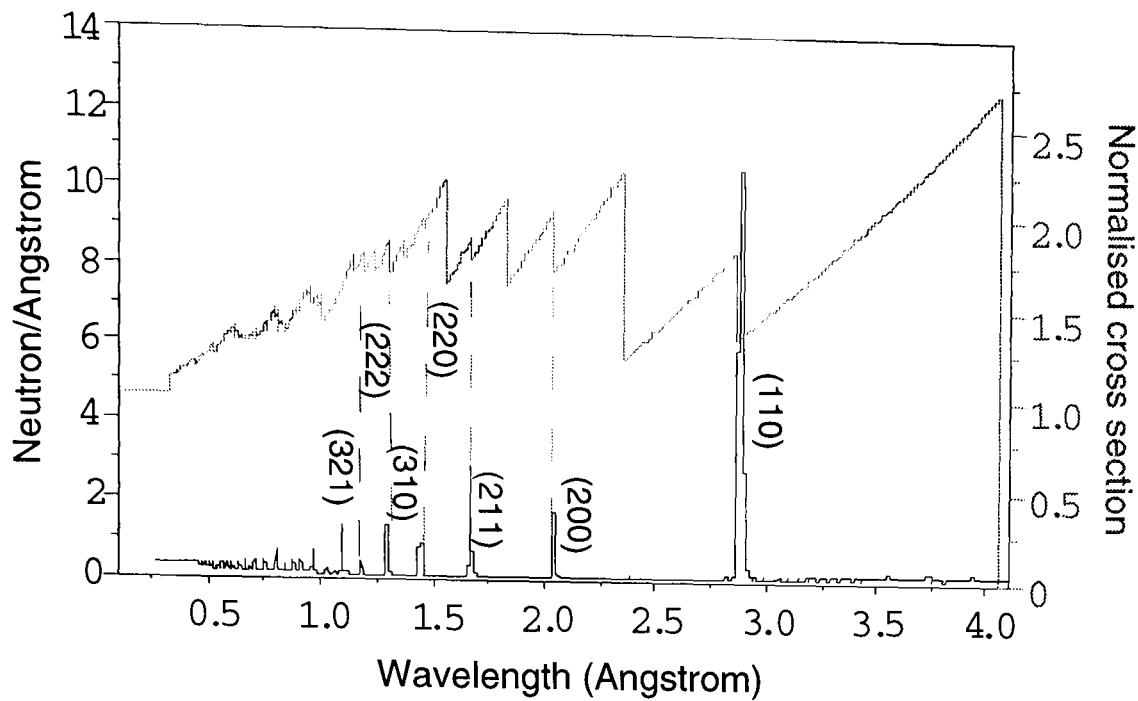
Figure 8.2 The calculated total cross section of iron and its diffraction spectrum when diffraction angle is 90 degrees.

8.3 Experimental Description

Several experiments were carried out on ENGIN. Firstly, to emulate a large component body, different numbers of plates were placed either in the incident beam or the diffraction beam as shown schematically in Figure 8.3. The materials used were a 7475 aluminium alloy, for which the path length was varied from 0 to 103 mm, and EN8 (medium carbon steel) iron, for which the path length was varied from 0 to 35 mm. The diffraction sample for aluminium was a 7475 alloy 5 mm thick bar, and the

Thickness of Al plates (mm)		Thickness of Fe plate (mm)	
incident path	diffracted path	incident path	Diffracted path
12.8	12.8	0.8	0.8
25.8	25.8	1.8	1.8
51.9	51.9	3.9	3.9
103			5.9
		9.5	9.5
		19.5	19.5
		34.9	34.9

Table 5.1 The thickness of the specimens used in the experiments. This was the plates' thickness of the material placed in either the incident or diffraction beam line.

101

gauge volume used was $7.2 \times 28 \times 1.4 \, mm^3$. The sample for iron was an EN8 2 mm thick bar. They were the same as the materials in the beam paths.
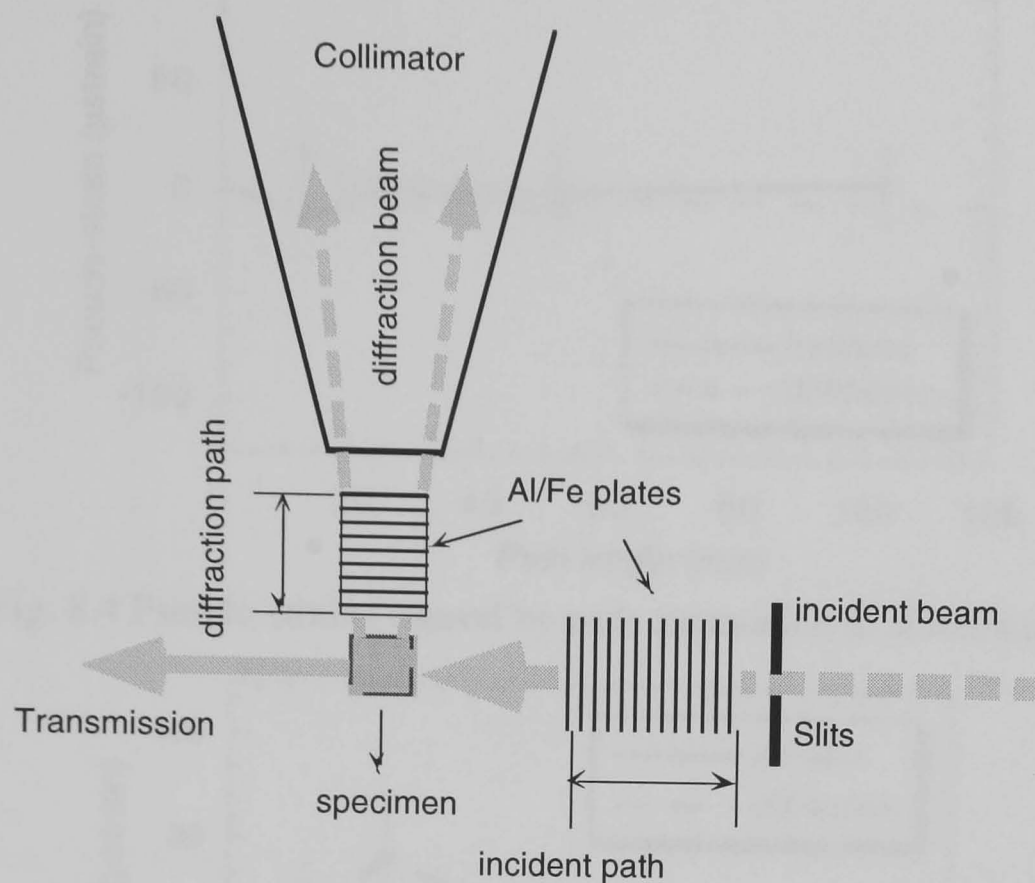
Fig. 8.3 The schematic draw for the experimental set-up

The effect of strain in the path material on strain measurement was investigated by loading EN8 square bars which were placed in the incident beam: A 6 mm wide bar was loaded in tension, and a 10 mm wide bar was loaded in compression. The macrostrains in the bars were monitored by strain gauges, and the Bragg edge shifts were derived from the transmission spectra (see chapter 7). For each path length studied, data were collected in fixed intervals to assess the counting time needed to obtain the same precision in the lattice parameter as the standard sample (no material in the incident and/or diffraction path).

As the strains are calculated from diffraction peak shifts, any effect of path length on the peak position must be understood. All the results were determined by Pawley refinement using the ISIS program CAILS (Cell And Integrated intensities Least Squares). Lattice parameter refinements include correction for anisotropic peak heights and widths, and single-peak refinements were allowed to the step for isotropic peak width.
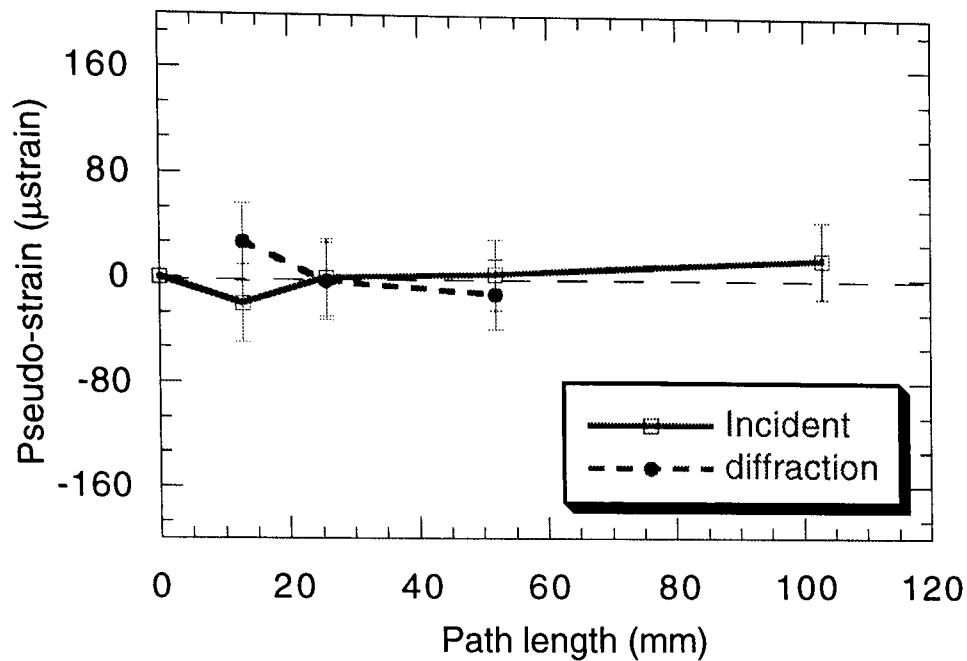
Fig. 8.4 Pseudo-strains caused by path attenuation in aluminium
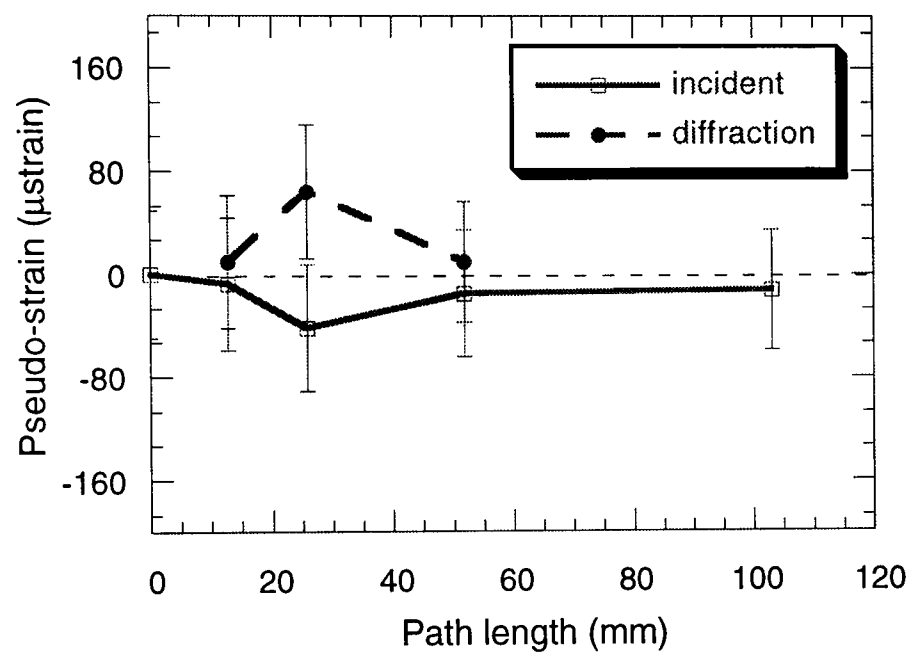
Fig. 8.5 Pseudo-strain produced by the path attenuation of aluminium.
The refinement includes only two peaks: (200) and (220)

8.4 Results

8.4.1 Effect of Attenuation in Aluminium

To investigate whether the shift in diffraction peak position occurs as the path length varies (shown in table 8.1), a comparison was made between the refinements for two peaks, (200) and (220), as well as for whole spectrum. The (200) and (220) peaks are expected to sit on the Bragg edges in aluminium. At the same time, the effect of placing material in the diffraction path and in the incident path also were compared. One can see

103

from figures 8.4 and 8.5 that the diffraction peak shift is small, within the error bar in both cases.
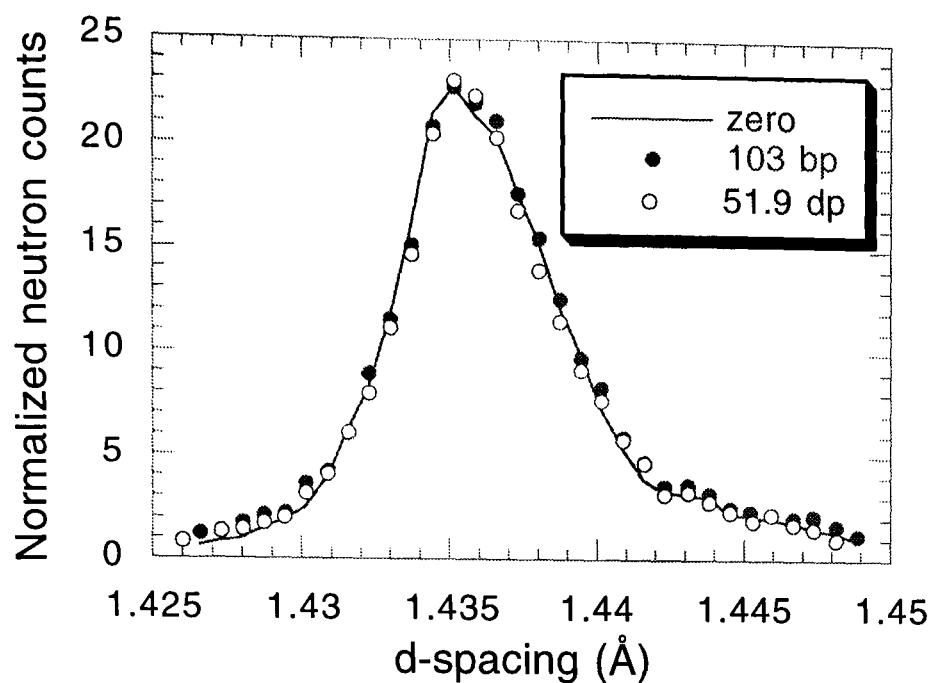
Fig.8 6 Comparison of (220) peak shape betweeen standard specimen (0 mm) path length, 103 mm incident path and 51.9 mm diffraction path length.

There is no evidence of peak shape deformation. In Figures 8.6, it can be seen that the (220) peak shape is insensitive to the amount of material in both the incident and the diffraction path, and that the peak intensity reduces as the path length increases.
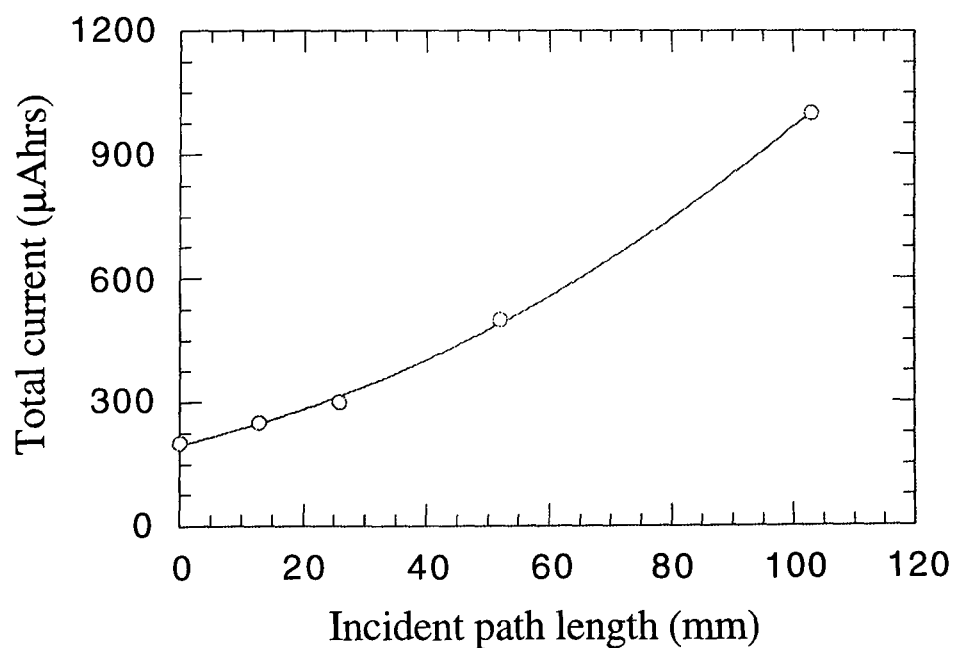
Fig. 8.7 Total beam current required to achieve an error of 2.1×10^{-4}

From the experiment one can also estimate how much the error in the measured lattice parameter changes with the variation of the path length and how long is required for a lattice parameter to be obtained to a given precision. Figure 8.7 plots the total neutron current needed to obtain a statistical error of 2.1×10^{-4} in the lattice parameter. It was found that they are satisfied with the simple quadratic relation, t (time or total current) $\propto$ L^2 (path length).
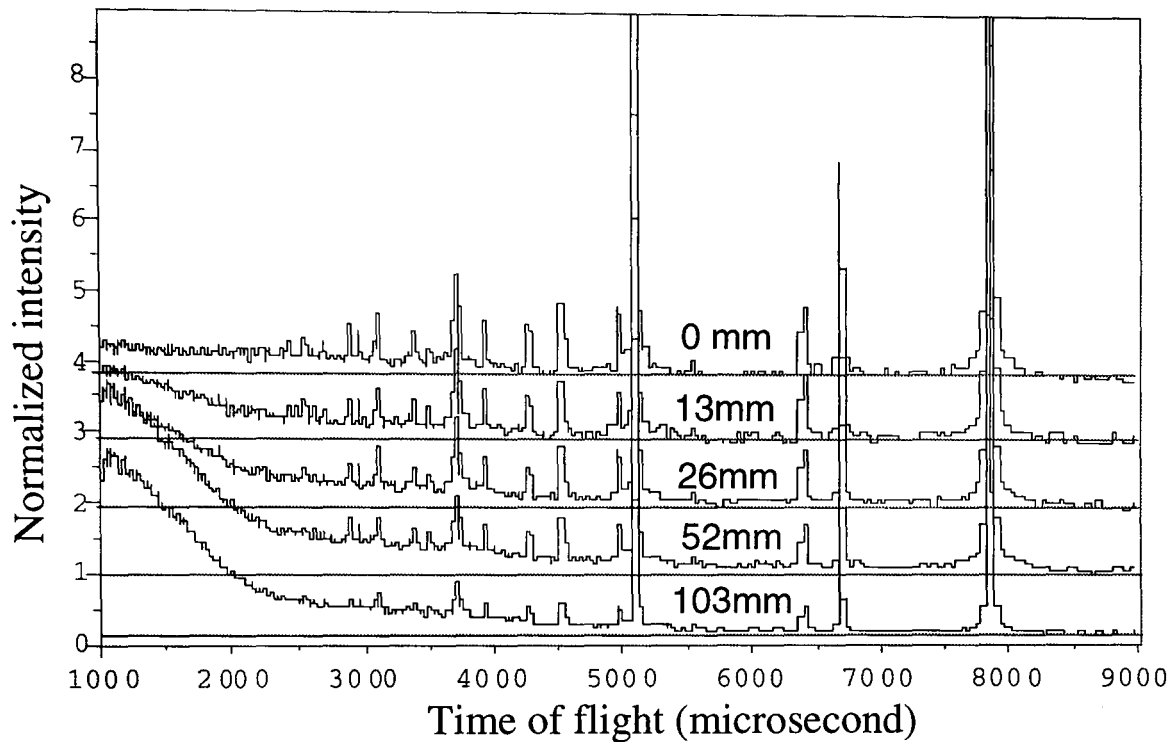
Fig. 8.8 Effect of the amount of materials in the incident beam path on background of diffraction spectrum.
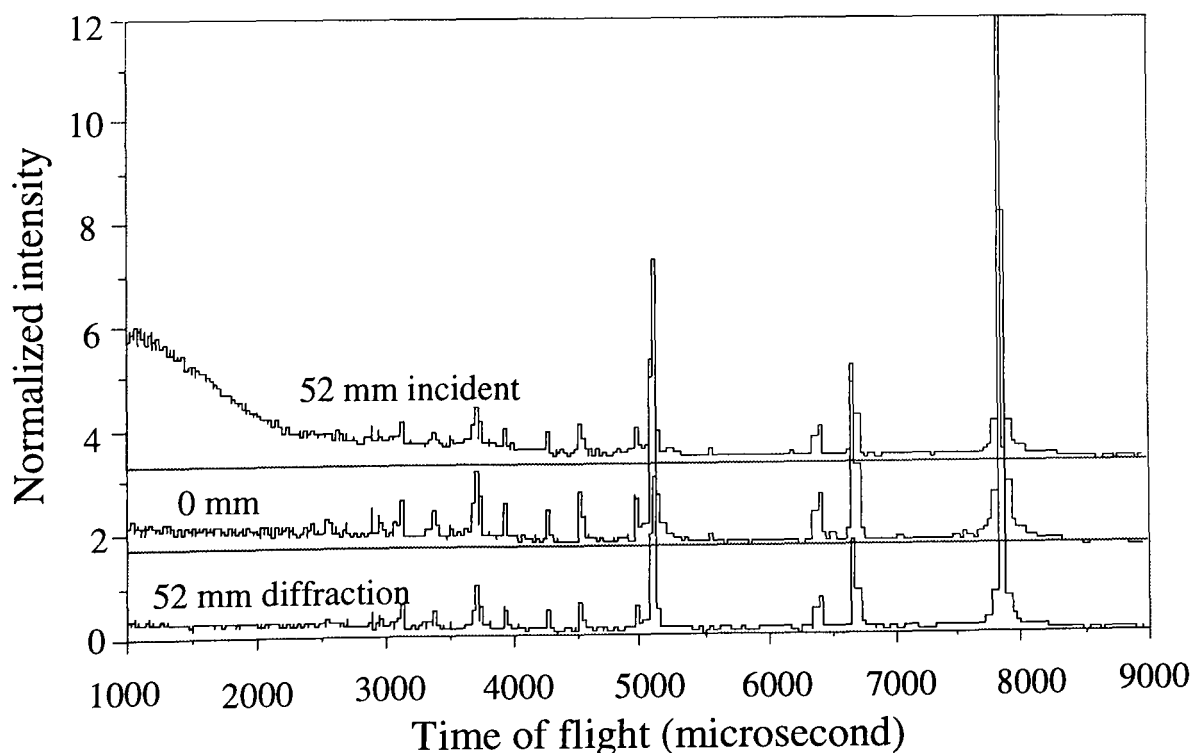
Fig.8.9 Effect of the amounts of materials in diffraction and incident beam paths on background

105

The background level was found to increase as the path length increases, particularly at short wavelengths as can be seen from Figure 8.8. In addition, this effect is larger when the material was placed in the incident path than in the diffraction path, as shown in figure 8.9.
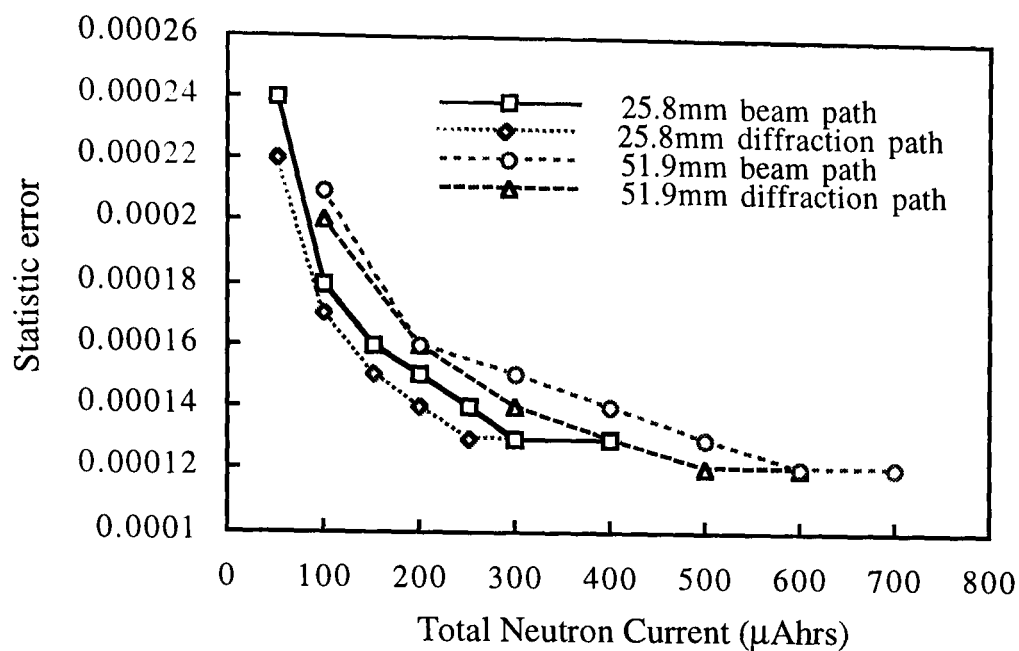
Fig.8.10 Effect of materials in the beam paths on statistical error for lattice parameter measurement.

The different background detected, when material was placed either in the incident beam or in the diffraction beam, suggests that multiple scattering is a factor because it has a stronger effect at short wavelengths (higher energy neutrons), as shown in Figure 8.8 and 8.9. Furthermore, material in the incident path has a stronger effect on the background than material in the diffraction path, as neutrons of all energies can take part in multiple scattering in the incident path, whereas only neutrons whose wavelengths match the Bragg condition do in the diffraction path. Thus, the statistic error at a given neutron current is slightly higher when material placed in the incident beam than in the diffraction beam as shown in figure 8.10.

8.4.2 Effect of Attenuation in Iron and Transmission Measurements

The same experimental geometry was used for studying the attenuation effect in iron. Additionally, to investigate how the incident beam intensity varies with the incident path length, the transmitted intensity was recorded by a glass scintillator detector. The thickness of the iron plates used is shown in table 8.1. The transmission spectra are shown in figure 8.11. It can be seen that the beam intensity was reduced, as a function of wavelength, as the path length increased. By comparing the transmission spectra with the diffraction pattern, as shown in figure 8.12, one can see that all the diffraction peaks are located at the Bragg edges as expected.

The peak shift is small (figure 8.13), although every peak is supposed to be at a Bragg edge; and even with the incident beam intensity decreased to 5% of its original intensity. In order to evaluate whether the larger Bragg edges have a stronger effect on the diffraction peak shift, individual peak shifts for (110) and (200) were also examined by using single-peak refinement. It was found that the effect is still negligible, as shown in figure 8.14.
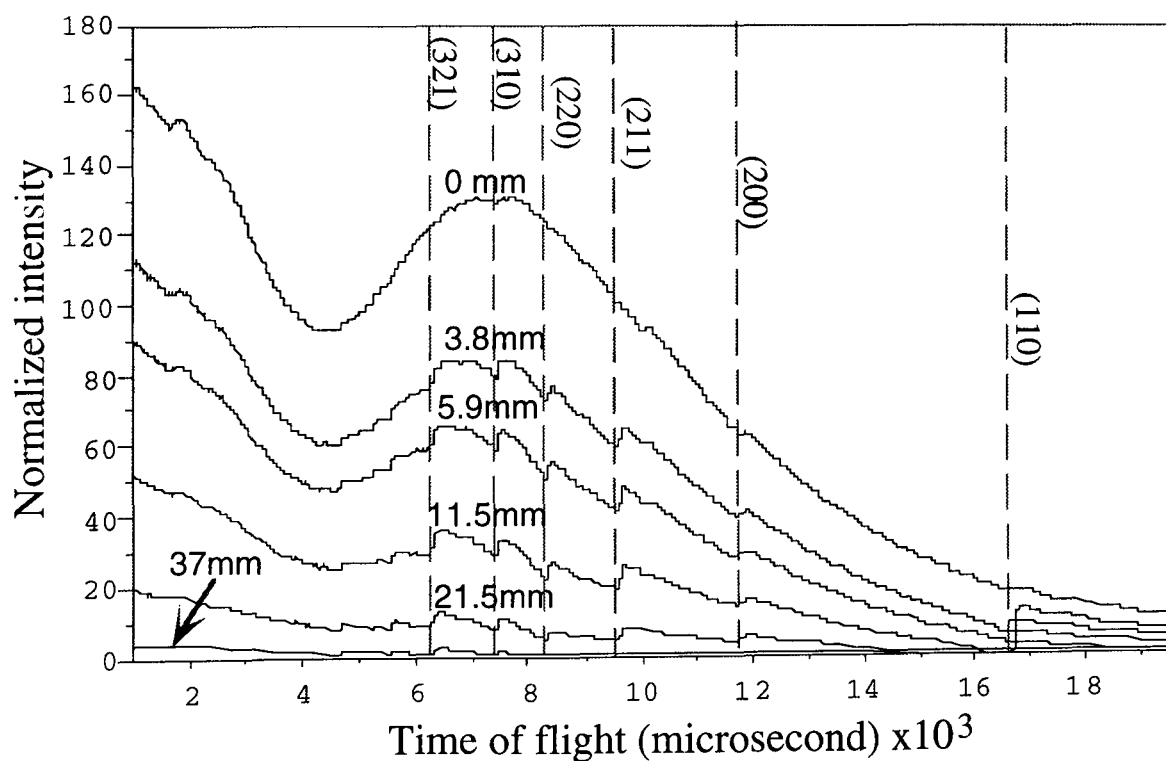
Fig. 8.11 The intensity of neutron beam is reduced in a wavelength-dependent way as it passes through iron plates.
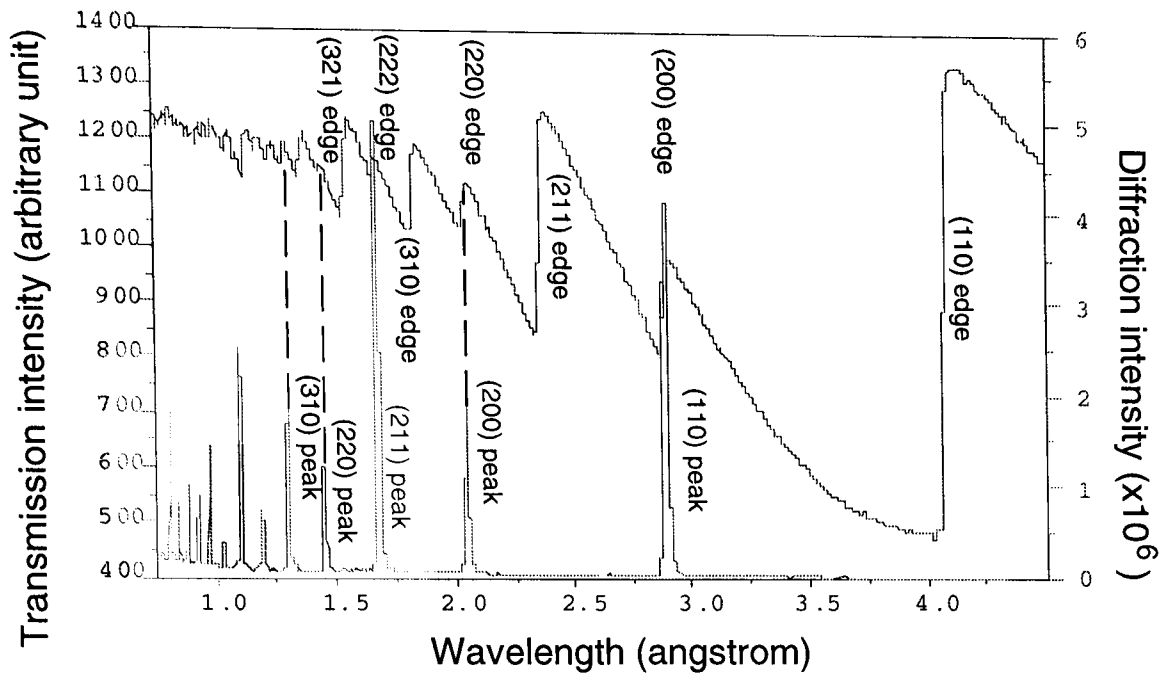
Fig. 8.12 Comparison of the diffraction pattern at 90 degrees diffraction angle and the measured transmission pattern of iron.
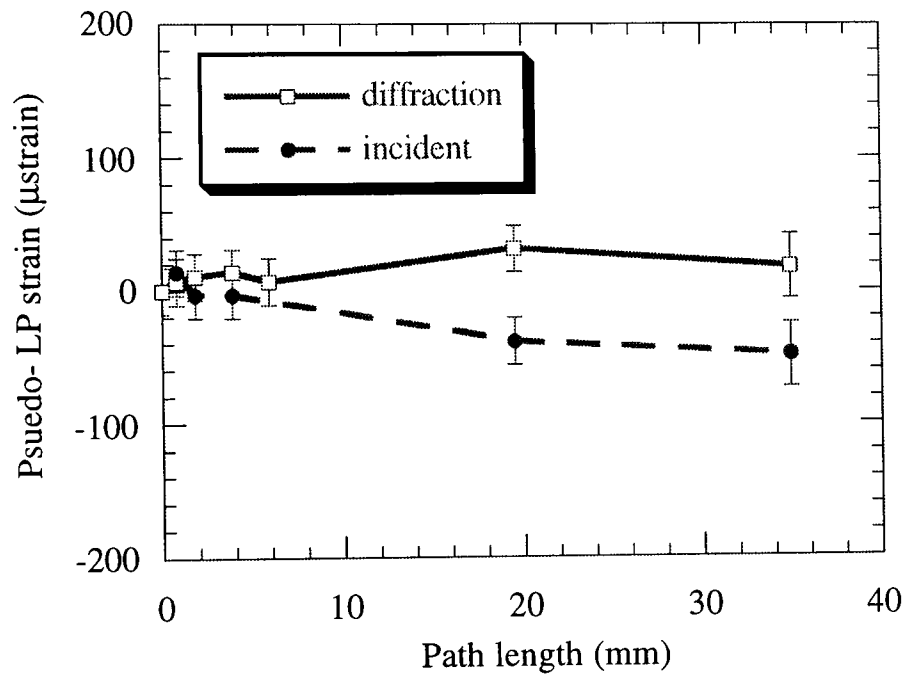
Fig. 8.13 Pseudo-strain induced by wavelength-dependent path attenuation in iron.
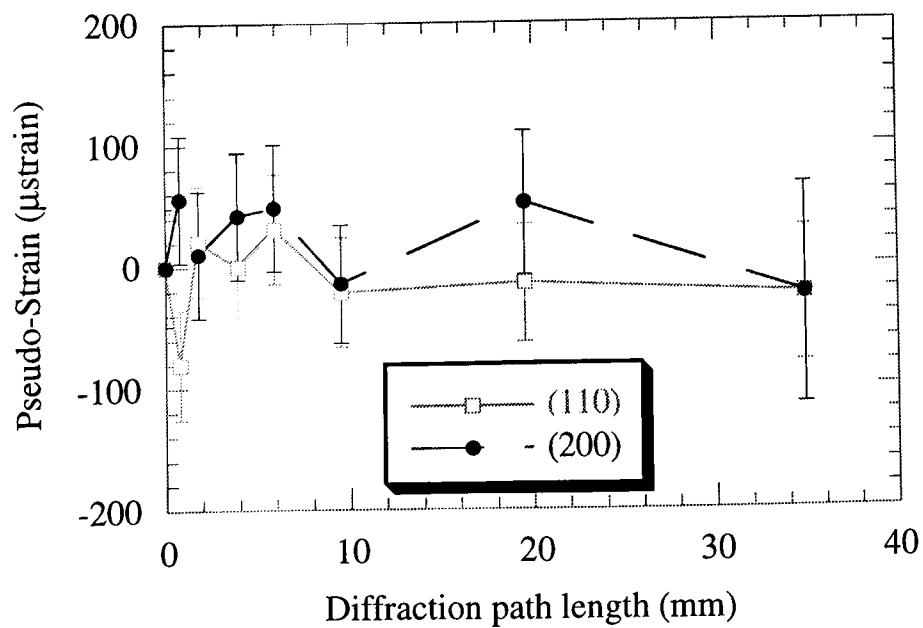
Fig. 8.14(a) Pseudo-strain induced by attenuation of iron for individual peaks: (110) and (200)
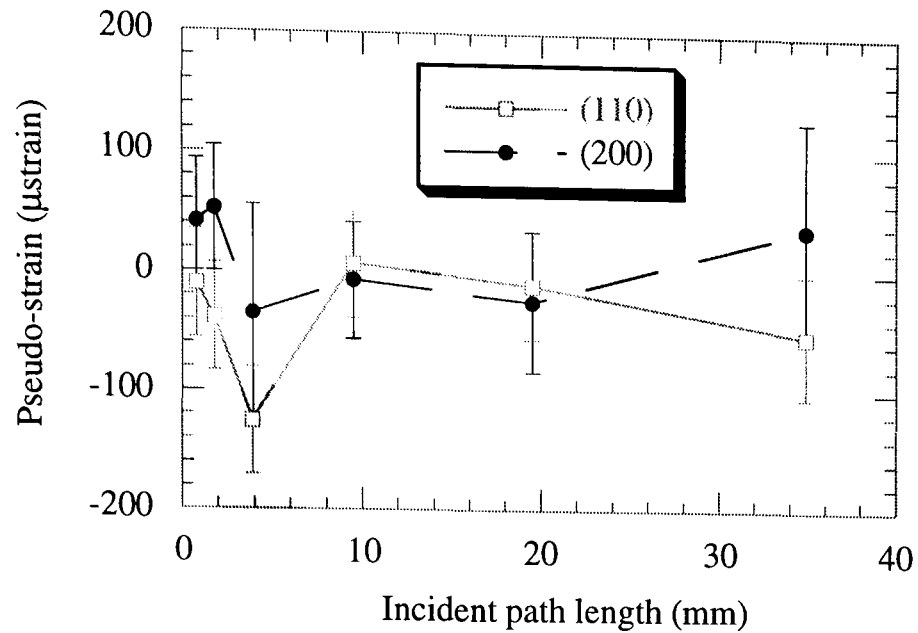
Fig. 8.14(b) Pseudo-strain induced by attenuation of iron for individual peak: (110) and (200).

Strain measured by the shift of Bragg edge (μstrain)
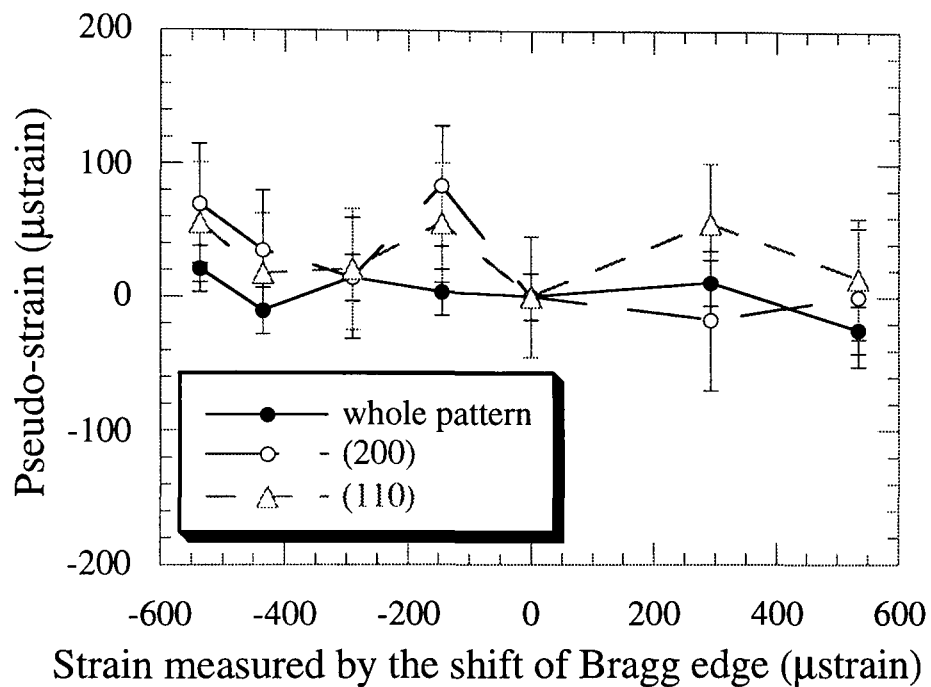
Fig. 8.15 Pseudo-strain induced by Bragg edge shift in the path material which is the same material as the specimen. The Bragg edge shifts were produced by an external load.

8.4.3 Effect of Strained Material in the Incident Beam

Experimental details can be found in chapter 7. Square bars perpendicularly placed in the incident beam were sequentially subjected to uniaxial macrostrains, of 1850, 1500, 1000, 500, 0, -1010, and -1840 με, monitored by strain gauges to investigate the effect of the presence of strained material in the incident beam. Only the strain parallel to the beam can cause the Bragg edge shifts as the Bragg edges represents the lattice spacing

perpendicular to the beam (see chapter 7). The sequential strain parallel to the beam in the bars were -537, -435, -290, 0, 293, 534 $\mu\varepsilon$ respectively (see chapter 7).

It can be seen from figure 8.15 that the diffraction peak shift was not obvious, although the Bragg edge observably shifted from about 500 $\mu\varepsilon$ to -500 $\mu\varepsilon$. This means that the strained materials in the incident beam also has a negligible effect on strain measurement, for a strain scanner with a radial collimator and using a "white" neutron beam.

8.5 Discussion

The experiments shows that the ENGIN instrument is insensitive to the effect of wavelength-dependent attenuation on strain measurement. This might be due to the fact that the three banks of 135 detectors spread over 17 degrees such that the diffraction peaks in most detectors are away from the Bragg edges. From equation (2.43) one can obtain the time shift induced by the variation of diffraction angle 2θ is:

$$\Delta t = 5455 \ d \cos\theta \ \Delta\theta \tag{8.8}$$

where d is the lattice spacing. Like what we have discussed in the section 8.2, when the diffraction angle is 90°, all the diffraction peaks locate at the Bragg edges for iron, and some of the diffraction peaks do for aluminium. The strongest effect of the Bragg edges on diffraction peak shift would occur where the strongest Bragg edge meets the diffraction peak. Using equation (8.8) to estimate the width of the (110) diffraction peak and the (200) Bragg edge, and taking the ENGIN's geometry into account, it is found that only 17% of the detectors on ENGIN can be affected due to the overlap between the Bragg edge and the diffraction peak in the worst situation: (110) diffraction peak meets (200) Bragg edge for iron. Furthermore, the effect from those 17% detectors resulting in a positive peak shift might be offset by that from the remain 83% detectors, which are affected by a weight factor of $e^{-c\lambda^2}$ (c is a constant) in the peak shape function, giving rise to a negative peak shift. Another reason might be that the Bragg edges at longer

wavelengths have larger magnitude, but in this region the diffraction peaks contribute less to the lattice parameter (see chapter 3.9).

When a load is applied to the path material, inducing a Bragg edge shift, it therefore also unlikely to have a large effect. Nevertheless, the distortion of the diffraction peak shape is unobservable, as shown in figure 8.6 and 8.16. Figure 8.16 shows the comparison of the (110) peak shape when the path length varies from z e r o mm to 37 mm. The peak broadening due to increase of the path length can be found in figure 8.16. As a consequence it is clear that wavelength-dependent attenuation caused by material in both the incident and diffraction paths has a negligible effect on diffraction peak shift on ENGIN.
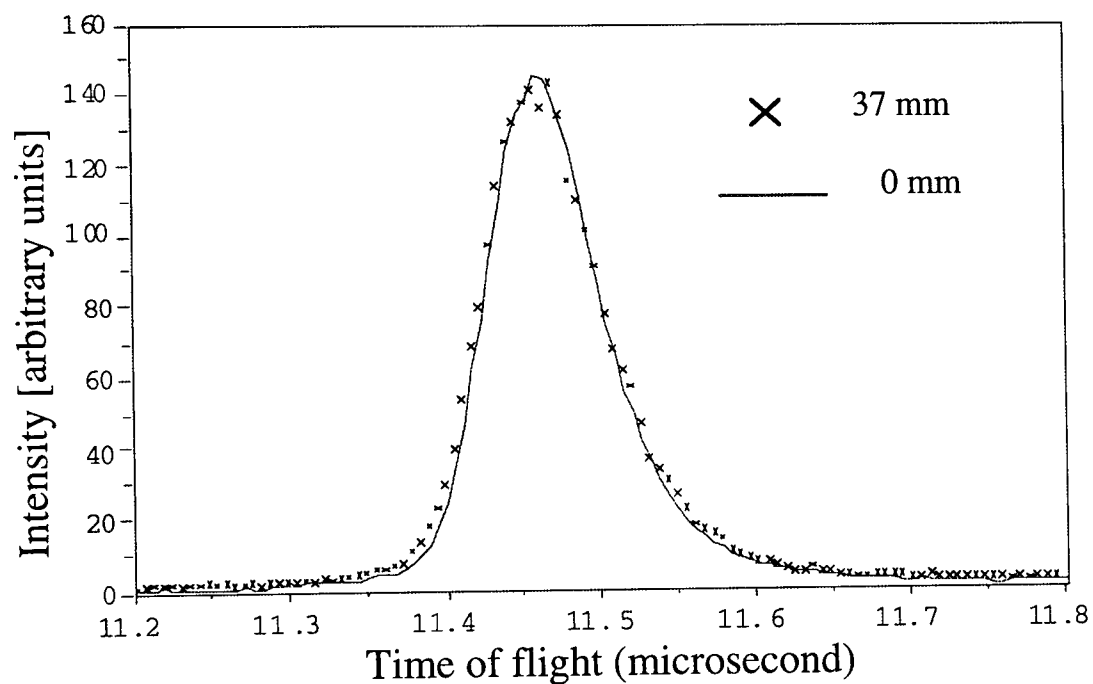
Figure 8.16 Comparison of the diffraction (110) peak shape with zero and 37 mm path length

Because of the effect of wavelength-dependent attenuation, care should be taken when determining texture as a function of depth in a sample. The relative intensity in figure 8.17 shows the peak intensity ratio of the highest peak to other peaks varies as the amount of materials in beam path varies. It can be found that with no added material in the incident path, the highest peak is (200) peak, whilst the (222) peak becomes the highest one when 37 mm of material is put in the incident beam: the wavelength-dependent attenuation does change the peak intensity ratio in the diffraction spectrum.
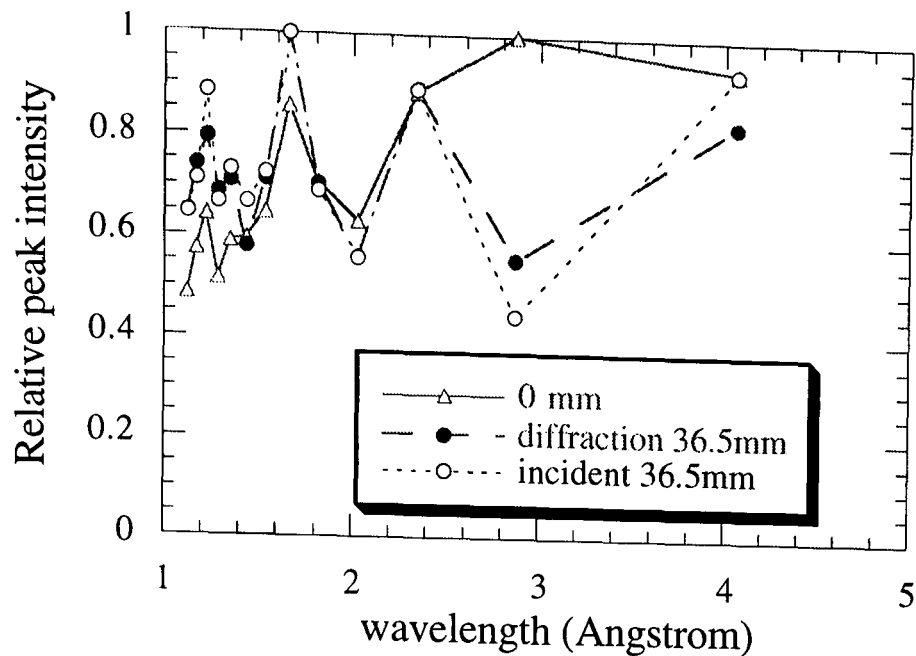
Fig.8.17 The variation of the diffraction peak height ratio with the path
length. The ratio for 0 mm path length comes from the value, a peak height
is divided by the highist peak height, which is (200) whereas for 36.5 mm
path length diffraction, the highist peak is (321)

8.6 Summary

- The effect of wavelength-dependent attenuation on peak position was found to be
  negligible in the energy-dispersive strain scanner with radial collimators and multi-
  detectors, although the incident beam intensity reduced as a function of wavelength as
  the path length increased. Both the measurement precision and the peak intensity
  were affected.

- Shifts in position of the Bragg edges do not change diffraction peak position.

- The total neutron current (measurement time) needed to obtain a given error in lattice
  parameter is proportional to L^2, where L= path length of material in the beam.

- The background level of the spectrum is proportional to the path length of the material
  in the beam, especially at short wavelengths. The effect is stronger when material is
  placed in the incident beam than in the diffraction beam, due to multiple scattering
  effect. This results in a slightly larger statistical error when material is present in the
  incident beam path.

112

- The reduction of the diffraction peak intensity, as a function of the amount of material in the beam path, shows that great care should be taken when measuring texture as a function of depth in materials.

- An explanation for the effect of material in the path on peak shift was presented. It indicates that wavelength-dependent attenuation from materials in both incident and diffraction paths may affect diffraction peak position, either positively or negatively, by distorting the diffraction peak shape, depending on the relative position and magnitude between the Bragg edges and the diffraction peaks, which are relevant to the experimental geometry, crystalline structure and texture of the specimen as well as the configuration of the instrument.

FACULTY OF TECHNOLOGY

Materials Department

MEMORANDUM

FROM	Dr Andrew Greasley	**REF**	AG/ef
TO	Prof. D Laurillard, PVC New Technology	**TEL**	5102
		DATE	5.11.96

SUBJECT

I was recently requested to join a video conference with some academics in Brisbane.

My initial enquiries with the campus telecommunications office indicated no on-site facility. My next enquiry at KMI suggested the VC's office as the Business School or the London regional office. I have since found that a couple of PC based systems are possibly located in KMI.

I eventually tracked down one in the OU Business School. However, the local expertise was insufficient to make a successful test transmission.

Finally I have received excellent support from David John an account manager at Mercury Communications and contributed to a $1\frac{1}{4}$ hour conference using their system in Bletchley.

Might I suggest that we need considerable rationalisation and improved on-site awareness as we move towards increased use of these facilities. I probably wanted about a day in setting up my end of the conference and would not like other colleagues to have to go round the same maze.

Dr Andrew Greasley
Materials

CHAPTER 9: CONCLUSIONS AND RECOMMENDATIONS

9.1 Introduction

A dedicated instrument for engineering strain measurement — ENGIN, has been set up, which has an accurate positioning and slit control system as well as an efficient data acquisition and analysis system. The systematic error, resolution and application for the strain measurement of ENGIN have been presented. 3-D stress distribution near a cold expanded hole was measured, which validated the measurement using a modified Sach's method. Additionally, the improvement of near-surface strain using neutron diffraction has been made by precisely determining the sample position, calculating centroid position of gauge volume and correcting the anomalous surface effect of the multi-detector system. Furthermore, strain distributions in a Q-joint under zero and 30 kN load were measured. The principal conclusions from all the experiments performed are presented with recommendations for future work in this chapter.

9.2 Summary and Main Conclusions

9.2.1 Instrument Configuration

ENGIN possesses the resolution about 5×10^{-3} and complete data acquisition and analysis systems which allow whole pattern recording and both whole and part pattern refinement (Pawley method), as well as positioning and slit controlling systems. The accuracy of position and angle can be achieved to 0.01 mm and 0.01°, respectively. The physical spatial limitation for ENGIN is about $160 \times 160 \times 300+ \, mm^3$, and the weight limitation is 250 kg. The incident beam has the divergence less than 3×10^{-3} rad. The size of the

incident beam can be changeable from 0.5x0.5 to 25x25 mm². The two collimators permit the measurements more efficiently performing simultaneously at two orthogonal directions and define one dimension of the gauge volume to ≈1.4 mm.

9.2.2 Systematic Error Associated with Strain Measurements

The principal systematic errors arise from the relatively large gauge volume. The gauge volume average could generate a large error if there is a large strain gradient. There is a large systematic error when measuring near-surface strain perpendicular to the surface as the gauge volume partially immerses in specimen and correction is needed. The correction can be made using either Monte Carlo simulation or powder scanning. The systematic error is negligible in the circumstance when strain measurement is performed deep in materials on ENGIN. The diffraction angle averaging of the collimators and an insufficient measurement time might cause a large systematic error depending on the instrumental configuration.

9.2.3 Strain Measurements on ENGIN

- A demonstration strain measurement in a diametrically plastically compressed ring has been made. The result agrees well with that from LANSCE (Los Alamos, USA) and CRNL (Chalk River National Lab, Canada). LP (lattice parameter) strain can be used to represent type I bulk strain in components.

- An explanation for the effect of wavelength-dependent attenuation on peak shift was given, which reveals that it may affect diffraction peak position, either positive or negative, by distorting diffraction peak shape, depending on the relative position and magnitude between Bragg edges and the diffraction peaks, which are relevant to the experimental geometry, crystalline structure of the specimen and the configuration of instrument. The experiments for iron and aluminium were carried out and the results

show that there is no effect on the distortion of peak shape which can induce systematic error in strain measurement but the multi-scattering can affect the statistical error on ENGIN.

- Calibration measurements on iron and aluminium powder shows that the near-surface strain measurements at the direction perpendicular to sample surface has a large systematic error so that it needs correction using either Monte Carlo or experimental method but there is a small systematic error for the near-surface strain measurement at the direction parallel to sample surface. The variation of gauge volume size also results in an unexpected systematic error.

- The strain measurements on a shot-peened surface in titanium alloy within 1 mm from surface reveals that there is a compressive strain in the shot-peened surface with peak strain of $-5500\,\mu\varepsilon$ at 0.1 mm from surface and becomes zero at about 0.6 mm. Neutron diffraction technique is capable of measuring the strain within 1 mm from surface if the methodology are applied: precise determination of specimen position, centroid position calculation and correction for surface effect. Neutron diffraction measurement is comparable to that from X-ray diffraction bearing in mind that there is a big difference of gauge volume and reflection "averaging" between them.

- A 3-D residual stress surrounding a cold expanded hole in a high strength aluminium alloy plate was measured. The result agrees well with that from modified Sachs' method after taking into account the effect of gauge volume averaging. The parameter, Σ_2, in Pawley refinement programme can be used as an indicator of variation of macrostrain gradients in the material.

- Calibration strain measurement for an energy-dispersive neutron transmission spectrometer was performed on ENGIN for the first time using iron bars and specially-designed rigs. Known strains measured by strain gauges agree well with that from the transmission spectrometer.

- Strain distributions on the TT section immediately adjacent to the fasteners and on a remote RR section in a Q-joint under zero and 30 kN load were measured using neutron diffraction. The former provides dramatic confirmation of the excellence of the joint design as the fastener system has completely shielded the fastener hole from deleterious tensile strains under operational loading. The latter shows a comparable secondary bending ratio with strain gauge measurement and finite element analysis. Both strain distributions show similar pattern with that of finite element analysis.

9.3 Recommendations

ENGIN is a dedicated strain scanner which has the gauge volume with one dimension fixed by the collimators, only about 1.4 mm. This limits the gauge volume size in the direction and could be improved by making the collimator's mouth "open" more and changeable hence the size of the gauge volume varies from 1.4 mm to 25 mm.

One of the Rietveld methods, Pawley refinement, has been used to analysis the data. A problem sometimes occurred is that it crashes due to failed fitting when the parameters in ccl file are not suitable. A possible solution is using the refined ccl file of previous run for the following refinement. This can be achieved by adding one more option in the batch mode program.

Some more cards in ccl file (see Appendix 2) are needed, such as S cards (symmetry cards) if crystalline structure of the material measured is not cubic. It would be more convenient to users if a data base including such information is prepared.

Further investigation is needed if there is a strong texture in material. As mentioned in chapter 3.9 and Appendix 4, diffractometers at reactor and spallation neutron sources work in a different way. The former measure diffraction peak shift for individual peak (lattice spacing shift) whereas the latter record whole diffraction pattern and the shift of peaks is derived from a kind of 'averaging' over several reflections, called LP (lattice parameter) shift. When material is strongly textured and anisotropic, great care should be

taken to choose proper reflection for representing bulk strain of the material. For those at spallation source, calibration measurements should be carried out to make sure the LP strain is the bulk strain of the material.

A calibration measurement for an energy-dispersive neutron transmission spectrometer have been performed for the first time on ENGIN in which the strains measured by strain gauge agree well with that from the transmission spectrometer using single reflection. To improve accuracy the Rietveld method should be developed. A new technique called energy-dispersive neutron transmission stroboscope (ENTS) can be exploited, which is a method with a high resolution as the backscattering and with more statistical accurate advantages. The very high instantaneous neutron flux of a spallation neutron source combined with high resolution of the transmission diffraction can be used to set up the ENTS, which can only be available at ISIS and LANSCE. Structural dynamic information can be extracted from single neutron pulse transmission spectra, delivered at a rate of 50 Hz at ISIS. This opens numerous possibilities for new and exciting experiments to study dynamic processes like quantitatively determining phase volume and texture *in-situ*, measuring hydrostatic and type-II strain in composites/ceramics and recognising structure of materials.

APPENDIX 1: NEUTRON ATTENUATION IN MATERIALS

This section covers the calculation of neutron attenuation coefficient in materials and are applied to Chapter 7 and 8.

A1.1 Linear Absorption Coefficient

When neutrons enter a specimen, the attenuation comes from absorption and scattering. The intensity of transmitted radiation reduces as the distance travelled by the neutron through the material increases. The strength of attenuation determines the maximum distance in a component over which neutrons may travel and still have sufficient intensity for a scattering measurement. In principle, engineering components can necessitate path lengths of up to several centimetres and the measurements are usually determined by the available beam time.

Increasing thickness of an absorber in a neutron beam causes an exponential decay in the intensity of transmitted radiation. The decay can be derived by assuming that the reduction in transmitted intensity caused by a small thickness of absorber is proportional both to the initial intensity and the thickness:

$$I = I_0 \, e^{-\mu L} \qquad\qquad (A1.1)$$

where μ is the linear absorption coefficient, L is the thickness of sample; I_0, the initial intensity. From equation (A1.1) the thickness for 50% absorption is $\ln 2 / \mu$.

The constant μ has a linear relation with wavelength but usually the variation with wavelength is very small so that it is supposed to be a wavelength-independent constant.

A1.2 Scattering Cross Section

The second attenuation factor is scattering: multiple scattering, coherent (secondary extinction effect) and incoherent scattering as well as magnetic scattering. The scattering probability for neutrons impinging on a specimen is related to the cross sectional area presented by the nuclei in it.

If the wavelength of the incident neutrons is much larger than the range of the strong nuclear force then the target nuclei can be treated as identical, non-interacting particles of constant cross section. The strength of interaction is characterised by a scattering length, b, which depends on the atomic species, isotope and spin state. The sign and magnitude of b change irregularly with atomic mass and number. When atoms of one species scatter in the same way the scattering is coherent and is associated with a coherent cross section, β_c, which is relevant to crystal structure of the material. Random fluctuations in the isotopic distribution and spin alignments cause incoherent scattering described by a incoherent cross section β_i. The attenuation caused by absorption is described by β_a. The scattering intensity depends on whether the nucleus is fixed or free to recoil in the scattering process. For most condensed matter experiments the fixed atom is a reasonable approximation and it is conventional to quote bound atom values for scattering cross sections. The scattering and absorption cross sections have been measured for most elements and isotopes at a certain wavelength (1Å) and are typically of the order of $10^{-28}\,\mathrm{m}^2$ or 1 barn.

If the material consists of only one element, the attenuation coefficient k is

$$k = \frac{\rho\ (\beta_c + \beta_i + \beta_a)N_A}{A} \tag{A1.2}$$

where ρ is the density of the material; N_A, Avogadro's number; A, the atomic mass of the element.

If the material is an alloy, then the attenuation coefficient is given by:

$$k = \rho \, N_A \sum^{j} \frac{w_j (\beta_c + \beta_i + \beta_a)_j}{A_j} \qquad\qquad (A1.3)$$

where w_j is a weight function of species j and:

$$\sum_j w_j = 1 \qquad\qquad (A1.4)$$

For the strain measurement on engineering materials, the total coherent scattering cross section is an important parameter as it represents the ability of scattering of the material, e.g. the efficiency of measurement.

The total coherent cross section is wavelength-dependent and relevant to crystal structure of the material. Assuming that the illuminated gauge volume is a polycrystalline material with a random orientation, then the total coherent scattering cross section is [Bacon 1975]:

$$\beta_c = \frac{\pi N_c}{2\kappa^2} \sum_{hkl} 4\pi [F_{hkl}]^2 \, d_{hkl} \qquad\qquad (A1.5)$$

where the summation is over all planes, (hkl), which are capable of giving Bragg reflections at a given neutron wavelength; N_c is the number of unit cells per unit volume; $[F_{hkl}]^2$ is the square of the structure factor of the unit cell for the (hkl) reflection; κ is the wave number; and d_{hkl} is the d-spacing. The wave number can be replaced by the wavelength: $\kappa = 2\pi/\lambda$ so that:

$$\beta_c = \frac{N_c \lambda^2}{2} \sum_{hkl} [F_{hkl}]^2 \, d_{hkl} \qquad\qquad (A1.6)$$

Where the sum is over all $d \geq \lambda/2$ and where

$$[F_{hkl}]^2 = \left[\sum^{j} b_j \cos 2\pi \, (hu_j + kv_j + lw_j) \right]^2 \qquad\qquad (A1.7)$$

where the sum is over the unit cell.

121

In fact the attenuation is mainly contributed by linear absorption and coherent scattering in conventional engineering materials. Examples of μ and β_c at 1.08 Å are given in table A1.1.

Table A1.1 Absorption Coefficients for Different Elements

Element	Fe	Ni	Al	Ti	Cd	Gd
$\beta_c (cm^{-1})$	1.00	1.61	0.093	0.25	30	545
$\mu (cm^{-1})$	0.12	0.25	0.008	0.20	2520	5×10^4

A1.3 Total Cross Section of Iron

The wavelength-dependent, unpolarized, neutron cross-section of iron has three components: coherent scattering (including magnetic scattering), incoherent scattering and absorption. The total cross-section was calculated and measured by Vinhas [1970]. It can be found that the principal contribution to the total cross-section of iron comes from absorption and coherent scattering as shown in figure A1.1.
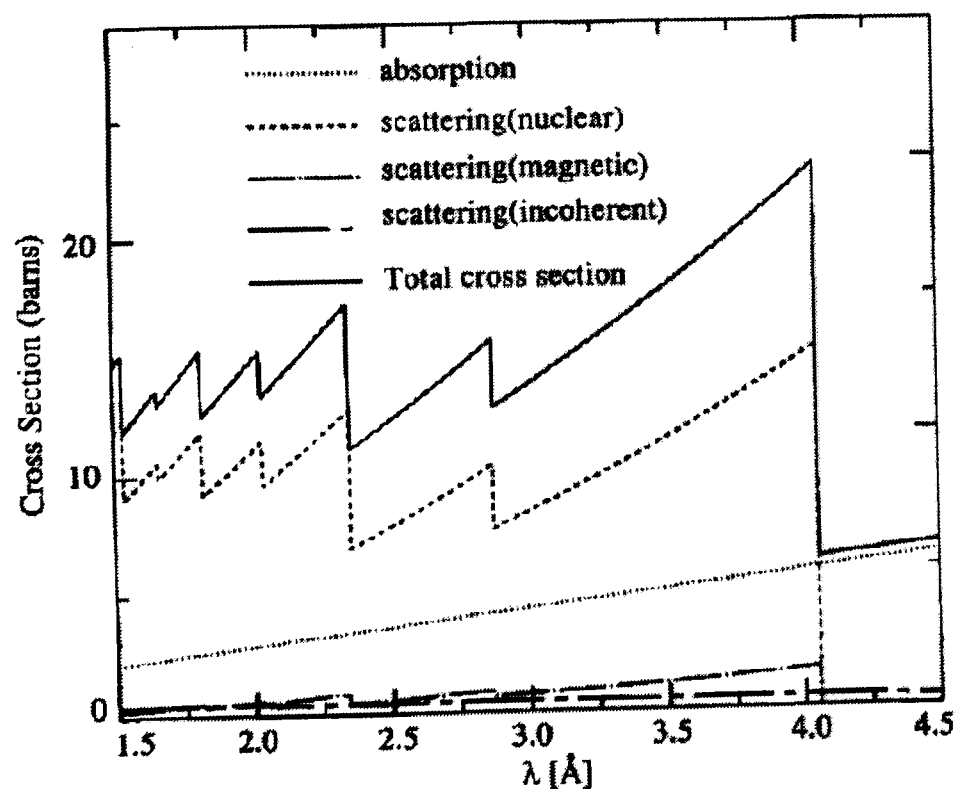
Figure A1.1 Total neutron scattering cross section of polycrystalline iron as a function of wavelength

122

APPENDIX 2: PROGRAMS FOR STRAIN MEASUREMENT AND DATA ANALYSIS ON ENGIN

A2.1 Typical Batch File in Strain Measurement

$ set noon

$ move x 10 mm

S   begin

S   change title """"Al plate"""""

S   waitfor 500 amps (or neutrons)

S   update

$ store

$ waitfor 1000 amps (or neutrons)

$ end

A2.2 Typical CCL File of Aluminium for Refinement on ENGIN

N

C   4.04955 4.04955 4.04955   90.000   90.000   90.000

S GRUP F M 3 M

A ATOM 0.0 0.0 0.0

F ATOM 1 1.0

I NCYC 5 MCOR 0 PRPR 2

L RTYP   1 10000.00 12000.00

L REFI 112

L WGHT 3

L SLIM 0.1 0.1 10

L THE2 90.0

L SCAL   0.01000

L BACK   2   0.01923   0.01707   -0.01993   -0.01949

    0.00728

L ZERO   1.3302

L PKCN   15.2640   0.0000

L PKFN TAUF   8.0000   0.0000   3.8314

L PKFN TAUS   8.0000   10.3430   2.8644

L PKFN SIGM   5.0000   0.0000   79.9020   0.0000

L PKFN GAMM   8.0000   0.0000   5.4196   0.0000

L PKFN SWCH   1.0000   3.5987   0.6221

L VARY ONLY ALL INTS ALL BACK ALL CELL SIGM 2 GAMM 2

    GAMM 1 ZERO 1 PKCN 2

APPENDIX 3: CALCULATION OF CENTROID POSITION

In this section the full calculation used for determination of centroid position are presented as outlined in Chapter 4, section three.

A3.1 Centroid Position for Vertical Scanning Geometry

In this case as shown in figure 4.1(a), the centroid position is simply the geometrical centre position in the gauge volume provided that the attenuation is ignored. However, if there is a strong attenuation effect, one has to use equation (4.14) to obtain the following equation:

$$2 \exp(-kr) - \exp(-kL) - 1 = 0 \qquad \text{(A3.1)}$$

then the centroid position in z-direction can be calculated. For example, the difference between geometry centre and the centroid is only 0.05 mm along z-direction, for iron with an attenuation coefficient, 0.112 mm^{-1}, if the gauge volume size is 2x2x2 mm^3.

However, if the spatial distribution of detected intensity is not a square pulse but a Gaussian-shape, for example, the focusing function of the collimator approximates as a Gaussian function, that is,

$$I(x,y,z) = \frac{I_0}{\sigma\sqrt{2\pi}} \exp\left[-\frac{z^2}{2\sigma^2}\right] \qquad \text{(A3.2)}$$

and the FWHM (full-width-at-half-maximum) defines the size of the gauge volume, then the spatial distribution of the detected intensity is

$$I(x,y,z) = \frac{2\sqrt{\ln 2}\,I_0}{c\sqrt{\pi}}\,\exp\left[-\frac{4\ln 2\,z^2}{c^2}\right] \tag{A3.3}$$

Comparison of the centroid position for Gaussian and square pulse of neutron intensity is shown in figure A3.1 by solving equation (4.14) using a partial integration method.
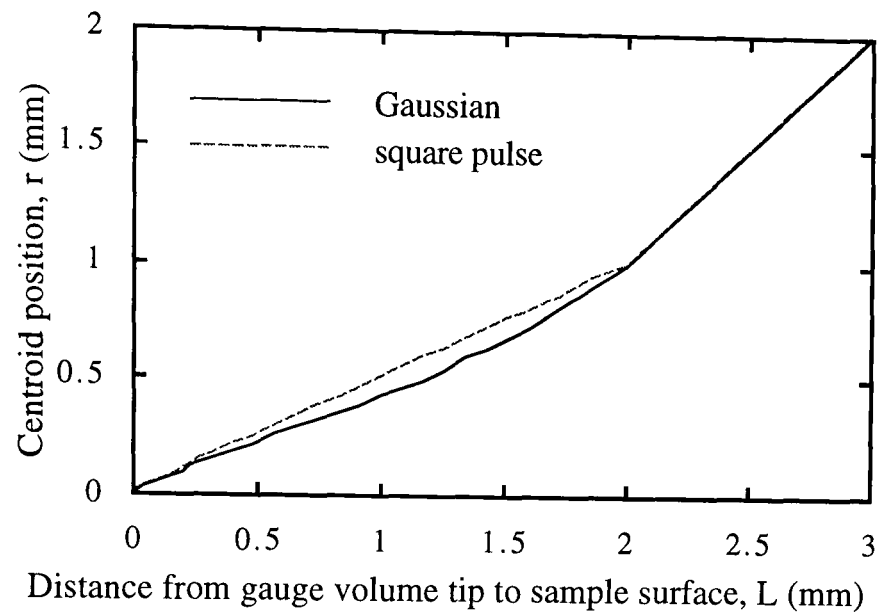
Figure A3.1 Comparison of the centroid position for a Gaussian and a square pulse function.

A3.2 Centroid Position for Horizontal Scanning Geometry

This case is plotted in figure 4.1(b). First considering the geometrical centroid position, e.g., without taking attenuation into account, the calculation has to be carried out in four different regions as the gauge volume enters the component :

a. when $0 < L \leq \dfrac{f}{\sqrt{2}}$, we have $\qquad r_I = \left(1 - \dfrac{1}{\sqrt{2}}\right)L$ $\qquad$ (A3.4)

b. when $\dfrac{f}{\sqrt{2}} \leq L \leq \dfrac{h}{\sqrt{2}}$, we have $\qquad r_{II} = \dfrac{2\sqrt{2}L^2 - 2fL - f^2 + \sqrt{2}f^2}{2(2\sqrt{2}L - f)}$ $\qquad$ (A3.5)

c. when $\dfrac{h}{\sqrt{2}} \leq L \leq \dfrac{f+h}{\sqrt{2}}$, we have

$$r_{III} = L - \frac{\dfrac{f^3 + \sqrt{2}f(h^2 - f^2)}{4} + \left(L - \dfrac{h}{\sqrt{2}}\right)\left(\dfrac{2f+h}{\sqrt{2}} - L\right)\left(\dfrac{f+h}{\sqrt{2}} - \sqrt{\left(\dfrac{f+h}{\sqrt{2}} - L\right)^2 - \dfrac{1}{2}\left(L - \dfrac{h}{\sqrt{2}}\right)\left(L - \dfrac{2f+h}{\sqrt{2}}\right)}\right)}{\left(\dfrac{2f+h}{\sqrt{2}} - L\right)\left(L - \dfrac{h}{\sqrt{2}}\right) + fh - \dfrac{f^2}{2}} \tag{A3.6}$$

126

d. when $L \geq \dfrac{f+h}{\sqrt{2}}$, we have $\qquad r_{VI} = L - \dfrac{f+h}{2\sqrt{2}}$ $\qquad$ (A3.7)

where r is the geometrical centroid position from sample surface; L, the distance between the top of gauge volume and sample surface; f, h, are the dimensions of the gauge volume.

If attenuation within the sample is taken into account, the case is more complicated and the calculation has to be performed in five different regions as following according to equation (4.14):

I. $0 < L \leq \dfrac{f}{\sqrt{2}}$,

$$\int_0^L (L-z)e^{-2\sqrt{2}kz}\,dz = 2\int_0^r (L-z)e^{-2\sqrt{2}kz}\,dz \qquad (A3.8)$$

II. $\dfrac{f}{\sqrt{2}} \leq L \leq 1.408$,

$$\int_0^L (L-z)e^{-2\sqrt{2}kz}\,dz = 2\int_{L-r}^L (L-z)e^{-2\sqrt{2}kz}\,dz \qquad (A3.9)$$

III. $1.408 \leq L \leq \dfrac{h}{\sqrt{2}}$,

$$2\int_0^r \sqrt{2}fe^{-2\sqrt{2}kz}\,dz = \int_0^{L-\frac{f}{\sqrt{2}}} \sqrt{2}fe^{-2\sqrt{2}kz}\,dz + \int_{L-\frac{f}{\sqrt{2}}}^L 2(L-z)e^{-2\sqrt{2}kz}\,dz \qquad (A3.10)$$

IV. $\dfrac{h}{\sqrt{2}} \leq L \leq \dfrac{f+h}{\sqrt{2}}$,

$$2\left\{ \int_0^{L-\frac{h}{\sqrt{2}}} 2\left[\frac{f+h}{\sqrt{2}} - (L-z)\right]e^{-2\sqrt{2}kz}\,dz + \int_{L-\frac{h}{\sqrt{2}}}^r \sqrt{2}fe^{-2\sqrt{2}kz}\,dz \right\}$$

$$= \int_{0}^{L-\frac{h}{\sqrt{2}}} 2\left[\frac{f+h}{\sqrt{2}} - (L-z)\right] e^{-2\sqrt{2}kz} \, dz + \int_{L-\frac{f}{\sqrt{2}}}^{L} 2(L-z) e^{-2\sqrt{2}kz} \, dz$$

$$+ \int_{L-\frac{h}{\sqrt{2}}}^{L-\frac{f}{\sqrt{2}}} \sqrt{2} f e^{-2\sqrt{2}kz} \, dz \qquad\qquad (A3.11)$$

where k is the attenuation coefficient of sample.

By solving equations (A3.8-A3.11), one can obtain the centroid position with attenuation effect as shown in figure 4.8. The attenuation effect causes a shift of the measured position 0.13 mm closer to surface in iron, which has an attenuation coefficient of 0.112 mm^{-1}. For aluminium, which possesses an attenuation coefficient of 0.0098 mm^{-1}, the effect will be less than 0.1 mm.

APPENDIX 4: SYSTEMATIC ERROR ANALYSIS ASSOCIATED WITH STRAIN MEASUREMENT

A4.1 Introduction

In any scientific experiment, the error associated with the measurement must be known if accurate interpretation of the results to be made. This is particularly true for engineering applications where it is of paramount importance that measurements are reproducible and comparable. Evaluation of errors is also of importance when automating measurements, as it enables errors to be calculated *a priori* by the operator.

This appendix will present an assessment of the systematic errors associated with residual strain measurement by neutron diffraction using ENGIN, a multi-detector instrument with radial collimators. Possible approaches to reduce the systematic error are discussed.

A4.2 Gauge Volume Average

The gauge volume used in neutron diffraction is defined by the incident beam size and the focusing function of the collimator as shown in figure A4.1. The variable dimensions of gauge volume are x and z for the current system. The dimension y is fixed in ENGIN by the focusing function of the collimator.

The lattice parameter obtained from any neutron diffraction measurement is an average of the lattice parameters of the subsets of crystals (grains) which satisfy Bragg's law within the gauge volume. As the size of the gauge volume increases, neutrons from different subsets of grains are detected and the measured lattice parameter is again a volume

average taken over all the grains in the particular subset within the gauge volume. This average can be expressed as [Noyan 1991]:
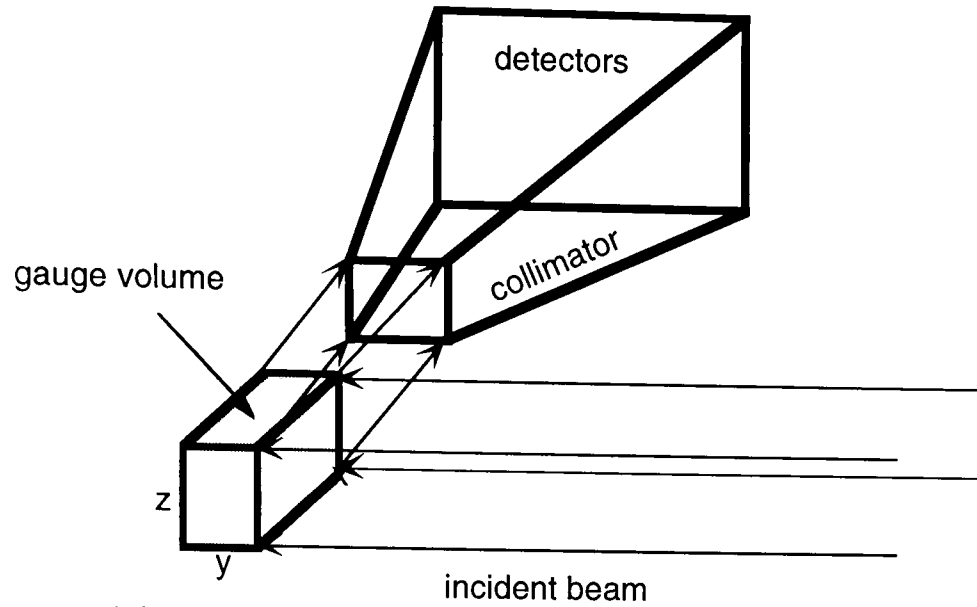
Figure A4.1 Definition of gauge volume size

$$\overline{\mathcal{E}} = \frac{\displaystyle\sum_{k=1}^{N_k} \frac{\displaystyle\int_{V_k} \mathcal{E}(x,y,z)f(z)dv}{\displaystyle\int_{V_k} f(z)dv}}{\displaystyle\sum_{k=1}^{N_k} V_k} \tag{A4.1}$$

where $\mathcal{E}(x,y,z)$ is the strain at the point (x,y,z) in the detected volume; V_k is the volume of these grains; $f(z)$ is a weight function relating the variation of diffracted intensity to depth(z); and N_k is the total number of grains satisfied Bragg equation (2.39) in the volume. Assuming that the diffraction is homogeneous without any variation of diffracted intensity with depth(z), then equation (A4.1) becomes

$$\overline{\mathcal{E}} = \frac{\displaystyle\int_v \mathcal{E}(x,y,z)dv}{V} \tag{A4.2}$$

where $\mathcal{E}(x,y,z)$ is a function of co-ordinate, x,y,z, and V is the gauge volume, whereas the "true" strain is defined by:

$$\mathcal{E}_t = \mathcal{E}(x_c, y_c, z_c) \tag{A4.3}$$

where x_c, y_c, z_c are the co-ordinates of the centroid of the gauge volume.

The effect of the gauge volume size on the different "true" type I strain spacial

distributions is discussed below. For simplification only the one-dimension case in

figure A4.2 is considered. For a linear strain distribution, it is:

$$\varepsilon = Ax \qquad\qquad (A4.4)$$

where A is a constant. In the region (x, x+c) (c is the gauge volume dimension), the

"true" strain is those at the geometry centre of the gauge volume:

$$\varepsilon_t = A\ (x+ c/2) \qquad\qquad (A4.5)$$

and the average strain with the gauge volume size, c, is

$$\bar{\varepsilon} = \frac{\int_{x}^{x+c} Axdx}{c} = A\ (x+ c/2) \qquad\qquad (A4.6)$$

Note that ε_t and $\bar{\varepsilon}$ have the same value. This means that gauge volume size has no effect

on the measurement of any linear spacial strain distribution.

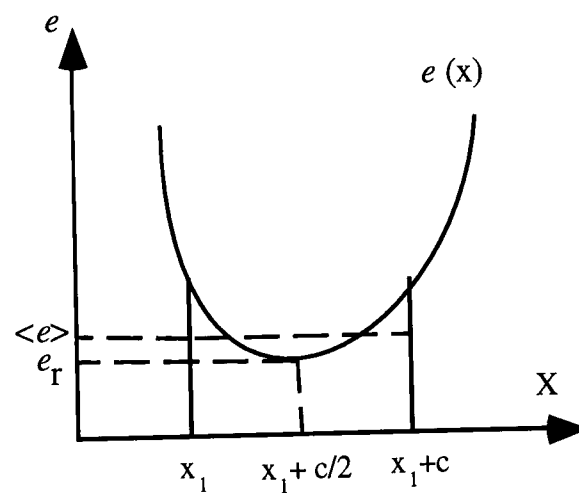Figure A4.2 Simplified case of strain spatial distribution.

However, if the spacial strain distribution is non-linear, and to a first approximation can

be taken to be quadratic, i.e.

$$\varepsilon = Ax^2 \qquad\qquad (A4.7)$$

where A is a constant, then the "true" strain at the point, c/2, is

$$\varepsilon_t = A\left(x+\frac{c}{2}\right)^2 = A\left(x^2+ xc + \frac{c^2}{4}\right) \qquad\qquad (A4.8)$$

131

where c is assumed to be the gauge volume dimension, whereas the strain measured with a gauge volume size, c, is described by

$$\bar{\varepsilon} = \frac{\int\limits_x^{x+c} Ax^2 dx}{c} = A\left(x^2 + xc + \frac{c^2}{3}\right) \qquad (A4.9)$$

so that

$$\bar{\varepsilon} - \varepsilon_t = \frac{Ac^2}{12} \qquad (A4.10)$$

showing that the strain measured with a gauge volume size, c, differs from the "true" strain by an amount of $Ac^2/12$.

Consider the strain possesses an exponential distribution thus:

$$\varepsilon(x) = \exp(Ax) \qquad (A4.11)$$

the strain difference between measured with the gauge volume of size, c, and the "true" value is

$$\bar{\varepsilon} - \varepsilon_t = \exp(Ax)\left(\exp\left(\frac{Ac}{2}\right) - A\exp(Ac) + \frac{1}{A}\right) \qquad (A4.12)$$

This value could be either positive or negative depending on the constant A.

In practice this means that the measured strain distribution from neutron diffraction is only likely to be markedly different from the real strain distribution in areas of highly changing strain gradients. Unfortunately it is not feasible to deconvolute the 'averaged' neutron strain measurements to the 'true' distribution, but it is possible to use neutron diffraction to validate other strain measurement techniques.

In summary, the "measured" strain spacial distribution which is the average over the gauge volume, is dependent on the "true" spacial distribution except where the "true" strain spacial distribution possesses a small strain gradient.

A4.3 Variation in Gauge Volume Size

An error could arise by gauge volume size variation, due to either an inhomogeneous spacial intensity distribution of the detected neutrons, or mis-alignment of the diffractometer. If the error occurs, it can be expressed as:

$$\Delta\varepsilon = -\frac{\Delta d}{d_0 + \Delta d}\,\varepsilon \tag{A4.13}$$

where $\Delta\varepsilon$ is the systematic error caused by the variation of gauge volume size; Δd, the error in lattice parameter; d_0, strain-free lattice parameter; and ε, measured strain. However, one can see from equation (A4.13) that the error is minor.

If one changes gauge volume size when measuring the strain-free sample, and makes d_0 either larger or smaller than its "true" value, one can see that it causes the strain spacial distribution $\varepsilon(x,y,z)$ to shift an amount derived from equation (2.44).

$$\Delta\varepsilon = \frac{d\,\Delta d}{d_0(d_0 + \Delta d)} \tag{A4.14}$$

where $\Delta\varepsilon$ is the strain variation caused by the lattice parameter shift or d-spacing shift of the strain-free sample, Δd. For example, if $\Delta d = 0.00027\text{Å}$ for iron, then $\Delta\varepsilon \approx 100\ \mu\varepsilon$.

A4.4 Diffraction Angle Average

The focus angles of the collimators on ENGIN are $22°$ in the vertical plane and $17°$ in the horizontal plane, as shown in figure A4.3. This means that every strain measurement is an average within the spatial angle. Generally, strain field in materials is triaxial, and can be described as an ellipsoid as follows [Barrett 1980]:

$$\left(\frac{x}{\varepsilon_1}\right)^2 + \left(\frac{y}{\varepsilon_2}\right)^2 + \left(\frac{z}{\varepsilon_3}\right)^2 = 1 \tag{A4.15}$$

where x, y, z, are co-ordinates along the principal axis, and $\varepsilon_1, \varepsilon_2, \varepsilon_3$ are the three principal strains.
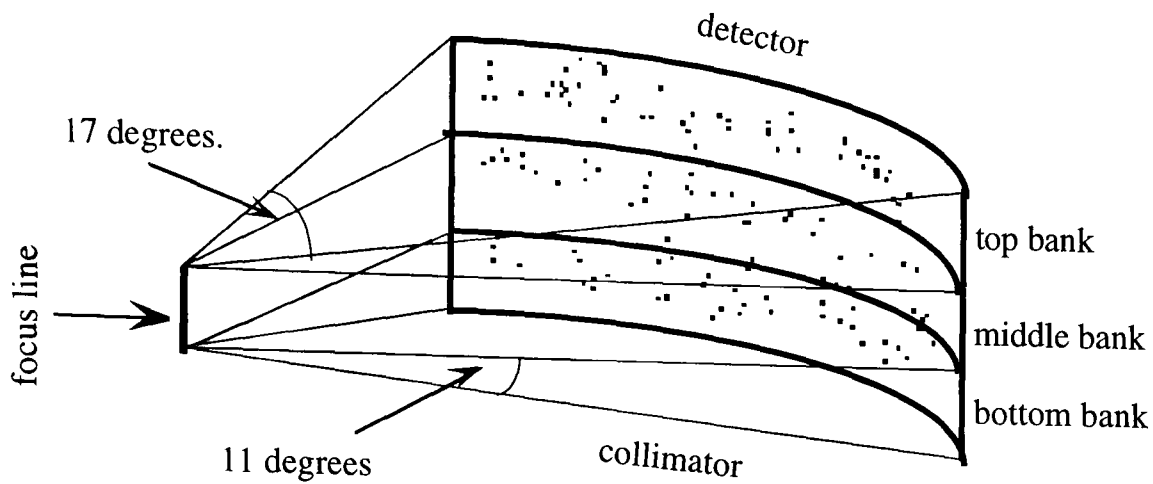
Figure A4.3 Focusing angle of the collimator

If one measures the principal strain ε_1, the angle average within the spatial angle of 17° degrees is

$$\bar{\varepsilon}_1 = 0.97\varepsilon_1 + 0.02(\varepsilon_2 + \varepsilon_3) \qquad (A4.16)$$

This means that the error from the collimator focus angle averaging over 17 degrees is principal-strain-dependent. One can obtain the true principal strains after measuring the three angle-averaging principal strains by solving equation (A4.16). For instance, if the real three principal strains are -5000 $\mu\varepsilon$, 1500 $\mu\varepsilon$ and 1500 $\mu\varepsilon$, respectively, then the measured three principal would be -4790 $\mu\varepsilon$, 1385 $\mu\varepsilon$ and 1385 $\mu\varepsilon$.

A4.5 Surface Pseudo-Strain Effect

A systematic error can occur where the gauge volume straddles the sample surface or an internal interface between two phases, or where the distribution of the phase being measured is not homogeneously distributed within the gauge volume. It happens in single detector systems [Bourke 1990] as well as in multi-detector systems with a collimator such as ENGIN at ISIS. The error results from the bias of the average diffraction length and volume for each individual detector [Harris 1995] as shown in figure A4.4. This causes a difference between the focusing routine for standard run (silicon powder or CeO_2) and the measurement run. Generally, differences of gauge volume size and shape, as well as the attenuation of materials between the standard and measured runs might affect the focusing routine. On ENGIN, the geometry is more

134

complicated since the radial collimator possesses 40 vanes and three banks of 45 detectors locate behind it [Wright 1994], which results in more difficultly quantitative modelling of the effect. However, the surface effect can be evaluated by either a set of experiments with powder specimen, or by a Monte Carlo simulation.
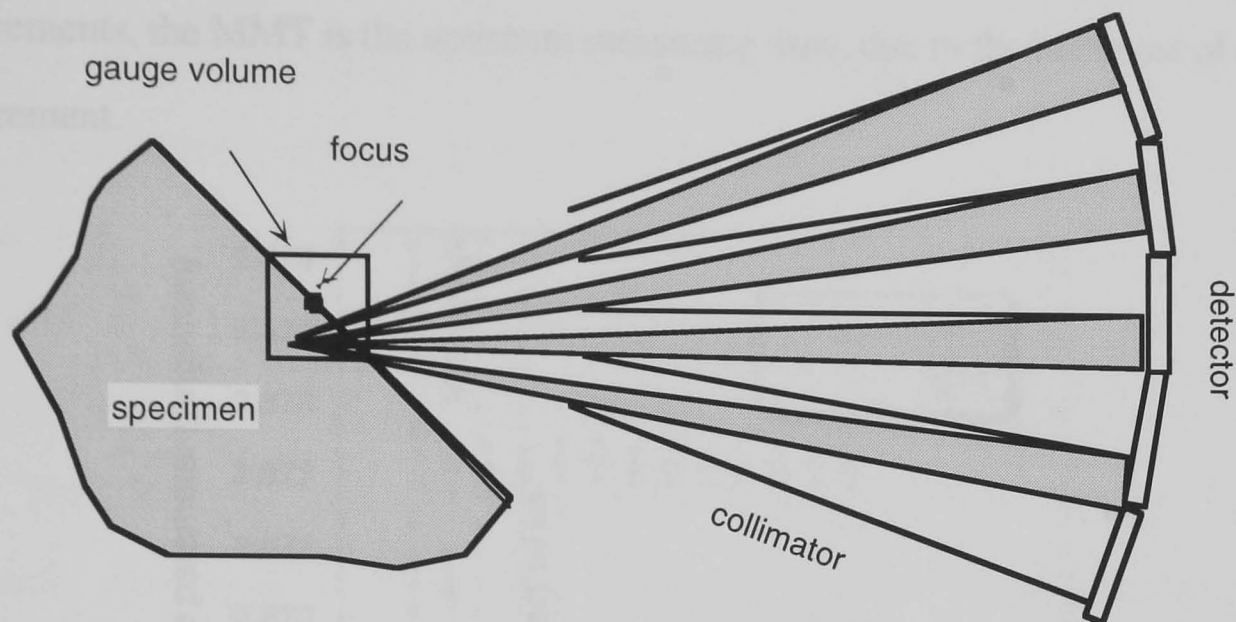

Fig. A4.4 Changes in average diffraction length and volume for individual detectors on ENGIN.

As discussed in chapter 4, two set-up geometries, for measuring the strain in the direction normal to the sample surface, and in the directions parallel to the sample surface, have been performed; and the results reveal that the former possesses 600 $\mu\epsilon$ systematic error, whereas the latter is about 50 $\mu\epsilon$. Obviously, the best geometry set-up to measure the near-surface strain is the latter one and correction is needed if measuring the near-surface strain in the direction normal to the sample surface. The correction can be made either by a Monte Carlo simulation, or by powder experiments, or by comparing the results from two geometrical set-ups for the same direction.

A4.6 Minimum Measurement Time (MMT)

As illustrated in figure A4.5, for any given material/geometry combination a minimum measurement time (or current) (MMT), may be defined after which further exposure produces little variation in measured lattice parameter. The MMT is controlled by properties of the data collection system (collimator and detector) and the diffraction beam

135

intensity. If the measurement time is less than MMT, the error could reach 500 με. It is interesting again to compare the two banks of detectors. As may be seen from figure A4.5, the detectors not only require different MMTs but also obtain different lattice parameters in the case that the two collimators may not be well aligned. For engineering measurements, the MMT is the optimum measuring time, due to the high cost of neutron measurement.
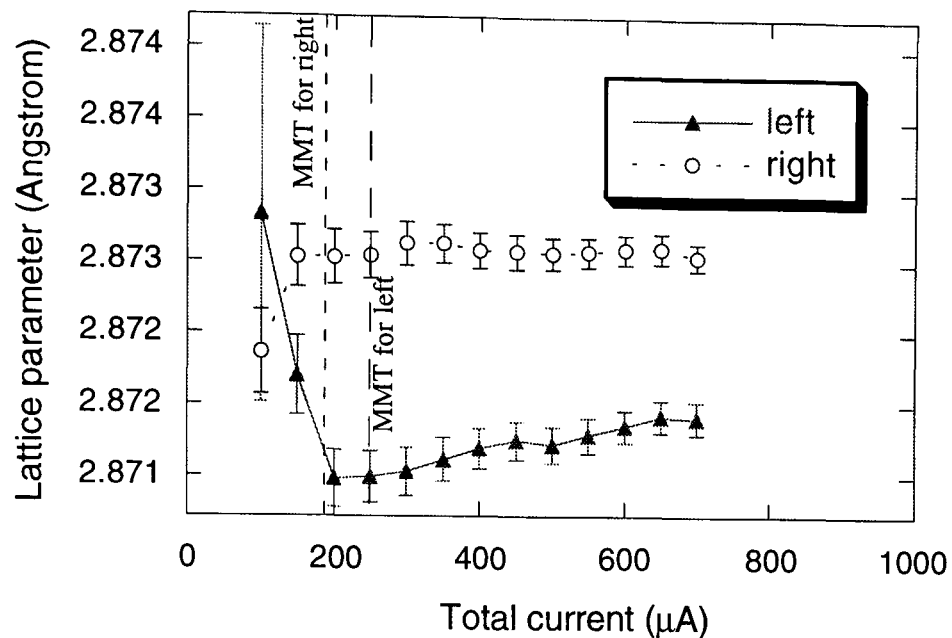
Figure A4.5 Variation of lattice parameter with measurement current for iron powder.

A4.7 Wavelength-dependent Attenuation

The effect of wavelength-dependent attenuation in materials on strain measurement might cause large systematic error if measurements are performed deep in materials and on a monochromatic diffractometer [Hsu 1995]. For the measurements in iron, the pseudo-strain could be 1000 με if the Bragg edge meets with the diffraction peak whereas it is negligible on an energy-dispersive diffractometer, like ENGIN at ISIS. The effect on shift of diffraction peaks arising from distortion of diffraction peak shape, which is much stronger in a monochromatic diffractometer than in an energy-dispersive diffractometer and dependence of crystalline structure and texture of materials measured, experimental geometry and instrumental configuration. Detailed theoretical analysis and experimental work can be found in chapter 8.

136

A4.8 Plastic Deformation and Anisotropy

Plastic deformation and strong anisotropy in materials might also cause error in strain measurement. The former can result in an increase in stiffness for some crystallographic reflections while some show a reduction. For example, plastic deformation is known to involve the rotation of grains and as such can affect the degree of anisotropy [Smith 1988]. During cyclic loading a large variation in modulus will obviously occur in material showing marked anisotropy. The PSECs (Plane Specific Elastic Constants) of planes (200) and (220) are affected by cyclic loading, leaving significant residual strains, while (311) remains almost unaffected in a nickel-base superalloy (Udimet 720) [Ezeilo 1992]. The shifts in individual reflections are therefore different both in sign and in magnitude. An extreme example is strain measurement in Incoloy-800 [Holden 1988, 1995], in which the strains derived from the (111) and (002) reflections had different signs.

It can be seen that calibration experiments are necessary to determine the most suitable reflections for strain/stress measurement, particularly for the monochromatic diffractometers, where only one reflection is used for determining the stress field in a material.

A4.9 Conclusions

A systematic error can arise: from the effect of gauge volume averaging and the focusing angle of the collimator; from the variation of gauge volume size and wavelength-dependent attenuation; when measuring the strain near a surface; from insufficient measurement time; or from plastic deformation and anisotropy of materials. The way to improve the accuracy is by taking proper geometry and by accurately determining the gauge volume position using sufficient measurement time, and using the most suitable refection. The effect of wavelength-dependent attenuation on the systematic error of strain measurement is found to be negligible in the energy-dispersive strain scanner with

a radial collimator and multi-detectors. To make reproducible strain measurements it is important to pertain experiments using near-identical conditions of gauge volume size and instrument geometry.

APPENDIX 5: STRAINS FROM PAWLEY REFINEMENT

A5.1 Pawley Refinement Procedure

The strains in this thesis are obtained using Pawley refinement, which is a development of the Rietveld refinement method. It allows pattern decomposition and refinement of unit cell parameters. The software used in this work is called CAILS (Cell And Integrated intensities Least Squares) and was written by Prof Bill David et al of ISIS [David 1988]. There are 24 principal variables in this programme as described in Appendix 2. In its usual mode of operation to refine the raw data, all the parameters in the ccl file are set to values obtained by a standard run using silicon or CeO_2 powder. The meaning for the parameters in the ccl file can be listed as following [David 1992]:

Parameter	Function of refinement
BACK	Background
INTS	Peak intensities
CELL	Lattice parameters
SIGM 2, GAMM 1	Isotropic widths of diffraction peaks
GAMM 2	Anisotropic widths of diffraction peaks
ZERO 1	Zero-point shift
PKCN 2	Anisotropic shift of diffraction peak position

Among all the parameters, only the lattice parameters are used in strain (LP Strain, see chapter 3) measurement calculation. The initial value for the lattice parameters are a "guessing" value. For example, for a measurement with run number of 6615 (aluminium), the inital value may be 4.05 Å and the refined value is 4.05073± 0.00030 Å.

As the detectors do not all lie at 90° to the beam but are spread over 17 degrees (chapter 3), spectra from individual detectors need to be shifted to allow the diffraction pattern in each detector to have the same time of flight. This is done by putting on a standard sample (silicon or CeO_2 powder) and adjusting the value of $l\sin\theta$ (where l is the distance from the detector to the sample, 2θ is the scattering angle) for each detector so that the lattice parameters obtained from every detector are equal to that of the standard sample. The values of $l\sin\theta$ are then used in a focusing programme which aims at aggregating all subsequent spectra from individual detectors into a single spectrum. The output from the focusing routine is a file with an extension name, HIS.

After obtaining the raw data and all the suitable parameters for the ccl file, the refinement procedure can be started. The initial input data are the place where the file is, file specification for instrument constants, run number, region of time-of-flight for refinement, refinement option, symmetry elements of crystal structure, lattice parameters and title for the refinement [Wright 1995]. The following is an example of refinement for aluminium (f.c.c.) powder. The input data are:

SCRATCH$DISK:[DQW01]

UTILITYN:SI_5623.IPARM

6615 1 2

3000 14000 1

F M 3 M

4.05

aluminium powder

The refinement procedure essentially involves: i>. putting all parameters to the initial values (see table A5.1); ii>. refining the parameters, BACK and INTS first, while fixing other parameters; iii>. refining BACK, INTS and CELL, fixing other parameters; and so on, until all parameters are refined. After the refinement is finished, one has to check if the refinement is properly completed by viewing the 'pictic' file [Wright 1995] as shown in A5.1 for aluminium powder. Then the lattice parameters and error can be found in a file with extension name, "OUT". The strain can be calculated using equation (2.44).
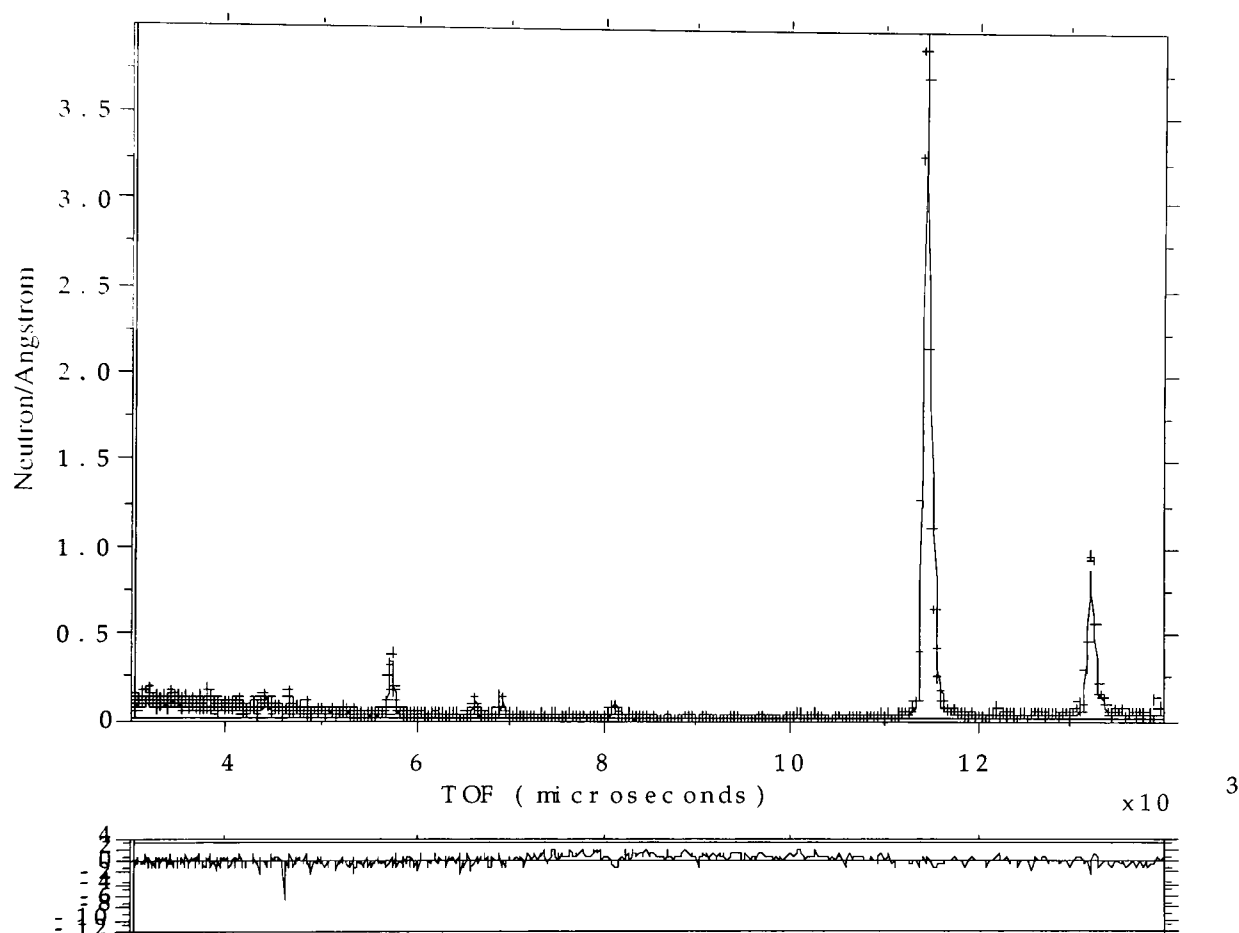

Figure A5.1 Assessing the refinement of the aluminium powder. There is a good fit between the model (line) and the experimental data (crosses). The lower box plots the diffrerence between the model and the data. The "fit" can be seen to be good.

A5.2 Typical Spectra Obtained on ENGIN

One advantage of a pulsed neutron spallation source is that the whole spectrum from the measurement can be seen [David 1988]. The typical spectra are given in figure A5.2-5.4.
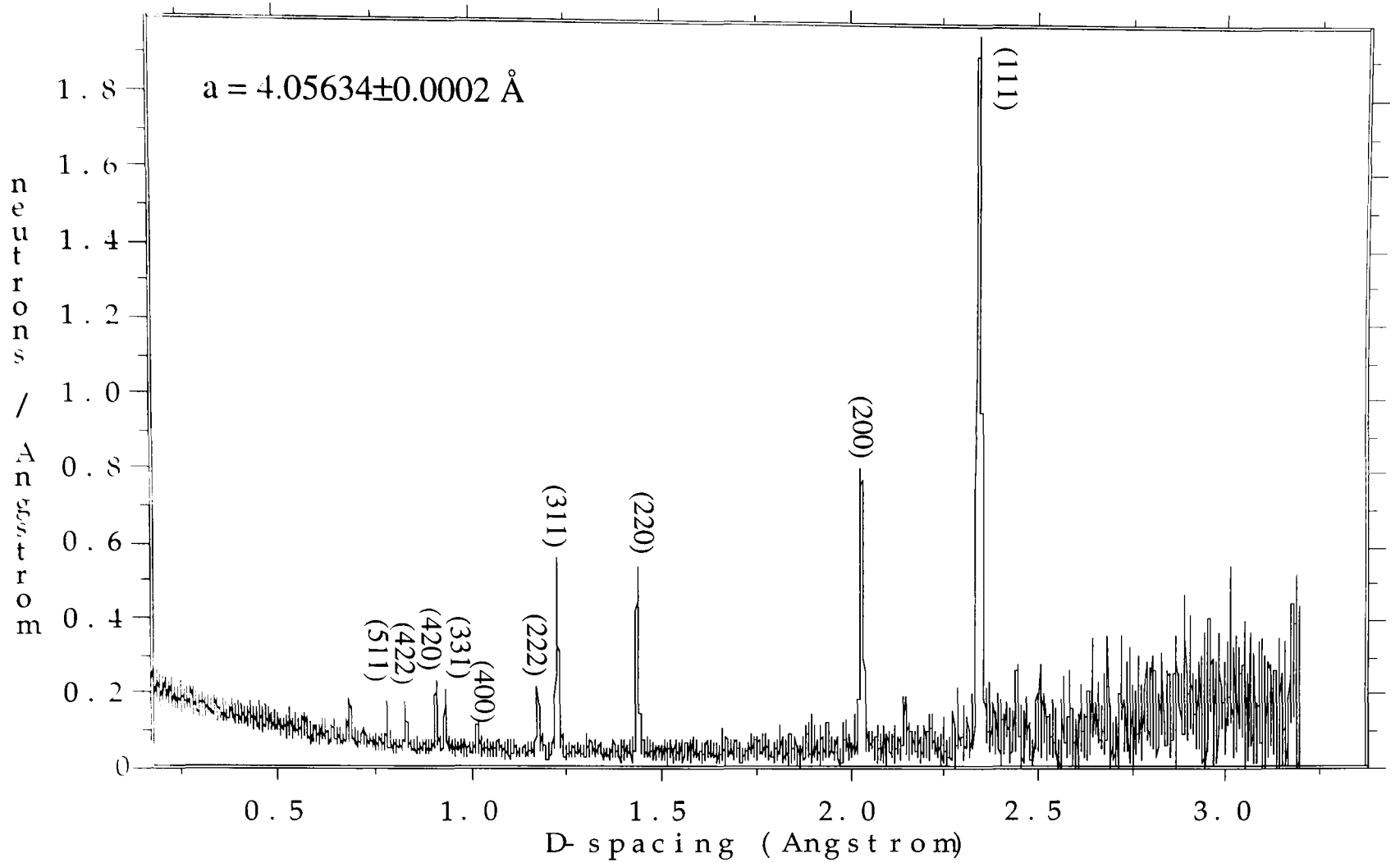
Figure A5.2 Diffraction spectrum of aluminium powder (f.c.c), 2x2x2 mm³

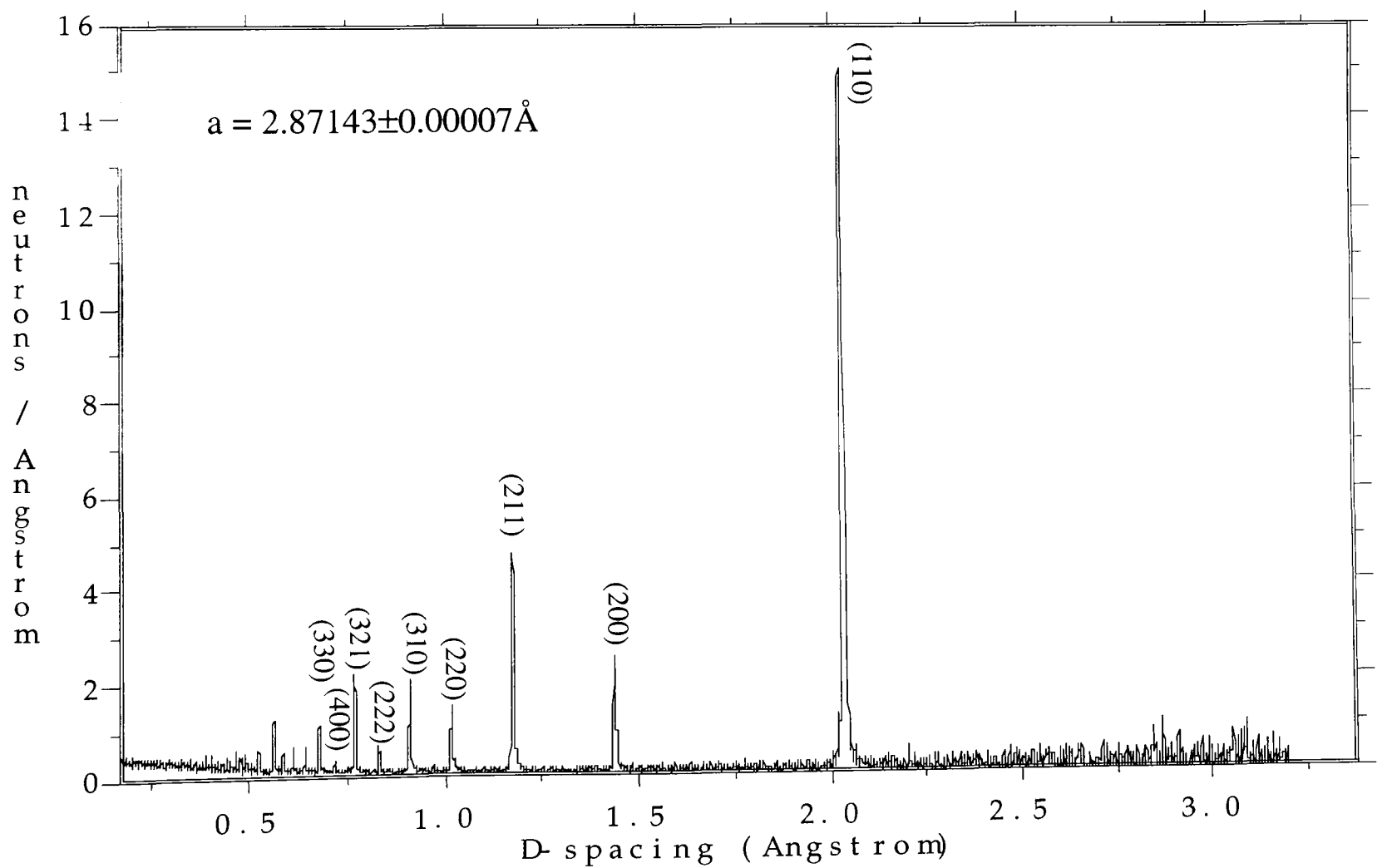Figure A5.3 Diffraction spectrum of iron powder (b.c.c), 2x2x2 mm³

It can be seen in figure A5.2 and A5.3 that the whole diffraction pattern of aluminium (f.c.c.) and iron (b.c.c.) are represented by eleven peaks and fourteen peaks, respectively.

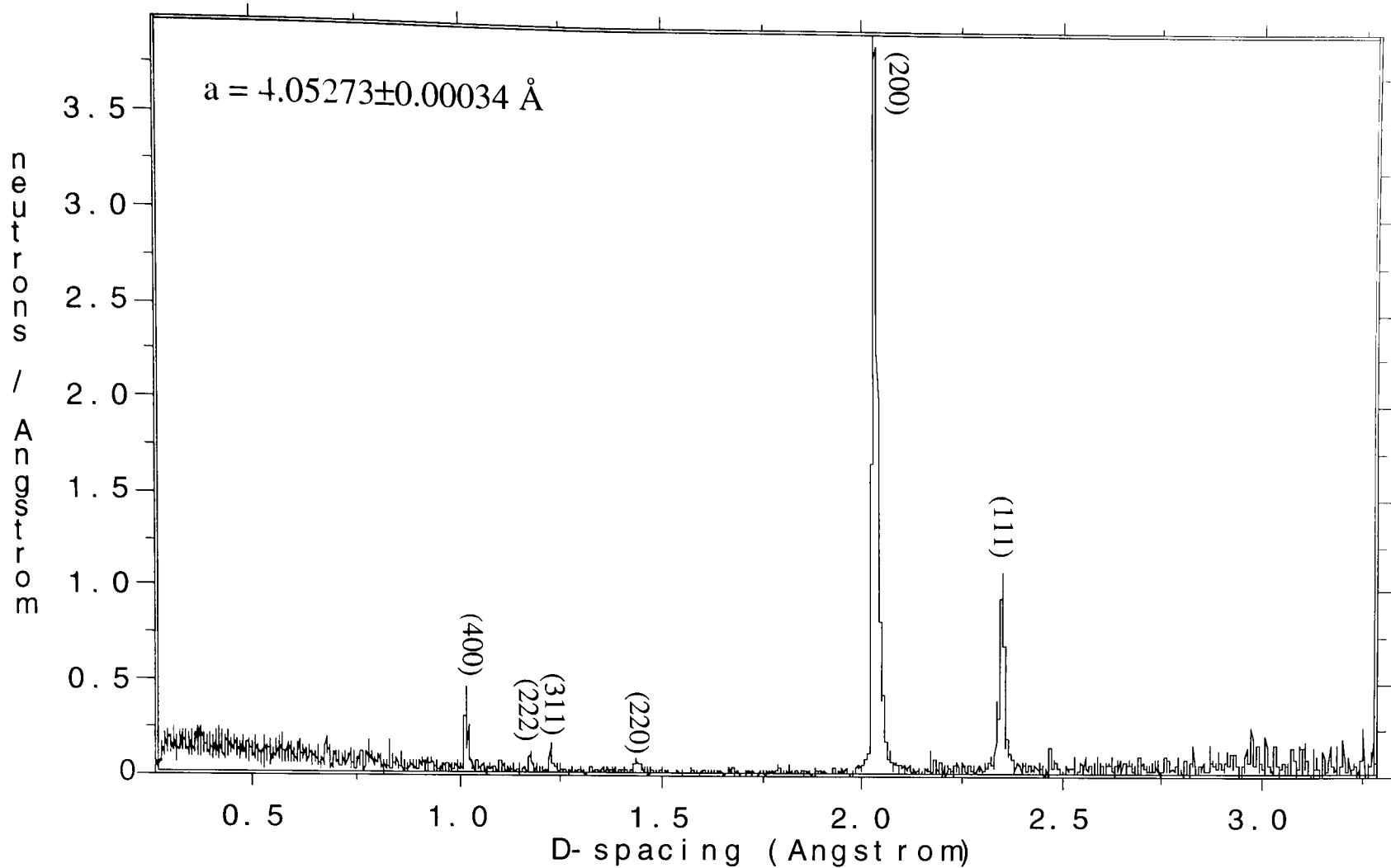Figure A5.4 Diffraction spectrum of the aluminium plate (f.c.c.), hoop direction, 2x2x2 mm^3.
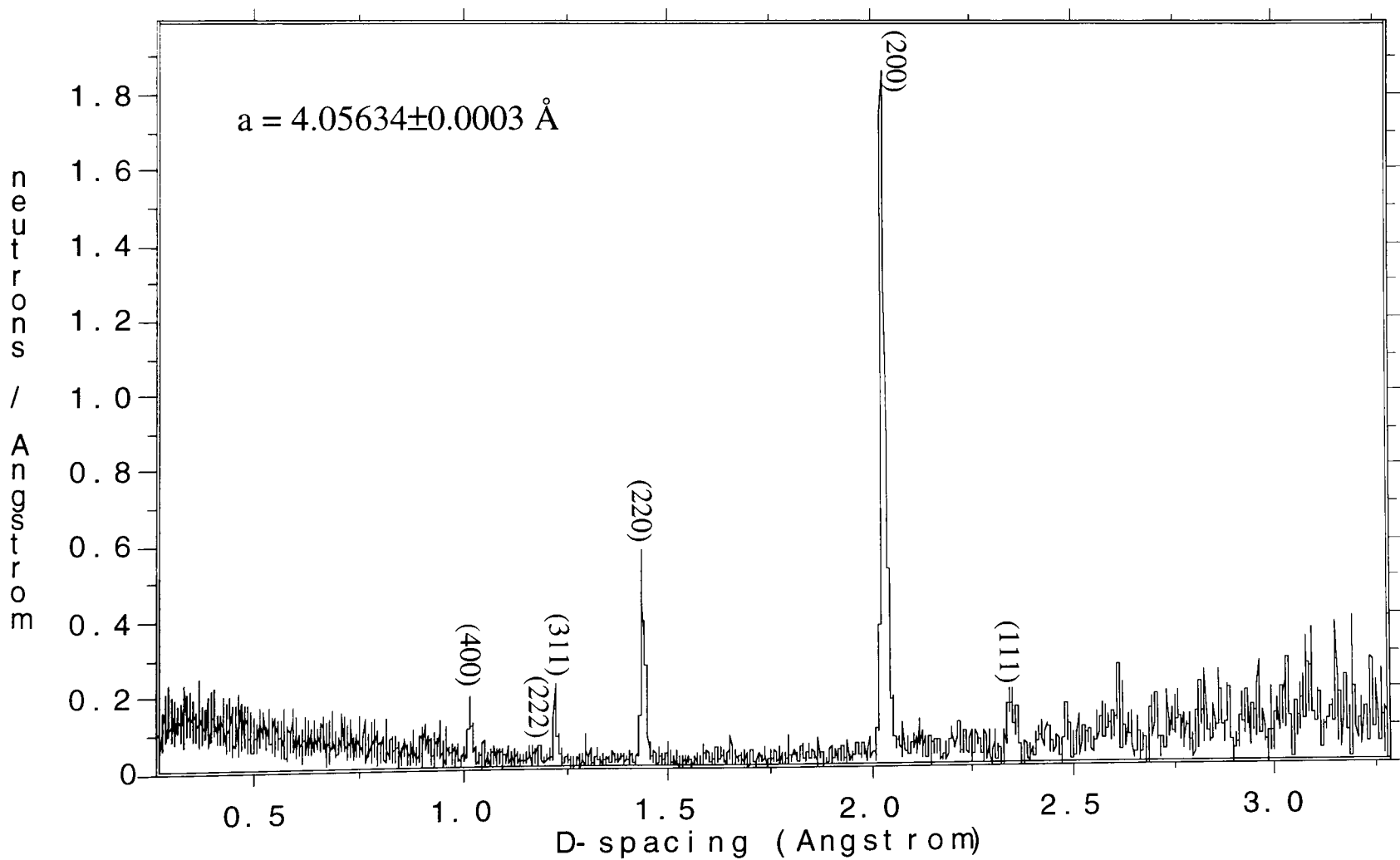
Figure A5.5 Diffraction spectrum of the aluminium plate, transverse direction, 2x2x2 mm^3.

Figure A5.4 and A5.5 shows the texture of aluminium plate containing the cold expanded hole as the relative peak intensities can be seen differ from that of aluminium powder.
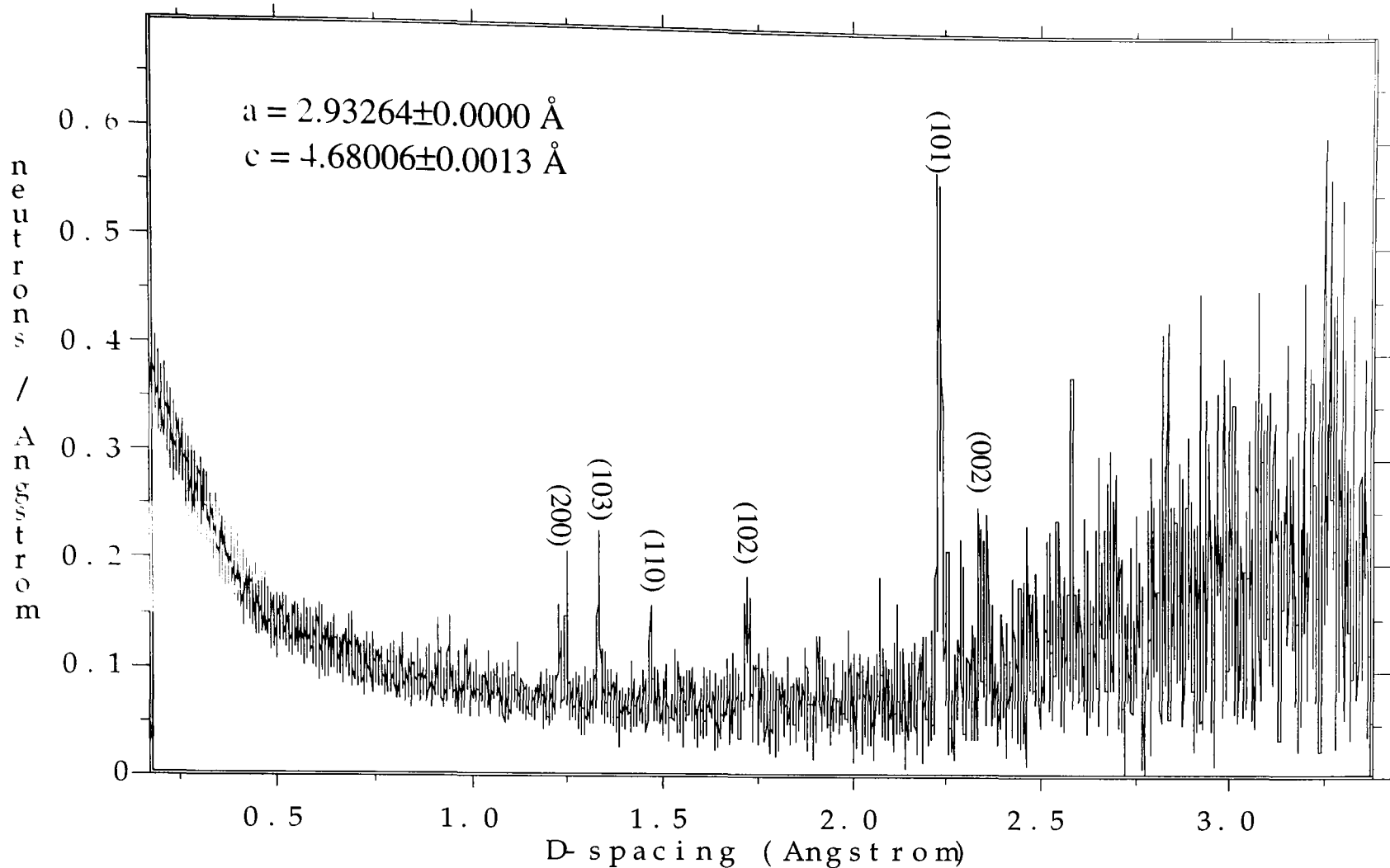
Figure A5.6 Diffraction spectrum of the shot-peened titanium (h.c.p) plate, 2x25x0.5 mm^3.

Figure A5.7 Diffraction spectrum of the austenitic steel ring (f.c.c.), 2x2x4 mm^3.

A large inelastic scattering coefficient of titanium causes a high background as shown in figure A5.6. The multi-scattering effect from iron in the beam also contributes a high background (see figure A5.7).

144

REFERENCES

Allen, A., Andreani C., Hutchings, M. T. and Windsor C. G. (1981), "Measurement Of Internal Stress Within Bulk Materials Using Neutron Diffraction." NDT International (October): 249-254.

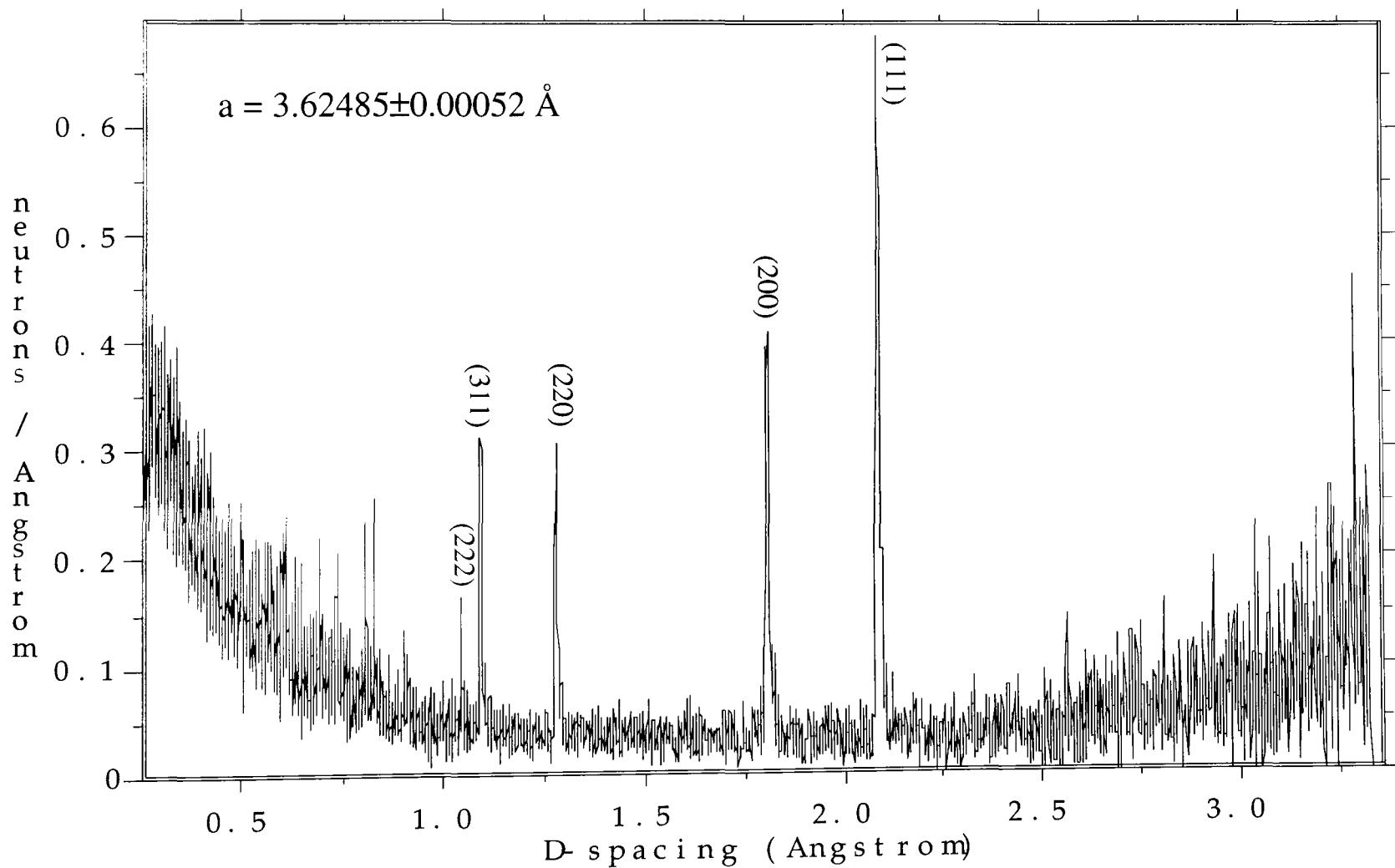Allen, A. J., Hutchings, M. T., Windsor, C. G. and Andreani, C. (1985), "Neutron Diffraction Methods for the Study of Residual Stress Fields." Adv. in Phys. 34: 445-473.

Allen, A. J., Hutchings, M. T., Krawitz, A. D. and Windsor, C. G. (1987), "Neutron Diffraction Measurement Of Internal Stress In Bulk Materials: Metal-Matrix Composites", Residual Stresses In Science And Technology, ed. E. Macherauch and V. Hauk, publ. DGM Informationsgesellschaft Verlag.

Almen, J. O., Black, P. H. (1963), Residual Stresses and Fatigue in Metals, publ. McGraw Hill Book Co. Inc.

Bacon, G. E. (1975), Neutron Diffraction, publ. Clarendon Press, Oxford.

Barrett, C., Massalski, T. B. (1980), Structure Of Metals - Crystallographic Methods, Principles And Data. Publ. Pergamon Press, Oxford.

Behnken, H., Hauk, V. (1991), "Berechnung und Ermittlung der rontgenographischen Spannungsfaktoren texturierter Werkstaoffe - Vergleich mit experimentellen Ergebnissen" Z. Metllkunde 82: 151-158.

Boland, B., Whapham, S. (1992), ISIS User Guide Experimental Facilities. SERC, UK

Bourke, M.A.M., Goldstone, J. A., Holden, T.M. (1991), "Residual Stress Measurement Using The Pulsed Neutron Source at LANSCE", Measurement Of Residual And Applied Stress Using Neutron Diffraction, Publ. Kluwer Academic Publishers, Oxford, UK, pp. 369-382

Bourke, M. A. M. (1990), "Residual Stress Measurement In Engineering Components By Neutron Diffraction", Ph.D thesis, Imperial College of Science, Technology & Medincine, London

Buras, B., Gerward, L. (1975), "Relations Between Integrated Intensities In Crystal Diffraction Methods For X-Rays And Neutrons", Acta Crystallogr A31: 372-374.

Carpenter, J. M., Yelon, W. B. (1986), "Neutron Sources", Methods Of Experimental Physics 23 (Part A): 99-197, ed. K.Skold and D. L. Price, Publ. Academic Press, Inc.

Champoux, R. L. (1986), "An Overview Of Cold Expansion Methods", Fatigue Prevention and Design, ed. J.T. Barnby, Chamelon Press, London, pp.35-45.

Cook, R. (1994), Stress Analysis Of A High Load Transfer Joint With Secondary Bending (Q-Joint). Defence Research Agency, DRA/SMC/TR942058

Cullity, B. D. (1977), "Some Problems In X-Ray Stress Measurements", Adv. in X-ray Anal. 60: 259-271.

Cullity, B. D. (1978), Elements of X-ray Diffraction, Publ. Addison-Wesley Publishing Co. Inc.

David, W. I. F., Akporiaye, D. E., Ibberson, R. M. and Wilson, C. C., The High Resolution Powder Diffractometer at ISIS-An Instroductory Users Guide, Rutherford Appleton Lab report, RAL-88-103

David, W. I. F., Johnson, M. W., Knowles, K. J., Moreton-Smith, C. M., Crosbie, G. D., Campbell, E. P., Graham, S.P., Lyall, J. S. (1986), Punch GENIE Manual Version 2.3. Neutron Division, Rutherford Appleton Lab.

David, W. I. F., Ibberson, R. M., Matthewman, J. C. (1992), Profile analysis of neutron powder diffraction data at ISIS. Rutherford Appleton Lab. RAL-92-032

Delsanto, P. P., Mignona, R. B., Clark, A. V., Mitrakovic, D., Moulder, J. C. (1986), "Acoustoelastic Determination of Residual Stresses", Residual Stresses, Germany, Garmisch-Partenkirchen.

Eshelby, J. D. (1957), "The Determination of the Elastic Field of an Ellipsoidal Inculsion, and Related Problem", Proc. of the Royal Society, 241A:376-396, London

Ezeilo. A. N. (1992), Residual stress determinations by neutron and X-ray diffraction methods. Ph.D. thesis, Department of Mechanical Engineering, Imperial college of Science, Technology and Medicine, London

Goldstone, J.A. (1994), "Calculation Of The Effect Of Thick Layers Of Material In The Beam", PREMIS Mid-term report (Brite EuRam program contract No. BRE2-CT92-0156), ISIS.

Harris, I. H. and Withers, P. J. (1995), "Residual strain measurement on ENGIN", PREMIS third-year report (Brite EuRam program contract No. BRE2-CT92-0156), ISIS.

Hauk, V.M., Oudelhoven, R., Vaessen, G.J.H. (1982), "The State Of Residual Stress In The Near Surface Region Of Homogeneous And Heterogeneous Materials After Grinding", Met. Trans. A. 13A: 1239-1244

Hauk, V., Troost, A., Ley, D. (1986), "Lattice Strain Measurements and Evaluation of Residual Stresses on Polymeric Materials", Proc. of Residual Stresses, Garmisch-Partenkirchen, Germany, Publ. DGM informationsgesellschaft

Holden, T. M., Holdt, R. A., Dolling, G., Powell, B. M., Winegar, J. E. (1988), "Charaterization Of Residual Stresses In Bent Incoloy-800 Tubing By Neutron Diffraction", Metall. Trans. 19A: 2207-2214.

Holden, T. M., Hosbons, R. R., MacEWen, S. R., Flower, E. C., Bourke, M. A., Goldstone, J. A. (1992), "Comparison Between Finite Element Calculation And Neutron Diffraction Measurement Of Residual Stress In A Diametrically Compressed Ring", Measurement of Residual and Applied Stress Using Neutron Diffraction, ed. M.T.Hutchings and A.D.Krawitz, Pulb. Kluwer Academic Publishers, pp.93-112

Holden, T. M., Root, J. H., Holt, R. A., Hayashi, M. (1995), "Neutron-Diffraction Measurement Of Stress", Physica B $\underline{214}$: 793-796.

Hutchings, M. T., Hipplsey, C, Rainey, V. (1990), "Neutron Diffraction Measurement Of The Stress Field During Fatigue Cycling Of A Cracked Test Specimen", Mat. Res. Soc. Symp. $\underline{166}$: 318-321

Hiismaki. P., Trunov, V. A., Anston, O., Kudryashov, V.A., Kukkonen, H., Poyry, H.. Shebetov, A. F., Tiita, A., Ulyanov, V.A. (1985), "Experience Of The Fourier Time-Of-Flight (Tof) Neutron Techniques For High-Resolution Neutron Diffractometry", Neutron Scattering In The Nineties, Publ. IAEA,Vienna.

Herzer, R. (1990), AUSTRA-An Instrument for the Automated Evaluation of Stress States Using Ultrasonic Techniques. Experimental Mechanics, $\underline{3}$:1150-1158

Hill, R. (1952), Proc. Phy. Soc., $\underline{A65}$: 349-354

Hughes, D. J. (1953), Pile Neutron Research, Publ. Addison-wesley Publishing Company, Inc.

Hutchings, M. T. (1991), "Neutron Diffraction Measurement Of Residual Stress Field: Overview And Points For Discussion", Measurement Of Residual And Applied Stress Using Neutron Diffraction, ed. M.T.Hutchings and A.D.Krawitz, Publ. Kluwer Academic Publishers, Oxford, pp. 3-18.

Hsu, T. C., Marsiglio, F., Root, J. H., Holden, T. M. (1995), "Effect Of Multiple Scattering And Wavelength-Dependent Attenuation On Strain Measurements By Neutron Scattering", J. Neutron Research, $\underline{3}$: 27-39.

Ikeda, S., Carpenter, J. M. (1985), "Wide-Energy-Range, High-Resolution Measurements of Neutron Pulse Shapes of Polyethylene Moderators", Nuclear Instruments & Methods In Physics Research Section A-Accelerator Spectrumeter Detectors And Associated Equipment, 239: 536-544.

Johnson, R.G., Bowman, C. D. (1981), "High-Resolution Powder Diffraction By White Source Transmission Measurements", Neutron Scattering 1981, ed. J.Faber, AIP conf. proc. no 89: 53-55

Krawitz, A. D. and Winholtz, R. A. (1994), "Use Of Position-Dependent Stress-Free Standards For Diffraction Stress Measurements", Materials Science and Engineering A185: 123-130.

Krawitz, A. D., Brune, J. E., Schmank, M. J. (1981), "Residual Stress And Stress Relaxation", Proc. of 28th Sagamore Army Materials Research Conference, pp. 139-156

Krawitz, A. D. (1991), "Stress Measurements in Composites Using Neutron Diffraction. in Measurement of Residual and Applied Stress Using Neutron Diffraction", ed. M.T.Hutchings and A.D.Krawitz, Publ. Kluwer Academic Publishers,Oxford, pp. 405-420

Kroner, E. (1958), "Berechnug der Elastischen Konstant des Vielkristalls aus den Konstant des Einkristalls." Z. Physik 151: 504.

Kupperman, D. S. (1994), "Neutron-Diffraction Determination Of Residual Stresses In Advanced Composites", Annu. Rev. Mater. Sci. 24: 265-291.

Lorentzen, T., Brand, P. C. (1991), "Summary Of The Panel Discussion Of Instrumentation At Steady State Sources", Measurement of Residual and Applied Stress Using Neutron Diffraction, ed. M.T.Hutchings and A.D.Krawitz, Publ. Kluwer Academic Publishers, Oxford, pp. 355-359

Mann, J. Y., Jost, G. S. (1983), "Stress Fields Associated With Fitted And Cold Expanded Holes", Metal Forum 6: 43-53.

Macherauch, E. (1986), "Origin, Measurement And Evaluation Of Residual Stresses. Residual Stresses", Proc. of Residual Stresses, ed. E.Macherauch and V.Hauk, Publ. DGM informationsgesellschaft, Germany, pp. 3-10

Meggers, K., Priesmeyer, H. G., Trela, W.J., Bowman, C.D., Dahms, M. (1994), "Real Time Neutron Transmission Investigation Of The Austenite-Bainite Transformation In Grey Iron", NIM B, Beam Interactions With Materials & Atoms, B88: 423-429.

Noyan, I. C., Cohen, J. B. (1987), Residual Stress, Measurement by Diffraction and Interpretation. Springer-Verlag.

Niku-Lari, A., Lu, J., Flavenot, J. F. (1985), "Measurement of Residual Stress Distribution by the Incremental Hole-Drilling Method", J. Mechanical Working Technology, 2: 2-9

Neerfeld, H. (1942), Mitt. K.W.I. Eisen. Dusseldorf, 24: 61-70.

Noyan, I. C. (1985), "Determination Of The Unstressed Lattice Parameter "AO" For (Triaxial) Residual Stress Determination By X-Rays", Adv. X-ray Anal, 28: 281-288.

Naik, R. A., Crews, J. H. (1991), AIAA Jounal, 29: 89-95.

Noyan, I. C. (1991), "The Theory Of Stress/Strain Analysis With Diffraction, In Measurement Of Residual And Applied Stress Using Neutron Diffraction", ed. M.T.Hutchings and A.D.Krawitz, Publ. Kluwer Academic Publishers, Oxford, pp. 51-66.

Ozdemir, A. T. (1993), Residual Stresses And Fatigue Performances At Cold Expanded Fastener Holes, Ph.D. thesis, Materials Discipline, The Open University

Ozelton, M. W., Coyle, T. G. (1986), "Fatigue Life Improvement By Cold Working Fastener Holes In 7050 Aluminium", Fatigue In Mechanically Fastened Composite And Metallic Joints, ed. J. M. Potter, ASTM STP, 927: 53-71.

Pintschovius, L., Jung, V., Maucherauch, L., Schefer, R., Vohringer, O. (1981), 28th Sagamore Army Materials Research Conference: 467-482

Priesmeyer, H. G., Schroder, J. (1990), "Residual Stress Analysis By Neutron Time-Of-Flight At A Reactor Source", Materials Research Society Symp., 166: 299-304.

Priesmeyer, H.G.(1988), "Neutron Strain Radiography", Proc. of Second International Conference on Residual Stresses, Publ. Elsevier, pp. 197-202

Procter, E., Beaney, E. (1987), "The Trepan or Ring Core Method, Centre Hole Method, Sachs Method, Blind Hole Methods, Deep Hole Technique." Advances in Surface Treatments, 4: 165-198.

Pell, R. A., Beaver, P. W., Mann, J. Y., Sparrow, J. G. (1989), "Fatigue Of Thicksection Cold-Expanded Holes With And Without Cracks", Fat. Fract. Eng. Mat. & Struct., 12: 553-567.

Prummer, R., Pfeiffer, W., Reisacher, E. (1988), "X-ray Elastic Constants and Residual Surface Stress State in Glass Ceramic", Proc. of Residual Stresses, Garmisch-Partenkirchen, Germany, Publ. DGM informationsgesellschaft

Reuss, A. and Angew, Z.(1929), "Berechnung der fliessgrenze von misch kristallen auf grund der plastizitatsbedingung fur einkristalle", Math. Mech., 9: 49-58

Ruppersberg, H., Detemple, I. (1993), "Evaluation Of The Stress Field In A Ground Steel Plate From Energy-Dispersive X-Ray Diffraction Experiments", Matls. Sci. Eng., A161: 41-44.

Ruud, C. O. (1982), "A Review of Selected Non-destructive Methods of Residual Stress Measurement", NDT Int. (July): 249-254.

Sawyer, J. W., Rothgeb, T. M. (1994), "An Instrumented Fastener For Sheer Force Measurements In Joints", Experimental Mechanics, 34: 16-22.

Smith, D. J., Leggatt, R. H., Webster, G. A., MacGillivray, H. J., Webster, P. J., Mills, P. J. (1988), "Neutron-Diffraction Measurements Of Residual-Stress And Plastic-Deformation In An Aluminum-Alloy Weld", J. Strain Analysis, 23: 201-211

Sachs, V. G. (1927), "Der Nachweis innerer Spannungen in Stangen and Rohren", Zeit fur Metallkunde, 19: 352-362.

Schajer, G. S. (1988), "Measurement of Non-Uniform Residual Stresses Using the Hole Drilling Method Part I - Stress Calculation Procedures", J. Eng.Materials and Technology 110: 338-343.

Schmank, M. J., Krawitz, A. D. (1981), "Measurement Of A Stress Gradient Through The Bulk Of An Aluminuim Alloy Using Neutrons", Metallurgical Transactions A, 13A: 1069-1076.

Schwarmann, L. (1982), "On Improving Fatigue Performance Of A Double Shear Lap Joint", International Journal of Fatigue, 2: 105-111.

Stacey, A. (1985), Prediction of Fatigue Crack Growth in Thick Walled Tubing, Ph.D thesis, Imperial College of Science, Technology & Medincine, London.

Tan, P. W., Bigelow, C. A., O'Donoghue, P. E., Atluri, S. T. (1993), ICAF'93 2: 1191-1251, ed. A.F.Blom, publ. EMAS.

Taylor, A. D. (1984), SNS Moderator Performance Preditions. Rutherford Appleton Laboratory, RAL-84-120

Thompson, R. B. (1994), "An Overview of Ultrasonic Measurement Techniques", Proc. of the Fourth International Conference on Residual Stresses, ed. M.R.James, publ. Society for Experimental Mechanics, Inc., pp. 97-111

Toraya, H. (1993), "Position-Constrained And Unconstrained Powder-Pattern-Decomposition Methods", The Rietveld Method, ed. R. A. Young, Publ. Oxford Science Publications, pp. 254-275.

Theiner, W. A., Brinksmeier, E., Stucker, E., Nowack, H. (1986), "Stress Measurements on Components with Nondestructive Ferromagnetic Methods", Proc. of Residual Stresses, Garmisch-Partenkirchen, Germany, pp. 167-174

Vinhas, A. L. (1970), "Estudo da interação de nêutrons lentos com o ferro policristalina", Ph.D thesis. Universidade Estadual de Compinas, Brazil.

Voigt, W. (1928), "Lehrbuch der Kristallphysik", Leipzig: Teubner : 962.

Webster, P. J., Low, K. S., Mills, G., Webster, G. A. (1990), "Neutron Measurement Of Residual Stresses In A Used Railway Rail", Mat. Res. Soc. Symp. Proc., 166: 311-316

Webster, P. J. (1992), "The Neutron Strain Scanner: Measurement In Weld", Mechanical Effects Of Welding, Publ. Springer, Berlin, pp. 143-150.

Windsor, C. G., Izuyama, T. (1991), "The Effects Of Cyrstalline Anisotropy On The Elastic Response Of Materials", Measurement Of Residual And Applied Stress Using Neutron Diffraction, ed. M.T.Hutchings and A.D.Krawitz, Publ. Kluwer Academic Publishers, Oxford, UK, pp. 147-158

Windsor, C. G. (1981), Pulsed Neutron Scattering, Publ. Taylor & Francis Ltd., London.

Winholtz, R. A., Krawitz, A. D. (1995), "The Relaxation Of Residual Stresses With Postweld Heat Treatment In A High-Performance Weld Measured With Neutron Diffraction", Metallurgical And Materials Transactions 26A: 1287-1295.

Wright, J. S., Johnson, M. W. (1994), Development of the ENGIN instrument. RAL Mid-term Report, (Brite/EuRam II Project no. 5129, Contract BRE2-CT92-0156), ISIS.

Wright, J. S. (1995), The ENGIN Mini-manual, RAL Report, RAL-95-017

Young, R. A., Ed. (1993), The Rietveld Method. IUCr Monographs on Crystallography. Oxford University Press.